A FINITE ELEMENT APPROACH FOR THE IMPLEMENTATION OF MAGNETOSTRICTIVE MATERIAL TERFENOL-D IN AUTOMOTIVE CNG FUEL INJECTION ACTUATION

by

H. A. CHOWDHURY
B. Sc. Engg. (ME), MASME, MSAE

A thesis submitted for the degree of
Master of Engineering

School of Mechanical and Manufacturing Engineering
Faculty of Engineering and Computing
Dublin City University

July 2008

Supervisor
DR. ABDUL GHANI OLABI

M.Eng 2008

Declaration

I hereby certify that this material, which I now submit for assessment on the programme of study leading to the award of Master of Engineering is entirely my own work, that I have exercised reasonable care to ensure that the work is original, and does not to the best of my knowledge breach any law of copyright, and has not been taken from the work of others save and to the extent that such work has been cited and acknowledged within the text of my work.

……………………………………….…

H. A. CHOWDHURY

Student ID Number: 54179416

Date: July 2008

Dedications

TO MY BELOVED

MAA

(HOSNE ARA BEGUM)

&

BABA

(NURUL AMIN CHOWDHURY)

Acknowledgments

First and foremost, I offer my sincerest gratitude to my supervisor, Dr. Abdul Ghani Olabi, who has supported me throughout my research with his patience and diligence. I would like to express my appreciation towards him for providing me with the unique opportunity to work with this interesting research topic, for his assistance and his expert guidance throughout the research. I would also like to thank Prof. Saleem Hashmi, for his tremendously erudite and inspiring conversations from time to time. Furthermore, I could not help myself from expressing my earnest admiration towards their remarkable support during my physical disability which was once hampering my research enormously. Therefore, at this point of acknowledgement, when I look back at those exasperating moments, I could feel nothing but respectful and thankful towards them.

I would like to thank my friend and colleague Dr. Saiful Amri Mazlan for his implausible support regarding exchanging ideas and arguments at my workplace, which facilitated in acquiring diverse knowledge in the field of smart materials. I would also like to thank Nasser Ekreem and Andrew Clarke for their suggestions, resources and encouragement.

In my daily work, I have been truly blessed with a friendly and cheerful group of fellow colleagues. Consequently, I would like to thank Dr. Ezzeddin Hassan, Hussam Achour and Dr. Mohammed Dabnoon.

The School of Mechanical and Manufacturing Engineering has provided the multiple software support that I have needed to perform and complete my research.

Finally, I would like to thank all my family members for their unconditional love and support throughout my studies.

Abstract

Magnetostriction is the deformation that spontaneously occurs in ferromagnetic materials when an external magnetic field is applied. In applications broadly defined for actuation, magnetostrictive material *Terfenol-D* possesses intrinsic rapid response times while providing small and accurate displacements and high-energy efficiency, which are some of the essential parameters required for fast control of fuel injector valves for decreased engine emissions and lower fuel consumption compared with the traditional solenoid fuel injection system.

A prototype CNG fuel injector assembly was designed, which primarily included magnetostrictive material Terfenol-D as the actuator material, *1020 Steel* having soft magnetic properties as the injector housing material, *AWG* copper wire as the coil material and *316 Stainless Steel* having non-magnetic properties as the plunger material. A 2D cross-sectional geometry including the injector housing, coil, Terfenol-D shaft, and plunger, was modeled in both *Finite Element Method Magnetics (FEMM)* and *ANSYS* for 2D axisymmetric magnetic simulation. The magnetic simulations were performed in order to determine the coil-circuit parameters and the magnetic field strength to achieve the required magnetostrictive strain, and consequently, the injector needle lift. The FEMM magnetic simulations were carried out with four different types of AWG coil wires and four different injector coil thicknesses in order to evaluate the relationship between the different coil types and thicknesses against the achieved strain or injector lift. Eventually, the optimized parameter obtained from FEMM results analysis was verified against ANSYS electromagnetic simulation.

Subsequently, a three dimensional replica of the CNG flow conduit was modelled in *GAMBIT* with the resultant injector lift. The meshed conduit was then simulated in *FLUENT* using the *3D time independent segregated solver* with *standard k-ε*, *realizable k-ε* and *RSM* turbulent models to predict the mass flow rate of CNG to be injected. Eventually, the simulated flow rates were verified against mathematically derived static flow rate required for a standard automotive fuel injector considering standard horsepower, BSFC and injector duty cycle.

Table of Contents

Declaration ……………………..……..………..……………………………. ii

Dedications ……..…………………………………………………………... iii

Acknowledgements …………………………...………………………….. iv

Abstract ……………………..………………………………………………. v

List of Tables ………………...…………….…………………………….. xi

List of Figures ……………………………………………………………. xii

CHAPTER ONE : INTRODUCTION

1.1 Introduction 1

1.2 Motivation and purpose of study 2

1.3 Outline of thesis 3

CHAPTER TWO : LITERATURE REVIEW OF CNG FUEL INJECTION ENVIRONMENTS

2.1 Introduction 5

2.2 Compressed natural gas 6

2.3 Dedicated natural gas engines (mono-fuel) 7

  2.3.1 Direct injection 7

    2.3.1.1 *Direct injection strategies* 7

    2.3.1.2 *Timings of fuel injection and ignition* 10

    2.3.1.3 *Fuel injector* 10

    2.3.1.4 *Injector driver* 11

    2.3.1.5 *Nozzles* 11

  2.3.2 Stratified charge combustion 12

2.4 Compressed natural gas in diesel environment 13

  2.4.1 Pilot ignited high pressure direct injection of natural gas 13

    2.4.1.1 *Diesel pilot injection strategy* 13

2.4.2 Direct injection with hot surface ignition 14
2.4.2.1 *Hot surface ignition strategy*.. 14
2.4.3 Dual-fuel diesel engine with induced natural gas 16
2.4.3.1 *Dual-fuel diesel engine with induced NG strategy* 16
2.4.4 Natural gas combustion assisted with gas-oil in a diesel engine 18
2.5 Compressed natural gas in gasoline environment.. 18
2.5.1 CNG as an alternative fuel for a retrofitted gasoline vehicle..................... 18
2.5.2 Natural gas direct injection in spark ignited Otto cycle engine 19
2.6 Compressed natural gas and hydrogen... 20
2.6.1 Hydrogen assisted jet ignition (HAJI).. 20
2.6.1.1 *HAJI strategy* 21
2.7 Summary of chapter two 22

CHAPTER THREE : LITERATURE REVIEW OF SMART MATERIALS

3.1 Introduction... 24
3.2 Actuator Materials.. 24
3.3 Mechanism of Magnetostriction 26
3.4 Fuel Injection 30
3.4.1 Prospect for smart materials 30
3.4.2 Comparative discussion between conventional solenoid injection and injection actuated by smart materials.. 31
3.5 Magnetostrictive Material Terfenol-D 34
3.5.1 Terfenol-D properties.. 34
3.5.2 Young’s modulus of Terfenol-D 36
3.5.3 The magnetomechanical coupling factor and the magnetostrictive coefficient... 37
3.5.4 Quality factor.. 39
3.5.5 Permeability of Terfenol-D 39
3.5.6 Hysteresis loop of Terfenol-D.. 41
3.5.7 Blocked force of Terfenol-D 43
3.6 Measurements of magnetostriction 44
3.7 Production of smart materials 44

3.8 Piezoelectric non-linearity 45
3.9 Real-time control of magnetostrictive actuators 46
3.10 Recent developments 47
3.11 Summary of chapter three 49

CHAPTER FOUR : FUEL INJECTOR DESIGN CONCEPT AND ACTUATING PARAMETER DETERMINATION

4.1 Introduction 51
4.2 Prototype CNG fuel injector 51
  4.2.1 Mechanism of the fuel injector 52
4.3 Fuel injector component material properties 54
  4.3.1 1020 Steel 54
  4.3.2 Grade 316 Stainless Steel 55
4.4 Actuating parameter determination 56
4.5 Summary of chapter four 59

CHAPTER FIVE : FEMM MAGNETIC FIELD SIMULATION

5.1 Introduction 61
5.2 Relevant Partial Differential Equations 61
  5.2.1 Magnetostatic problems 61
  5.2.2 Time-harmonic magnetics problem 62
5.3 Model Construction and Analysis 63
  5.3.1 Problem definition and creating model geometry 65
  5.3.2 Boundary conditions 67
  5.3.3 Material and circuit properties 69
  5.3.4 Meshed geometry 71
5.4 FEMM analysis results 72
  5.4.1 Magnetostatic series circuitry 72
  5.4.2 Magnetostatic parallel circuitry 77
  5.4.3 Time-harmonic series circuitry 81
5.5 Summary of chapter five 84

CHAPTER SIX : ANSYS ELECTROMAGNETIC VERIFICATION

6.1 Introduction 86
6.2 Low-frequency electromagnetic analysis 86
  6.2.1 Element type used in 2-D static magnetic analysis 87
  6.2.2 Magnetic formulation 88
6.3 ANSYS Electromagnetic nodal analysis preprocessor 89
  6.3.1 Geometry modeling 89
  6.3.2 Defining element type and material properties 90
  6.3.3 Meshed geometry 92
  6.3.4 Applying magnetic excitation and boundary condition 93
6.4 ANSYS Electromagnetic results 94
6.5 ANSYS and FEMM results verification 97
6.6 Summary of chapter six 99

CHAPTER SEVEN : CNG FUEL INJECTOR MASS FLOW RATE PREDICTION BY FLUENT

7.1 Introduction 101
7.2 Turbulence models 102
  7.2.1 The Standard $k-\varepsilon$ model 102
  7.2.2 The Realizable $k-\varepsilon$ model 103
  7.2.3 The Reynolds Stress Model (RSM) 104
7.3 Modeling of the CNG conduit 104
  7.3.1 Geometry creation 104
  7.3.2 Specifying zone types 107
  7.3.3 Meshing 107
    7.3.3.1 Mesh checking 109
  7.3.4 FLUENT solver 110
7.4 FLUENT simulation results 111
  7.4.1 Sample calculation of injector flow rate 113
7.5 Summary of chapter seven 115

CHAPTER EIGHT : CONCLUSIONS & RECOMMENDATIONS

8.1 Conclusions 117
8.2 Contributions of the thesis 119
8.3 Recommendations for future work 119
8.4 Summary of chapter eight 120

REFERENCES..………………………………………………………....... 121

APPENDICES

Appendix A : Publications…..……………………………………… I
Appendix B : CAD drawings…………………………………….. II
Appendix C : FEMM magnetostatic simulation results…………….. IV

List of Tables

Table 2.1 : Properties of some conventional fuels and CNG………………… 6

Table 3.1 : Terfenol-D properties…………………………………………….. 35
Table 3.2 : Relative permeability of different ferromagnetic materials……… 40

Table 4.1 : Typical material properties of 1020 Steel………………………... 54
Table 4.2 : Typical material properties of 316 Stainless Steel……………….. 56
Table 4.3 : Required parameters to achieve in simulation……………………. 58

Table 5.1 : Table of AWGs…………………………………………………… 64
Table 5.2 : Coil number of turns in layers……………………………………. 65
Table 5.3 : Comparison between data analysis and FEMM result for 22 AWG with 5 mm coil thickness………………………………….. 75
Table 5.4 : Summary of the results between series and parallel circuit properties………………………………………………………… 81

Table 6.1 : Assigned material model number in ANSYS…………………….. 92
Table 6.2 : Percentage error calculation for FEMM and ANSYS flux density output………………………………………………………….... 98

Table 7.1 : Zone type specifications………………………………………….. 107
Table 7.2 : GAMBIT mesh investigation…………………………………….. 109
Table 7.3 : Assumptions for CFD analysis…………………………………… 111
Table 7.4 : Results of mass flow rates at the pressure outlet of the injector for P_{inlet}: 85 psig, P_{outlet}: 0 psig……………………………………….. 113
Table 7.5 : Assumptions for sample fuel flow calculation…………………… 114
Table 7.6 : Percentage difference between simulated and numerically derived mass flow rate…………………………………………………….. 115

List of Figures

FIGURE OF CHAPTER ONE

Figure 1.1 : Summary of the research process in chapter one………………… 4

FIGURES OF CHAPTER TWO

Figure 2.1 : Arrangements of the fuel injectors and the spark gap; (a) opposed and single injection, spark gap at centre and halfway between centre and wall, and (b) parallel injection with spark gap at centre……………………………………………………………... 8

Figure 2.2 : Schematic of diesel pilot ignition with natural gas DI…………… 14

Figure 2.3 : Glow plug ignition……………………………………………….. 15

Figure 2.4 : Concept of biform mixture formation in different piston cavity space in a dual-fuel engine; (a) Diesel fuel injection at 60° CA BTDC, and (b) Biform mixture formation at end of compression…………………………………………………… 17

Figure 2.5 : Schematic of hydrogen assisted jet ignition……………………… 21

Figure 2.6 : Summary of the research process in chapter two………………… 23

FIGURES OF CHAPTER THREE

Figure 3.1 : Joule magnetostriction. (a) The changes in shape in response to the magnetic field H. H is proportional to the current that passes through the solenoid. (b) The relationship between ΔL/L and H…………………………………………………………….. 27

Figure 3.2 : Graphical representation of strain vs. magnetic field (idealized behaviour)………………………………………………………… 28

Figure 3.3 : Schematic of strain vs. magnetic field…………………………... 28

Figure 3.4 : Application of compressive load to magnetostrictive materials….. 29

Figure 3.5 : Traditional fuel injector; (a) solenoid off, valve closed position; (b) solenoid on, plunger movement and valve open position…….. 32

Figure 3.6 Cross section of a prototypical Terfenol-D magnetostrictive transducer…………………………………………………………… 34

Figure 3.7 : Length change versus Terfenol-D rod with strain as parameter….. 36

Figure 3.8 : Young's modulus versus magnetic field………………………….. 36

Figure 3.9 : Strain versus magnetic field……………………………………… 38

Figure 3.10 : k_{33} and d_{33} versus applied stress…………………………………….. 38
Figure 3.11 : Hysteretic magnetization curve for ferromagnetic material……… 41
Figure 3.12 : General B-H curve of Terfenol-D………………………………... 42
Figure 3.13 : Full loop of magnetization………………………………………... 42
Figure 3.14 : Summary of the research process in chapter three……………….. 50

FIGURES OF CHAPTER FOUR

Figure 4.1 : Prototype CNG fuel injector assembly…………………………… 52
Figure 4.2 : CNG inlet-outlet port and needle valve…………………………... 53
Figure 4.3 : Non-linear B-H data of 1020 Steel from FEMM materials Library……………………………………………………… 55
Figure 4.4 : Terfenol-D strain vs. applied field at various preloads, data from ETREMA PRODUCTS INC……………………………….. 57
Figure 4.5 : Hysteretic magnetization curve for a ferromagnetic material and relevant points: B_R, remnance; (H_S, B_S), saturation; and H_C, coercitive field strength…………………………………………... 57
Figure 4.6 : B-H data of Terfenol-D, data from ETREMA PRODUCTS INC... 58
Figure 4.7 : Summary of the research process in chapter four………………... 60

FIGURES OF CHAPTER FIVE

Figure 5.1 : Injector components for FEMM simulation……………………… 64
Figure 5.2 : Problem definition in FEMM…………………………………….. 66
Figure 5.3 : Injector geometry in FEMM with four coil thicknesses………….. 67
Figure 5.4 : Applying boundary conditions in FEMM………………………... 69
Figure 5.5 : Adding material properties to the model………………………… 70
Figure 5.6 : Constructing Terfenol-D material model in FEMM……………... 70
Figure 5.7 : Meshed geometry in FEMM……………………………………... 71
Figure 5.8 : Power vs. current for coil thickness; (a) t = 2mm; (b) t = 3mm; (c) t = 4mm and (d) t = 5mm…………………………………... 72
Figure 5.9 : Average flux density vs. current for coil thickness; (a) t = 2mm; (b) t = 3mm; (c) t = 4mm and (d) t = 5mm……………………….. 73

Figure 5.10 : Current, power and voltage variation at flux density, B = 0.55 Tesla for coil thickness; (a) t = 2mm; (b) t = 3mm; (c) t = 4mm and (d) t = 5mm……………………………………………….. 74

Figure 5.11 : Flux density plot for 22 AWG with 672 turns in 8 layers; coil thickness, t = 5 mm……………………………………….. 76

Figure 5.12 : Change of flux density at different sections along the 15 mm half-section of the Terfenol-D shaft for 22 AWG with 672 turns in 8 layers…………………………………………………… 76

Figure 5.13 : Parallel circuit………………………………………………….. 77

Figure 5.14 : Parallel coil circuitry in FEMM……………………………….. 78

Figure 5.15 : Flux density variation for parallel and series coil circuitry………. 79

Figure 5.16 : Change of flux density at different sections along the 15 mm half-section of the Terfenol-D shaft for 22 AWG with 672 turns in 8 layers (t = 5 mm)………………………………………….. 80

Figure 5.17 : The parallel circuit properties for 22 AWG with 672 turns in 8 layers (t = 5 mm)………………………………………………… 80

Figure 5.18 : Variation of flux density for 22 AWG with 672 turns in 8 layers with 4.07 amps input current; (a) flux density vs. distance at different frequencies; (b) zoom in view of flux density vs. distance showing for 100 Hz and 250 Hz; (c) zoom in view of flux density vs. distance showing for 10 Hz, 20 Hz, 50 Hz and 100 Hz; (d) Flux density vs. frequency at the points (0,0), (5,0) and (10,0)…………………………………………………… 82

Figure 5.19 : FEMM time-harmonic series circuitry results output……………. 83

Figure 5.20 : Summary of the research process in chapter five………………… 85

FIGURES OF CHAPTER SIX

Figure 6.1 : Current density………………………………………………… 87

Figure 6.2 : PLANE13 element type geometry with nodes I, J, K and L…….... 88

Figure 6.3 : 2-D cross-sectional geometry in ANSYS showing line and area plot………………………………………………………….... 90

Figure 6.4 : Defining PLANE13 element type……………………………... 91

Figure 6.5 : (a) Defining material model behavior, (b) Terfenol-D B-H data input…………………………………………………………. 91

Figure 6.6 : Defining mesh attributes by area………………………………. 92

Figure 6.7 : Meshed geometry in ANSYS………………………………….. 93

Figure 6.8 : Applying current density and boundary condition………………. 94

Figure 6.9 : Magnetostatic options and solutions…………………………... 94
Figure 6.10 : (a) 2D flux lines; (b) Flux density vector sum nodal solution……. 95
Figure 6.11 : Flux density vector sum vector plot for 2D ½ expansion………… 96
Figure 6.12 : Electromagnetic force calculation, (a) Nodal solution, and (b) Vector plot…………………………………………………... 96
Figure 6.13 : Flux density vector sum vector plot; (a) FEMM output, and (b) ANSYS output……………………………………………... 97
Figure 6.14 : Flux density distribution along the indicated contour lines………. 98
Figure 6.15 : Summary of the research process in chapter six…………………. 100

FIGURES OF CHAPTER SEVEN

Figure 7.1 : Pro-Engineer model of the CNG flow conduit…………………… 105
Figure 7.2 : Importing Pro-E model as IGES in GAMBIT……………………. 106
Figure 7.3 : Imported CNG flow conduit model in GAMBIT………………… 106
Figure 7.4 : Meshed geometry in GAMBIT…………………………………... 108
Figure 7.5 : Equi-angle skewness quality……………………………………... 109
Figure 7.6 : Overview of the segregated solution method…………………….. 110
Figure 7.7 : Velocity vector colored by static pressure (Pa)…………………... 112
Figure 7.8 : Summary of the research process in chapter seven………………. 116

FIGURES OF CHAPTER EIGHT

Figure 8.1 : Summary of the research process in chapter eight……………….. 120

FIGURES OF APPENDIX B

Figure B1 : Injector housing…………………………………………………... II
Figure B2 : Needle valve……………………………………………………… II
Figure B3 : Plunger……………………………………………………………. III
Figure B4 : Closing spring…………………………………………………….. III

FIGURES OF APPENDIX C

Figure C1 : Variation of power and average flux density with current at coil thickness, t = 2 mm for; (a) 22 AWG, (b) 24 AWG, (c) 28 AWG and (d) 30 AWG…………………………………………………….. IV

Figure C2 : Variation of power and average flux density with current at coil thickness, t = 3 mm for; (a) 22 AWG, (b) 24 AWG, (c) 28 AWG and (d) 30 AWG…………………………………………………….. V

Figure C3 : Variation of power and average flux density with current at coil thickness, t = 4 mm for; (a) 22 AWG, (b) 24 AWG, (c) 28 AWG and (d) 30 AWG…………………………………………………….. VI

Figure C4 : Variation of power and average flux density with current at coil thickness, t = 5 mm for; (a) 22 AWG, (b) 24 AWG, (c) 28 AWG and (d) 30 AWG…………………………………………………….. VII

CHAPTER ONE

INTRODUCTION

1.1 Introduction

In many of the emerging engine technologies, it is becoming evident that the integration and adoption of multi-functional smart materials are essential alternatives for the development of fuel injection applications at a time when the necessity of emission reduction is of enormous significance. The integration of actuating capability at the micron scale affords the realization of extremely controlled and effective fuel injector actuator systems that would be able to respond to an environmental stimulus such as change in magnetic field. *Magnetostriction* (MS) is such a phenomenon in which the shape of certain type of materials changes under the influence of an external magnetic field. This change in shape is the result of the rotation of small magnetic domains which causes internal strains in the material structure. The magnetostrictive effect was first described in the 19th century (1842) by an English physicist James Joule.

In this context, numerous studies have shown that varying the rate and the shape of fuel injection cycles and using multiple injections per cycle can significantly increase the fuel efficiency of internal combustion engines and lower their NOx and particulate emissions. The need for multiple injection capability during power combustion cycles has inspired research into the development of high-speed, low-cost magnetostrictive and piezoelectric actuators. These actuators can potentially act twice as fast as solenoid actuators. This intrinsic rapid response time enables the engine designer to match the fuel system and engine after-treatment requirements for optimal performance. Furthermore, as the transportation sector account for the majority of man-made global pollution and as almost all the traditional vehicles belonging to this sector use petroleum based fuels, the necessity exists for the innovation and implementation of advanced alternative fuel systems for automotive application. In this context, *compressed natural gas (CNG)* possesses tremendous potential due to its ability towards reduced CO_2, CO, particulate matter (PM) and NOx emission without compromising the engine power output through innovative and enhanced fuel injection techniques. Therefore, the integration of magnetostrictive actuators with CNG fuel injection system offer tremendous prospects for both emission reduction and fuel injection system optimization.

1.2 Motivation and purpose of study

Magnetostrictive (MS) materials possess exceptional characteristics in terms of rapid, reliable and reversible strain with high force generating capabilities in the presence of a magnetic field. On the other hand, traditional solenoid fuel injection system suffered with lack of ability to operate under high speed applications mainly due to factors such as inertia; resulting in wear in valve seat, needle noise and unwanted vibrations. Thus, the exquisite magnetostrictive actuating capabilities at micron scale and the incompetence of traditional solenoid fuel injection system motivated this research to discover the possibility of implementing a magnetostrictive material, in this case *Terfenol-D*, in automotive fuel injection actuation. Specifically, the purposes of this study could be summarized as follows:

- To design a compressed natural gas fuel injector incorporating *Terfenol-D* as the magnetostrictive actuator material.

- To simulate the magnetic field generated by the coil in the injector to achieve the required magnetic field strength necessary for causing a predetermined strain in Terfenol-D member utilizing *Finite Element Method Magnetics (FEMM)* simulation software.

- To investigate the effect of both varying coil thicknesses and wire types on magnetic field strength and circuit properties.

- To verify the simulation results obtained from *FEMM* with that of *ANSYS Electromagnetic* simulation software.

- To predict the mass flow rate of CNG through the predetermined injector lift by the *computational fluid dynamics (CFD)* simulation software *FLUENT* utilizing several turbulent models.

1.3 Outline of thesis

This thesis is organized in eight chapters. A concise and inclusive overview of the highlighted research process is shown in figure 1.1. Each respective chapter in this thesis ends with a brief summary outlining the foremost achievements and findings. The remainder of this thesis is organized as shown:

Chapter Two:	This chapter incorporates a comprehensive literature review of various compressed natural gas fuel injection environments.
Chapter Three:	This chapter incorporates basic principles and properties of smart materials especially for MS material Terfenol-D.
Chapter Four:	This chapter incorporates the design concept and mechanism of a prototype CNG fuel injector. Besides, the actuating parameters required to initiate the electromagnetic and CFD simulations would be predetermined.
Chapter Five:	This chapter incorporates the discussion and analysis of FEMM simulation results.
Chapter Six:	This chapter incorporates the verification of FEMM simulation results with that of ANSYS Electromagnetic.
Chapter Seven:	This chapter incorporates the prediction of mass flow rate of the CNG fuel injector utilizing *standard* k-ε, *realizable* k-ε and *Reynolds Stress Model (RSM)* turbulent models in FLUENT CFD software.
Chapter Eight:	This chapter incorporates conclusions and highlights of the research contribution with recommendations for future research work.

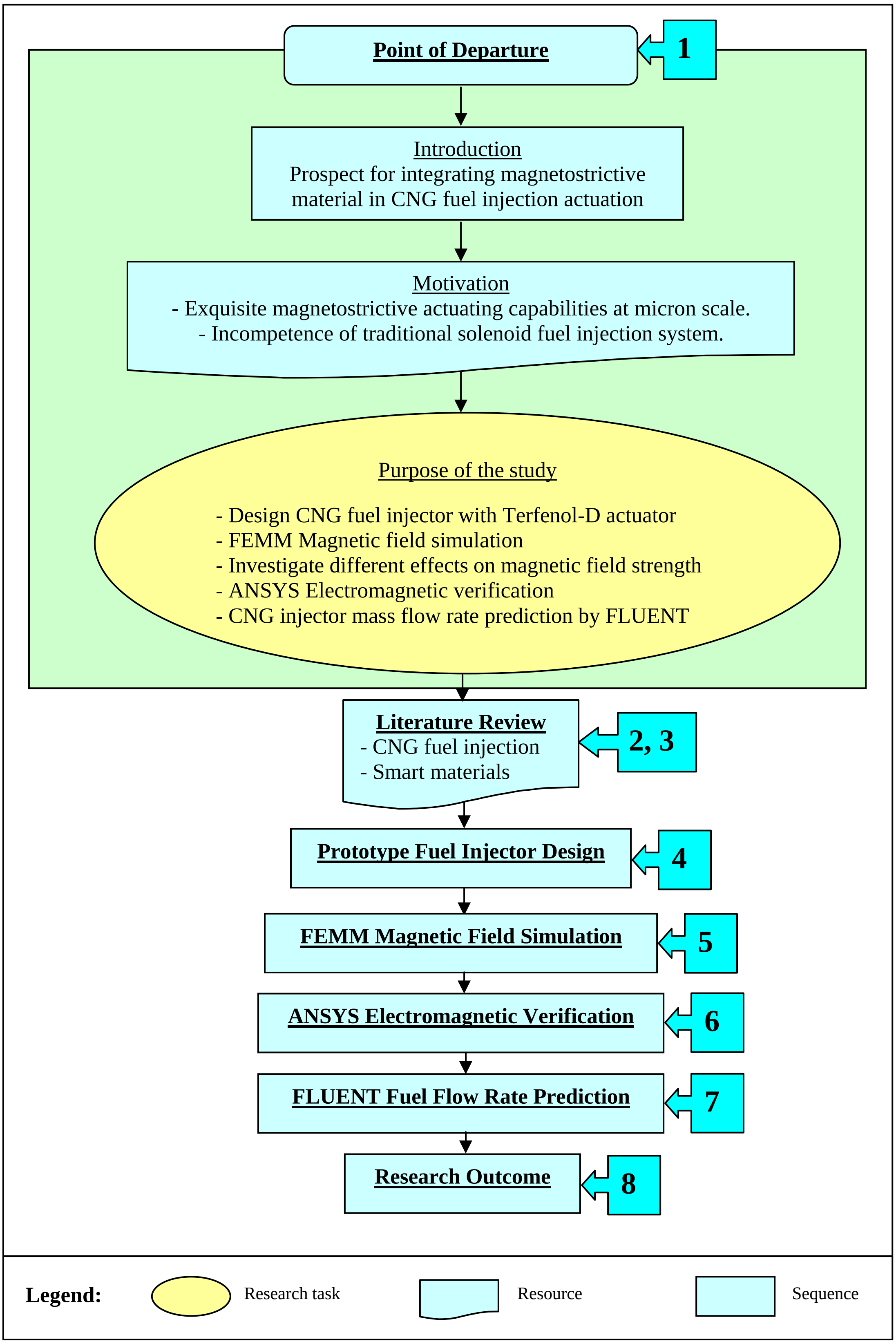

Figure 1.1: Summary of the research process in chapter one.

CHAPTER TWO

LITERATURE REVIEW
OF
CNG FUEL INJECTION
ENVIRONMENTS

2.1 Introduction

Natural gas vehicles (NGVs) can be made to operate only on natural gas or can be designed to run on either natural gas or gasoline. Generally, these spark-ignited or Otto-cycle engines are referred to as *bi-fuel* vehicles. On the other hand, diesel engines, which operate according to the principle of a *compression ignition* or *heat of compression* engine, can be run on a combination of natural gas and diesel fuel mixed inside the combustion chamber. In this case, small amounts of diesel fuel mixed with natural gas act as mini-spark plugs to allow the natural gas to ignite. Normally when the vehicle is idling, the engine will run totally on diesel fuel. But when the vehicle begins to move, natural gas begins to replace the diesel fuel, which in most cases can be up to about 80-85%. These are known as *dual-fuel* natural gas engines.

According to a classification by *European Natural Gas Vehicle Association* (ENGVA) [1], natural gas engine technology can be divided into two main categories, a) *Mono-fuel Technology*, and b) *Dual-fuel Technology*. Although optimal power-output, low particulate matter (PM) emissions, secured use of CNG infrastructure are some of the benefits that mono-fuel technology provides, high cost involved in engine development is a significant drawback. On the other hand, dual-fuel technology includes some benefits which incorporate low cost engine development, less CNG storage required compared to mono-fuel vehicle resulting in low vehicle weight, etc. However factors such as diesel power compromise, non-optimization of emission results and possibility of high fuel cost are some of the drawbacks of this technology.

This chapter is an attempt to gather major technological advancements regarding CNG utilization in automotive applications emphasizing on four basic configurations; a) *mono-fuel* (CNG only), b) *compression-ignition or diesel environment*, c) *spark-ignited or gasoline environment,* and d) *blending with hydrogen*.

2.2 Compressed natural gas

Natural gas is a naturally occurring gaseous mixture of hydrocarbons, mostly methane, and non-hydrocarbons produced from wells drilled into underground reservoirs of porous rock. Natural gas used as a transportation fuel is generally compressed to a very high pressure, typically 3000 psi or higher. This form of natural gas is classified as *compressed natural gas* (CNG). Moreover, natural gas can also be stored in a specific cryogenic tank in liquefied state referred as *liquefied natural gas* (LNG) [2]. Compared with other hydrocarbon products, such as methanol and ethanol, CNG is different in that it is a gas at normal temperatures and pressures, which requires different approaches to on-board fuel storage and vehicle refuelling operations. Furthermore, it also requires the fuel system to be entirely closed, eliminating significant environmental benefit. Vehicles using CNG fuel greatly reduce CO_2 and HC emissions [3].

As mentioned earlier, natural gas contains predominantly methane (95 to 99 percent) with the balance made up by other gases, such as ethane and propane [4]. Table 2.1 depicts some properties of CNG compared with other conventional fuels.

Table 2.1: Properties of some conventional fuels and CNG [4].

Properties		**Gasoline**	**Diesel**	**CNG (Methane)**
Energy content (Lower Heating Value) (MJ/kg)		44.0	42.5	50
Liquid density (kg/litre)		0.72-0.78	0.84-0.88	0.4225
Liquid energy density (MJ/litre)		33.0	36.55	21.13
Gas energy density (MJ/litre)	@ atmospheric pressure	N/A	N/A	0.036
	@ 2,900 psi pressure	N/A	N/A	7.47
Boiling point (^{o}C)		37-205	140-360	-161.6
Research octane number		92-98	25	120
Motor octane number		80-90	N/A	120

2.3 Dedicated natural gas engines (mono-fuel)

Contemporary natural gas engines do suffer significant efficiency reductions at part load and small reductions at full load from their diesel counterparts. These efficiency reductions can be ascribed to two primary factors, *reduction in compression ratio* and *throttling losses* [5]. Current lean burn spark ignited (SI) engine technology emphasises in increasing the part load efficiency through reduction or elimination of throttling losses. Among the different strategies, the following fuel injection techniques found to be widely used in case of dedicated natural gas vehicles. These are namely, *direct injection*, *port injection* and *single point premixed injection*. Direct injection might be preferable as the necessary level of fuel stratification is generally unachievable in case of port injection [5]. However, properly timed port fuel injection to achieve charge stratification in a chamber SI engine has also been attempted [6]. This approach was attractive because it did not force any significant modifications to the production engine. Yet, it was also unlikely to provide the level of stratification needed for throttleless operation under very light load conditions [7]. Therefore, it was found that, the development of fuel injection system was more towards in implementing the direct fuel injection strategy.

2.3.1 Direct injection

According to Cox et al. [8], the best long-term technology for alternative fuel engines was four stroke cycle and direct injected (DI) engine using a single fuel. This DI single fuel approach generally maximizes the substitution of alternative fuel for diesel and retains the thermal efficiency and power density of the diesel engine. Again, according to a CNG DI combustion research by Shiga et al. [9], it was shown that stratified combustion with extremely lean burn capability can be realized with CNG direct injection.

2.3.1.1 Direct injection strategies

For the reason that there is no liquid phase present in case of compressed natural gas (CNG) direct injection stratified combustion, no wall wetting exists.

Thus, comparing with the gasoline direct-injection engine, a smaller excessively fuel rich volume can be expected. Furthermore, a greater charging efficiency could be achieved than that of a port injection type or gas mixer type CNG engine because the fuel can be injected after closing the intake valve [10]. However, some pressure enhancement devices might be necessary to inject the fuel into a high-pressure cylinder from the CNG storage when its pressure becomes lower than the required injection pressure.

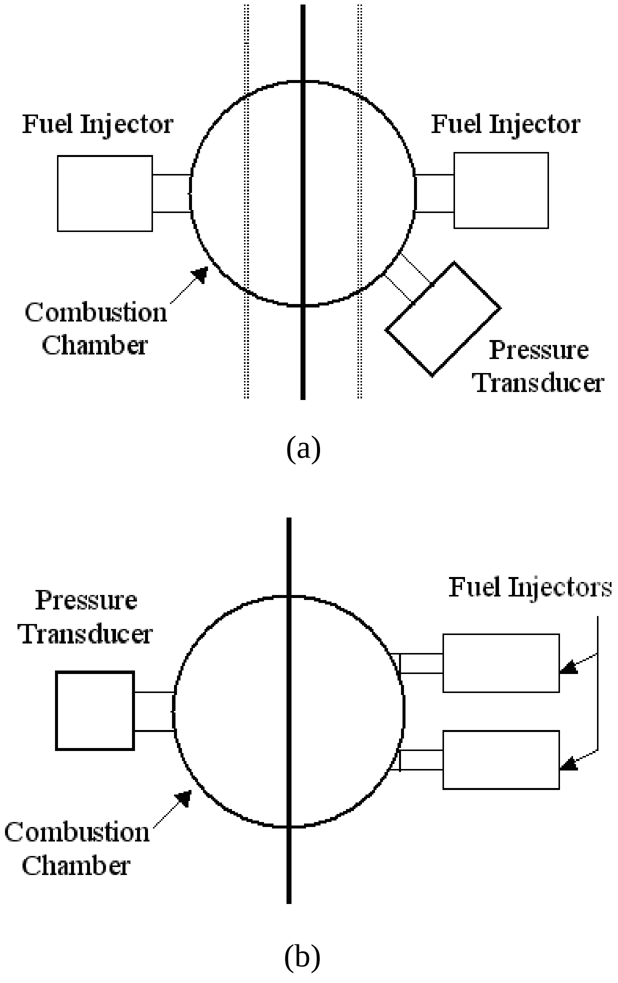

Figure 2.1: Arrangements of the fuel injectors and the spark gap [9]; (a) opposed and single injection, spark gap at centre and halfway between centre and wall, and (b) parallel injection with spark gap at centre.

As shown in figure 2.1, for a centrally positioned spark gap, the two injectors are generally set at two different locations generating greater mixing between the gas fuel, air and the combustion products due to the mutual impingement of the gas which would result in better utilization of air and internal EGR. The injector locations are cited as *opposed injectio*n and *parallel injection* as shown in figure 2.1 (a)-(b), respectively. In *single injection* strategy, the spark gap is generally set halfway between the centre and the sidewall (near the injector tip) and the fuel is injected through the injector closer to the gap [9].

According to Kubesh [7], *direct-injection stratified charge* (DISC) approach was felt to be the best option for allowing throttleless operation with the lowest emissions penalties relative to a *homogeneous charge spark-ignited* approach. The DISC approach would also facilitate a hybrid stratified charge or homogeneous charge approach to accommodate medium to high load operations. The strategy was to mount the prototype injector in the normal spark plug location, and the spark plug was relocated to the opposite side of the head with a special adapter sleeve. The piston was redesigned to incorporate a divided bowl structure. The fuel injector had a nozzle with a large, single hole that vectored the fuel directly down into the primary combustion bowl. The basis of their direct injector design was a fuel metering system development for a pre-chamber natural gas engine [11], which was adapted for use in a direct injection environment. The fuel injector assembly was composed of several parts, such as an adapter for mounting the injector in spark plug hole, a nozzle, an injector body containing the check valve, and the metering unit. The injector was held in the adapter underneath a threaded jam nut. The nozzle was readily positionable and replaceable since it was attached to the injector body by a threaded sleeve. Each of the metering units was designed to be interchangeable with the remaining injector hardware. The metering units could be disassembled from the injector through compression fitting between the two pieces. The metering unit also contained the temperature and pressure sensors for calculating fuel density to provide control of fuel mass per injection. Two computer models, namely *JETMIX* and *INFLOW*, were used which assisted in designing the injector and nozzle. JETMIX was used to analyze the injection flow pattern obtained from the injector nozzle, while INJFLOW was used to analyze the flow and restrictions within the injector [5].

2.3.1.2 Timings of fuel injection and ignition

For a CNG direct injection combustion study by Shiga et al. [9], the ignition timing was fixed at 80 ms from the start of compression for all conditions and the fuel injection timing was varied to ensure stable ignition. The injection timing for twin injectors was set at 60 ms from the start of compression when the equivalence ratio was greater than or equal to 0.6. Then again, the injection timing for a single injector was set at 50 ms from the start of compression when the equivalence ratio was greater than or equal to 0.6. However, when the equivalence ratio was less than 0.6, the injection timing was adjusted to give the best ignitability for the two kinds of twin injection and the single injection.

2.3.1.3 Fuel injector

Precisely controlled flow of fuel vapour happens to be the focus of injector design. Fuel injectors that utilise control valves that are opened and closed by electrical solenoids, are widely used for injecting fuel into internal combustion engines. In such devices, the actuating parts are subject to considerable impact forces causing wear even in most highly durable materials. Then again, when the fuel is gaseous, lubrication and viscous damping could not be afforded. Thus, design requirements for gaseous fuel injectors involve self-lubrication, impact damping and enlarged injector orifice size.

According to the study by Liu et al. [12], a higher injector component life was ensured by fabricating the ball valve and introducing motion stops for the reciprocating armature. The surface against which the armature slides was also fabricated from a highly durable, low friction, impact cushioning, resilient plastic material. Furthermore, the ball valve was placed above the armature and its seat so that the ball was normally seated in its closed position and was driven to the open position by the armature to minimize the inertia effects at closing. Basically, when the coil was energized, the armature was driven upward against the valve end surface which in turn opened the valve. With the coil energized, the upper surface of the armature was put against the stop member on the bottom surface of the inner housing which limited the upward travel. When not energised, the spring forced the ball and the armature downward to a closed position.

2.3.1.4 Injector driver

In case of direct injection, two types of injector drivers were mostly found to be used; these are *peak hold drivers* and *saturated drivers*. The saturated and peak hold drivers generally designed for high and low impedance injectors respectively [12].

2.3.1.5 Nozzles

For CNG applications, two types of nozzle were mostly found to be used; these are a) *NGV1*, and b) *NGV2*. For smaller and larger sized vehicles, NGV1 and NGV2 were used respectively [13]. In addition, a brief discussion regarding a) *three-hole nozzle*, and b) *five-hole nozzle* would be presented at this juncture.

Basically, a three-hole nozzle features a small centre hole that points at the spark plug, as well as a larger hole on either side of the centre hole. A five-hole nozzle while retaining the same total flow area as the three-hole nozzle, the spray pattern spreads over a larger area and the hole size of the largest holes are noticeably less than those of the three-hole nozzle. However, the five-hole nozzle generally features the same size centre hole as the three-hole nozzle [5].

According to a study by Podnar and Kubesh [5], reliable combustion with the three-hole nozzle was only achieved with early cycle injection, such as injection during the intake stroke. When late cycle injection was attempted, inconsistent combustion such as many misfiring or near misfiring cycles, or no combustion was observed which was found to be true over a variety of *end of injection* (EOI) timing and spark timing value combinations. This might be due to the reason that the engine might be firing under a homogeneous charge mode and that stratified charge combustion was not achieved. However, with the five-hole nozzle, in addition to stable combustion in the early cycle injection mode, late cycle injection over a specific range of EOI and spark-timing combinations also yielded stable combustion.

2.3.2 Stratified charge combustion

It is necessary to stratify the fuel-air charge so that an ignitable mixture can be achieved near the spark plug at the time of ignition in order to achieve throttleless SI operation over an entire engine operating range. Some feasible methods to accomplish this requirement generally include, a) *port injection open chamber combustion approach,* b) *pre-chamber combustion approach,* and c) *direct injection open chamber approach.*

As mentioned earlier, port fuel injection open chamber combustion would be attractive from the perspective of not forcing significant modifications to the production engine. However, this approach was unlikely to provide the level of stratification needed for throttleless operation at significant light load conditions.

Although a great deal of work has been done using the prechamber combustion approach with natural gas in order to achieve extremely low emissions and high efficiency, it was found that in order to achieve throttleless operation over the entire operating range, a much larger prechamber, such as 10% or more of the main chamber volume would be required. Research experiences with engines having prechambers this large showed that these engines suffered significant emissions penalties [5]. For this reason, a traditional prechamber approach was determined to be inappropriate for several engine applications.

Considering these inconveniences, the DISC approach was felt to be the best option for allowing throttleless operation resulting in high efficiency with the lowest emissions penalties relative to a homogeneous charge SI approach. This approach also accommodated the transition into the traditional homogeneous charge approach, or a hybrid stratified charge and homogeneous charge approach for medium to high load operation. For this reason, the DISC approach seemed to be the focus of the stratified charge combustion system development effort [5,7].

2.4 Compressed natural gas in diesel environment

Generally, diesel cycle engine utilizes natural gas according to two following ways, a) *with diesel pilot-ignition*, and b) *using hot surface or glow plug ignition*.

2.4.1 Pilot ignited high pressure direct injection of natural gas

Diesel cycle engine with diesel pilot ignition was an effort to reproduce the diesel combustion cycle with natural gas. In this technology, a number of pilot diesel sprays provided multiple ignition sites for the directly injected natural gas. As an ignition source, only a small quantity of diesel pilot was found to be used, such as from 2% to 5% at high loads, where the gas injection pressure being roughly between 19 and 25 MPa. Some major advantages of this technology included retention of the efficiency of the diesel platform, maintenance of torque capability of the base diesel engine, resistance to knocking at the presence of natural gas of varying qualities and reduction in NOx, PM and CO_2 emissions compared to the diesel baseline [14].

2.4.1.1 Diesel pilot injection strategy

According to a study regarding this technology yielded that the original diesel injector was replaced by a new common rail type injector capable of injecting a small quantity of pilot diesel fuel and a main charge of natural gas at the end of compression stroke. Each injector incorporated two solenoid controlled valves, each controlling the injection timing and the metering of one of the fuel to the combustion chamber. A diesel pump provided diesel fuel to a rail at a pressure of approximately 25 MPa. Natural gas was supplied to a parallel rail at the same pressure. The rails were balanced with a dome-loaded regulator to minimize leakage of one fuel into the other within the injector. The pilot quantity remained roughly constant independently from the load and varied between 9% and 2.4% when the load increased from 20% to 100% [14]. Figure 2.2 depicts the general working principle of diesel pilot ignition with CNG direct injection.

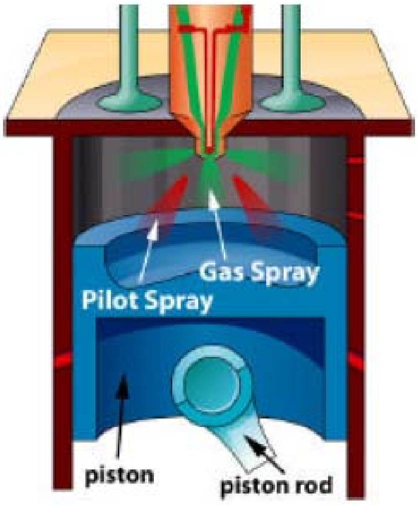

Figure 2.2: Schematic of diesel pilot ignition with natural gas DI.

2.4.2 Direct injection with hot surface ignition

Direct injection with hot-surface ignition technology was found to be an attempt to provide some significant benefits, such as diesel-like efficiency and torque with low emission, while simplifying the fuel injection system. This technology also offered single refuelling step and potential for improved emissions as no diesel fuel was used. Also according to Fukuda et al. [15], directly injected natural gas can be successfully ignited by glow plugs.

2.4.2.1 Hot surface ignition strategy

The basis of glow plug ignition is the initiation of combustion by heat transfer from a high temperature surface in excess of 1200°C [16-22]. A hydraulically driven compressor is generally utilized to deliver high pressure CNG to common-rail injectors at 20 to 25 MPa. A hydraulic pump is generally installed instead of the original diesel pump, which could either be a *common rail* or a *pump line nozzle* type. A spool valve generally controls the flow of hydraulic fluid to and from the pump and compressor tubes. A reservoir and optional hydraulic cooler are generally included also. The engine controller usually has the task to monitor and control the injector driver, glow plug driver and the compressor. The injector is generally based upon direct actuation of a gas needle. In this case, a magnetostrictive actuator could be the best option due to its high durability and simple construction. Furthermore, the hydraulic compressor has the task to compress natural gas from the main tank, providing the ability to remotely mount the compressor away from the engine.

Basically, the initial ignition occurs in the thin layer of the glow plug where the air/fuel mixture reaches ignition temperature. The flame propagation generally starts from the surface of the glow plug. Special shields around the glow plug are employed to limit cooling due to the air and CNG jet flow fields. Intake airflow, particularly at high speeds, and the high-speed CNG jet usually have a pronounced effect on cooling of the surface of the glow plug. However, this is significantly critical as excessive cooling requires higher power levels and eventually shortens the life of the glow plug. A sample glow plug ignition configuration is depicted in figure 2.3.

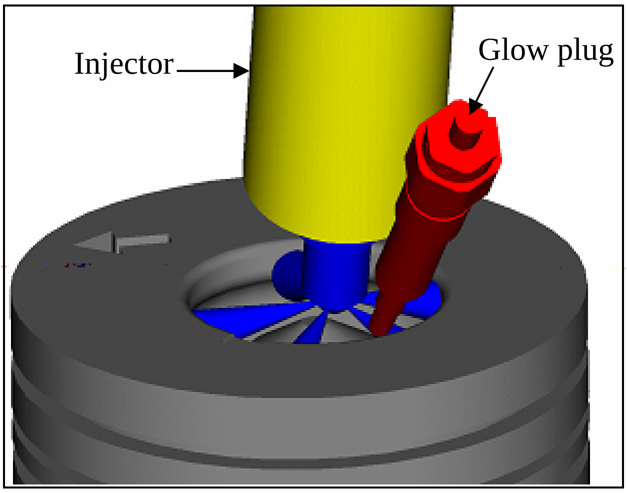

Figure 2.3: Glow plug ignition.

It was found that, the foremost challenge of diesel pilot ignition was to develop an injection system that would provide both high-pressure gas and pilot diesel fuel. Thus, the necessities exist for a high-pressure gas injector or a combined injection valve, which would inject both the main natural gas charge and the pilot diesel with a high-pressure gaseous fuel supply. However, for hot surface or glow-plug ignition, challenges similar to the direct injection spark ignited engines are to be expected, since the right mixture has to be developed before the ignition at a wide range of loads and speeds. In addition, continuous operation of the glow plugs at higher temperature is yet another challenge of this technology. These challenges were confirmed to various extents by several researchers that have been active in this area, such as Caterpillar researchers [8,23,24], Mitsu [25], Shioji et al. [26] and Bartunek and Hilger [27].

2.4.3 Dual-fuel diesel engine with induced natural gas

The operating range of a lean premixed compression ignition engine is limited to higher excess air ratios because of the difficulties with both control of ignition timing and knocking, although smokeless and ultra low NOx combustion has been established with this technique [28-30]. A dual-fuel diesel engine, where an induced natural gas acts as the main fuel with resistance to self-ignition and a small quantity of diesel acts as the ignition source, has got excellent prospects to control ignition timing and to realize the formation of rich and lean biform mixture composition [31-33]. It eventually avoids near stoichiometric and extremely over-rich regions. Furthermore, this technique helps to suppress NOx formation without smoke increase when the overall excess air ratio approaches the stoichiometric. However, knocking and misfiring might be some problems associated with it when the percentage of inducted fuel is increased. According to a research by Ogawa et al. [34] have established smokeless and ultra low NOx combustion without knocking over a wide operating range in such a dual-fuel engine. At several IMEP conditions, they investigated the optimizations of the combustion chamber shape and operating factors, including *exhaust gas recirculation* (EGR) and intake air throttling.

2.4.3.1 Dual-fuel diesel engine with induced NG strategy

In this technique, natural gas is continuously induced into an intake manifold upstream from the cylinder head. Furthermore, a small amount of conventional diesel fuel is directly injected into the combustion chamber to act as the ignition source from a common rail fuel injection system, as shown in figure 2.4. A lean quasi-homogenous mixture is generally formed with induced natural gas in the combustion chamber.

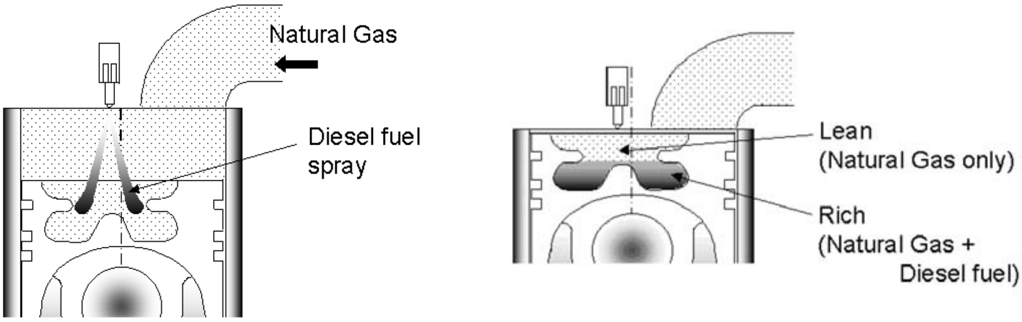

(a) (b)

Figure 2.4: Concept of biform mixture formation in different piston cavity space in a dual-fuel engine [34]; (a) Diesel fuel injection at 60° CA BTDC, and (b) Biform mixture formation at end of compression.

According to a study performed by Ogawa et al. [34], the injection timing of the diesel fuel was set at 60° CA BTDC, which was relatively an earlier timing to prevent an extremely rich mixture and smoke formation. It was also expected that a slightly richer than stoichiometric mixture was to be formed in the lower part of the cavity, and a leaner mixture in the upper part. The fuel injection nozzle had four holes typically 0.21 mm in diameter, while the spray hole cone angle was 40°. A throttle valve was installed in the intake manifold to control the overall excess air ratio. The piston had an interchangeable piston crown and cavity allowing the use of two different piston cavity shapes, namely *divided* and *ordinary toroidal* cavity. The piston cavity was divided by a lip in the sidewall, as shown in figure 2.4, which was suitable to confine diesel fuel into the lower part of the cavity, and this suppressed knocking just after ignition. The results of their experiments showed that a combination of the divided cavity, exhaust gas recirculation and intake air throttling was effective to simultaneously eliminate knocking and reduce *total hydrocarbon* (THC) and NOx over a wide IMEP range.

2.4.4 Natural gas combustion assisted with gas-oil in a diesel engine

For the purposes of reducing NOx and smoke, and to achieve significant improvement of trade-off between smoke and NOx without deteriorating fuel consumption, natural gas is generally charged homogeneously into the intake air and is burned by igniting a small amount of gas oil injection. According to a study by Ishida et al. [35], a high burning rate of natural gas resulted in shortening the combustion duration, subsequently leading to lower fuel consumption. Generally, if the burning rate of natural gas is too high, it results in increase of NOx. In contrast, too low burning rate results in increases of fuel consumption and THC. By raising the intake charge temperature up to 120°C, which increased the burning rate of natural gas, they managed to drastically improve the fuel consumption and THC. Increase in NOx due to high burning rate of natural gas at the high load was mended by lowering the intake charge temperature below 60°C, which suppressed the burning rate of natural gas. Besides, high EGR rate showed suppression effect on the burning rate at the high load. However, the burning rate was found to be hardly affected by EGR at the low load. Eventually, NOx was reduced effectively by EGR without deteriorating fuel consumption, which was thought to be due to the water content brought by EGR as well as the decrease in oxygen concentration of the intake charge.

2.5 Compressed natural gas in gasoline environment

Due to some of its favourable physio-chemical properties, CNG appears to be an excellent fuel for the spark ignition (SI) engine. Moreover, SI engines can be converted to CNG operation quite effortlessly as a second fuelling system.

2.5.1 CNG as an alternative fuel for a retrofitted gasoline vehicle

The development of new dedicated natural gas vehicle (NGV) is very difficult within a diminutive time, as it requires new ignition, combustion, injection and engine control system. Therefore, after market conversion or retrofitting happens to be the realistic way to increase CNG based bi-fuel vehicles [36]. As a consequence, in order to satisfy customer demand, vehicle manufacturers are more interested in converting gasoline engines into bi-fuel ones rather than producing new-dedicated NGVs [37]. Also from a study, it was found that, on average retrofitted CNG engine reduces CO by around 80%, CO_2 by 20% and HC by 50% compared to gasoline [36].

However, retrofitted NGV engine produce about 10–15% less power than the same engine fuelled by gasoline [38-40]. Jones and Evans [41] measured a total power loss of approximately 15% and efficiency drop of 5% when changing from gasoline to CNG. 10% loss of power was attributed due to reduction in the inhaled energy and the remaining 5% to the lower burning velocity of CNG compared to gasoline. Aslam et al. [36] also concluded from their study that retrofitted CNG engine produces round 16% less *brake mean effective pressure* (BMEP) and consumes 17–18% less *brake specific fuel consumption* (BSFC), or consumes an average of 1.65 MJ less energy per kWh at *wide open throttle* (WOT) condition with CNG compared to gasoline. In another comparative study of performance and exhaust emissions by Evans and Blaszczyk [42], it was also observed that the BMEP and BSFC were both 12% lower with CNG at WOT condition. Another study by Hamid and Ahmad [43] presented a comparison of the NGV and gasoline base engine performance where they found the volumetric efficiency of the NGV engine was reduced by about 15% and overall performance lowered by circa 9% at maximum torque and maximum power conditions.

2.5.2 Natural gas direct injection in spark ignited Otto cycle engine

This technique is similar or equivalent to some extents with *gasoline direct injection* (GDI). It provides an efficiency enhancement by reducing throttling losses. This is generally achieved by the precise control over amount of fuel and injection timings that are varied according to the load conditions. Basically, the engine management system continuously chooses between three different modes of combustion - *ultra lean burn combustion, stoichiometric combustion* and *high power output mode*. In addition, this method avoids the volumetric efficiency loss that is caused by the presence of low-density natural gas in the intake manifold. But several challenges regarding the control of NOx and hydrocarbon emissions are evident, as in the case of GDI engines mentioned in many research works by Southwest Research Institute [5,7], Goto and Sato [44,45] from Japanese traffic Safety and Nuisance Research Institute, and Arcoumanis et al [46] from Imperial College.

2.6 Compressed natural gas and hydrogen

A possible approach for meeting future emission regulations with current natural gas engine design is to blend hydrogen with compressed natural gas (CNG). This would allow leaner air/fuel ratio and retarded spark timing [47]. Despite its low energy density, hydrogen can improve engine performance at very lean engine operation, because it releases more energy per unit oxygen consumed. Moreover, the increased flame speed and lean combustion ability of hydrogen would enhance the combustion efficiency significantly. Altogether, the lean air/fuel ratio and retarded timing can reduce NOx considerably without the use of exhaust gas after-treatment equipments.

Early research on hydrogen enrichment was focused on fuels such as gasoline and iso-octane [48,49]. These experiments established the effectiveness of hydrogen in extending the lean operating limit as well as reducing NOx emissions and increasing thermal efficiency. Later studies of hydrogen enrichment have focused on natural gas utilizing lean-burn, spark-ignited (SI) engines [50-53]. According to a study undertaken by *National Renewable Energy Laboratory* (NREL), USA [5], which involved H/CNG blend for transit buses, it was concluded that minor engine and vehicle hardware modifications were required for the 20/80 H/CNG operation. The modifications were the addition of a new fuel mass flow rate sensor and additional vehicle fuel tanks. However, the fuel economy was reduced by about 12% relative to the CNG operation on a diesel gallon equivalent basis.

2.6.1 Hydrogen assisted jet ignition (HAJI)

Hydrogen assisted jet ignition (HAJI) is commonly used to achieve reliable combustion and low NOx emissions. It is a system developed by *Transport Energy Group, University of Melbourne* [54], which replaces the spark plug in a conventional spark ignition engine and virtually eliminates the lean limit. HAJI primarily consists of, a) *a small prechamber* which is approximately 0.7% of the TDC main chamber volume, b) *a hydrogen injector*, and c) *a spark plug*.

2.6.1.1 HAJI strategy

In this technique, Hydrogen is generally injected into the pre-chamber prior to ignition. Stable and repeatable ignition is guaranteed by the wide flammability limits of H_2. The increased pressure from combustion forces the ignited hydrogen gas through a number of orifices into the main chamber. The presence of highly reactive partial products and turbulence generally causes the resulting jets to have an energy level at least two orders of magnitude higher than that of a spark [55]. In the main chamber, the fuel is then ignited by these jets in a stable and reliable manner, as shown in figure 2.5.

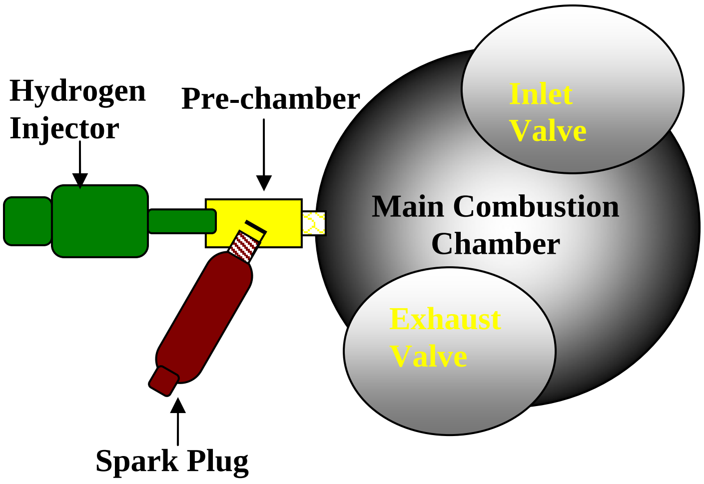

Figure 2.5: Schematic of hydrogen assisted jet ignition.

A HAJI-equipped engine could be run as lean as relative air/fuel ratio, $\lambda = 5$ resulting in an *Ultra Low Emissions Vehicle* (ULEV), without the need for complex and expensive exhaust after treatment. An additional benefit is that the work per cycle could be reduced to no load quantities by simply increasing the air/fuel ratio. Since there is effectively neither a lean limit nor the need for a catalytic converter, this eventually results in the reduction of pumping losses that has been estimated to improve efficiency by around 20% [56].

Current research work regarding a HAJI-equipped engine is focused on reducing the hydrocarbon (HC) emissions. According to Lawrence [57], these HC emissions were largely due to quench and crevice. As the air/fuel ratio was increased, the proportion of total emissions contributed by crevice was decreased even though the absolute quantity of crevice emissions increased. In contrast, an increased air/fuel ratio resulted in increased quench emissions both proportionally and absolutely. This was attributed to quench being more strongly influenced by a reduction of peak temperatures than crevice. In order to reduce both crevice and quench emissions, fuel stratification facilitated by direct injection was suggested. From another study by Wang and Watson [54], it was concluded that negligible levels of CO and NOx emissions were preserved with the introduction of CNG direct injection while fuel stratification was minimally achieved by direct injection. However, the reduction in exhaust HC was mainly attributed to a reduction in crevice emissions. They also recommended that in order to get better fuel stratification, a dual opposing injection strategy, either with or without induced swirl, might be helpful.

2.7 Summary of chapter two

Although present alternative fuel technologies might be sufficient to meet the current emission reduction legislations, continuous in depth research regarding new and improved fuel injection systems are quite indispensable to meet any future emission standards. In this context, due to their enormous potential regarding sensing and actuating capabilities, smart materials such as *magnetostrictive* (MS), *piezoelectric* and *magnetorheological fluid* (MRF) possess tremendous prospect in developing different types of actuator design concepts [58]. The following chapters will focus on designing a compressed natural gas fuel injector utilizing such a material as an actuator in order to step towards a more efficient fuel injection system compared to the traditional solenoid injection one. A concise and inclusive overview of the highlighted research process of this chapter is shown in figure 2.6.

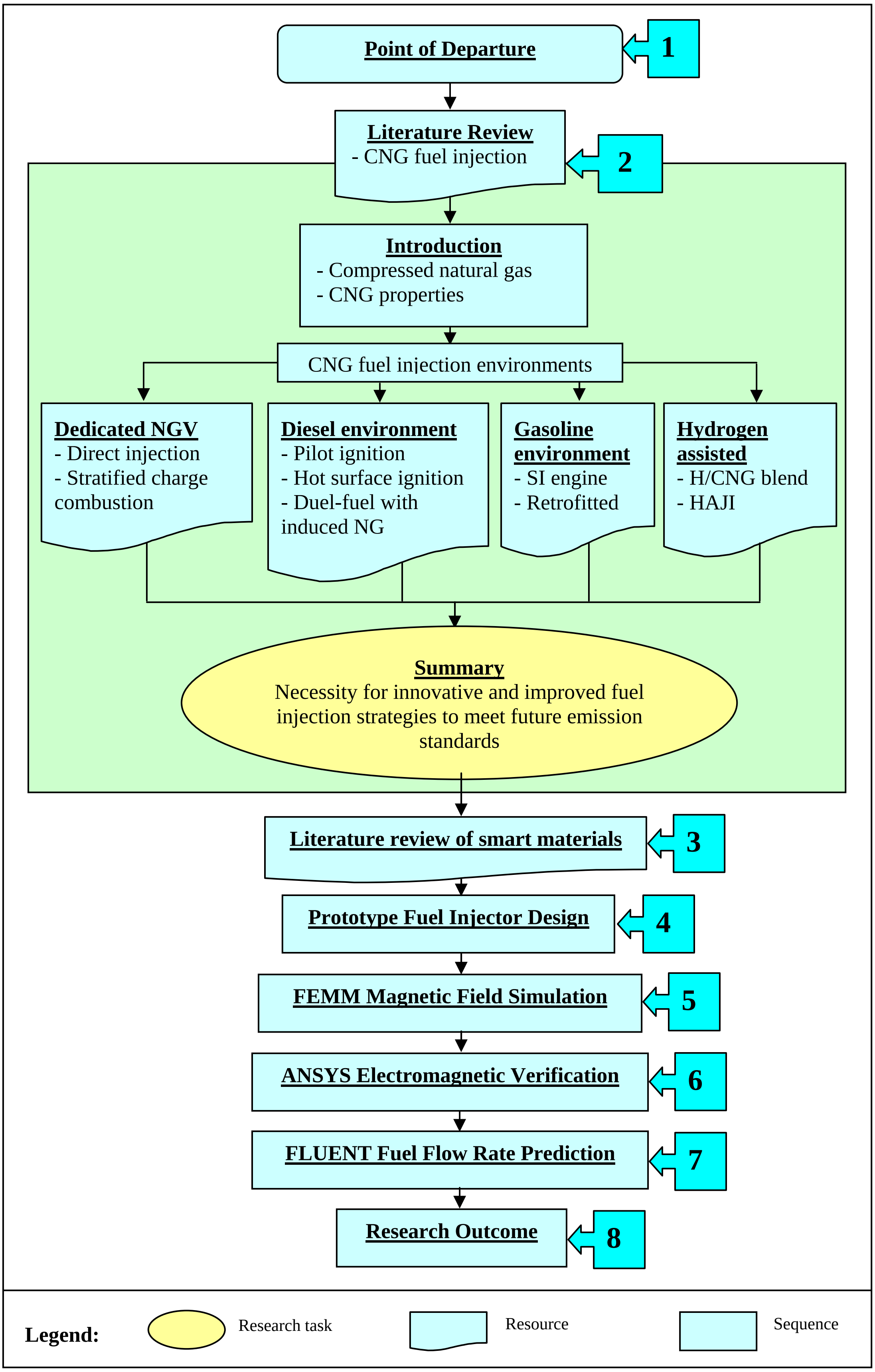

Figure 2.6: Summary of the research process in chapter two.

CHAPTER THREE

LITERATURE REVIEW
OF
SMART MATERIALS

3.1 Introduction

Materials that possess the ability to perform both sensing and actuating functions are generally defined as *"smart"* [59]. Hence, magnetostriction or piezoelectricity is the changing of physical dimensions of materials, such as most ferromagnetic materials, piezo-crystals and certain ceramic material, in response to changing its magnetization. In other words, a magnetostrictive or piezoelectric material will change shape when it is subjected to a magnetic field or an externally applied voltage. A passively smart material has the ability to respond to environmental conditions in a useful manner showing a distinction from an actively smart material in that there are no external fields, forces or feedback systems used to enhance its behavior.

This chapter will highlight different aspects of smart materials, especially in case of magnetostrictive material, mechanism of magnetostriction and their prospect for fuel injection actuation. In addition, a detailed investigation regarding the material and magnetic properties of magnetostrictive material *Terfenol-D* will also be performed. Furthermore, some discussions regarding the production and non-linear characteristics of piezoelectric materials will also be presented.

3.2 Actuator Materials

Materials that show the highest known magnetostriction are those of cubic laves phase iron alloys containing the rare earth elements Dysprosium, Dy, or Terbium, Tb; $DyFe_2$, and $TbFe_2$. However, these materials have tremendous magnetic anisotropy which requires a very large magnetic field to drive the magnetostriction. Noting that these materials have anisotropies in opposite directions, Clark [60] and his co-workers at *NSWC-Carderock* prepared alloys containing Fe, Dy, and Tb which are generally stoichiometric of the form $Tb_xDy_{1-x}Fe_y$ (where y = 1.9 to 2) referred as *Terfenol-D*. For example, Terfenol-D ($Tb_{0.3}$ $Dy_{0.7}$ $Fe_{1.9}$), is capable of approximately 10 μm displacements for every 1 cm of length exposed to an approximately 500 Oersted magnetizing field.

Also, *Lead Zirconate Titanate* ($Pb[Zr_xTi_{1-x}]O_3$ $0<x<1$) or PZT is a ferroelectric ceramic perovskite material that shows a marked piezoelectric effect. Like structurally similar lead scandium tantalate and barium strontium titanate, PZT possess good prospects for manufacturing actuator devices due to lower material cost and improved performance.

For typical transducer and actuator applications, Terfenol-D is the most commonly used engineering magnetostrictive material [61] and in the case of fuel injection actuation, it offers exquisite potential. Earlier alloys exhibited large magnetostriction, but either at very large magnetic fields or at cryogenic temperatures. Terfenol-D overcame the temperature difficulty by incorporating RFe_2 microstructure which raised the *Curie temperature* above room temperature. The necessary magnetic field was reduced by balancing the ratio of Terbium and Dysprosium, two elements with oppositely signed magneto-crystalline anisotropy, such that effective anisotropy of the compound was near zero at room temperature. Since this time, Terfenol-D has become the foremost magnetostrictive material, although research continues into new materials constantly [62].

In this context, Xie et al. [63] prepared well-aligned pseudosingle crystals of a series of Terfenol-D using the *Czochralski* method by which grain-aligned rod can be prepared in one relatively speedy operation. The effects of several parameters, which included pulling rate, heat treatment and start material purity on the magnetomechanical coupling factor (k_{33}) of the samples, was investigated in their work. Their grown Terfenol-D rods showed high k_{33} values without subsequent heat treatment. Magnetomechanical coupling coefficients are further discussed in section 3.5.3.

Researchers recently investigated another material which is an iron/gallium alloy termed *Galfenol* by its inventors at the Naval Surface Warfare Center (Clark et al.). Studies performed with these alloys showed that magnetostriction peaked in iron/gallium alloys at a volume fraction of 17% gallium. Single crystal Galfenol exhibited magnetostriction on the order of 400 ppm at low applied fields. In addition, unlike Terfenol-D, Galfenol is tough and may be machined and used in devices where Terfenol-D may fracture. While the magnetostriction mechanism in

Galfenol is still under investigation, the magnetostriction seemed to be more similar to the classic magnetostriction of iron and nickel than the newer giant magnetostrictive alloys [62].

3.3 Mechanism of Magnetostriction

Magnetostriction is the deformation that spontaneously occurs in ferromagnetic materials when an external magnetic field is applied [64]. The magnetic phenomenon providing transducer capabilities generally incorporates, a) *the Joule Effect*, which is the change in dimension of magnetostrictive materials due to a change in magnetization; b) *the Villari Effect,* which is the reciprocal behavior of Joule effect in which the variation of state of stresses produce a change in magnetization; c) *the Wiedemann Effect*, which is manifested as a twisting in the sample material due to a helical magnetic field; d) *the Matteucci or inverse Wiedemann Effect*, which is the creation of a helical anisotropy of the susceptibility of a magnetostrictive material when subjected to a torque [65]. Among other magnetostrictive effects, the two most widely used ones are the Joule effect and the Villari effect. Firstly, the Joule effect can be represented by the equation:

$$S = c^{H}\sigma + dH \tag{3-1}$$

In the Eq.(3-1), S is the mechanical strain, c^{H} [m²/N] is the compliance coefficient at constant field strength and d [m/A] is the magnetostrictive constant at constant stress. Subsequently, the Villari effect can be represented as

$$B = d\sigma + \mu^{\sigma} H \tag{3-2}$$

In the Eq.(3-2), B is the magnetic flux density in Tesla, d is the magnetostrictive constant in m/A, σ [Pa] symbolizes the stress change and μ^{σ} [N/A²] is the permeability at constant mechanical stress. The magnetic field strength, H, could be calculated using:

$$H = \frac{IN}{l} \tag{3-3}$$

In Eq.(3-3), I is the current [A], N is the number of coil turns and l [m] is length of the magnetic path.

According to a review by Ekreem et al. [66], the nature of magnetostriction could be explained as illustrated in figure 3.1, which relates to the Joule Effect of magnetostriction. It shows a rod of a magnetic material of length L surrounded by a coil of wire carrying an electrical current so that a magnetic field, H, is produced along the rod [67]. The length of the rod increases by a small amount, ΔL, with the current flowing and the strain $\Delta L/L$ is termed as *magnetostriction* (λ). Figure 3.1 (a) also shows that in addition to an increase in length in the direction of the field, there is also, usually a decrease in length in the perpendicular directions, and consequently, the volume of the rod remains almost constant. Figure 3.1 (b) also explains two significant characteristics of magnetostriction. Firstly for high values of H, λ eventually reaches a constant value λ_{sat}, which indicates saturation, and secondly the sign of λ does not change when the field H becomes negative. As a result, the rod increases in length for both positive and negative values of the magnetic field strength [68]. Thus, the dependence between saturation magnetization and magnetostriction can be treated as quadratic [69,70].

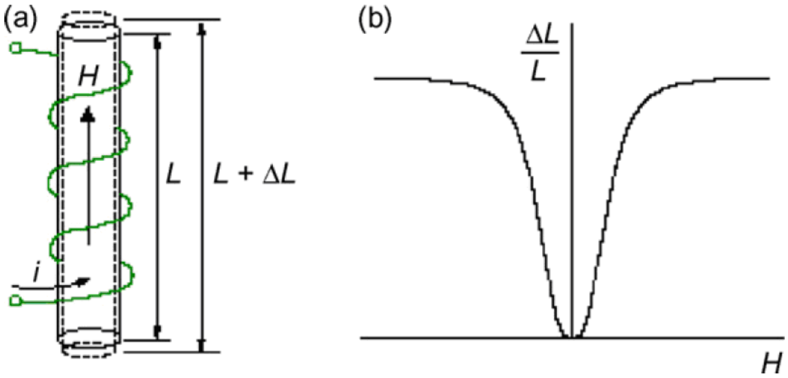

Figure 3.1: Joule magnetostriction. (a) The changes in shape in response to the magnetic field H. H is proportional to the current that passes through the solenoid. (b) The relationship between ΔL/L and H [66].

Although the mechanism of magnetostriction at an atomic level is relatively complicated, on a macroscopic level, however, it may be isolated into two distinct processes. While the domination of the migration of domain walls within the material in response to external magnetic fields is the first process, the second one is the rotation of the domains themselves. These two mechanisms allow the material to change the domain orientation which sequentially causes a dimensional change. The re-orientation of magnetic domains can be represented schematically, as shown in figures 3.2 and 3.3. In the region between 0 and 1, where the applied magnetic field is small, the magnetic domains show almost no common orientation pattern. However, depending on the way that the material was formed, there might be a small amount of a common orientation pattern, which would show itself as a permanent magnet bias. In addition, the resulting strain depends very much on how homogeneous the base structure of the magnetostrictive material is, besides the material formulation. Then, in the region 1–2, ideally there should be an almost linear relationship between strain and magnetic field, which eventually makes it easier to predict the behavior of the material. However, beyond point 2, the relationship becomes non-linear again as a result of the fact that most of the magnetic domains have become aligned with the magnetic field direction. The saturation effect is predominant at point 3, which prevents further strain increase [71].

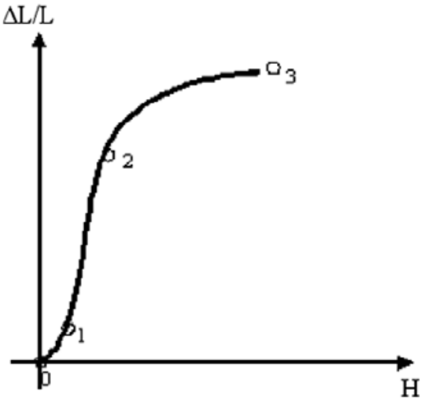

Figure 3.2: Graphical representation of strain vs. magnetic field (idealized behaviour) [71].

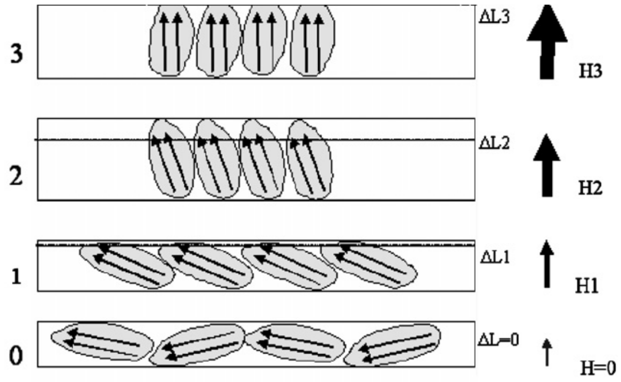

Figure 3.3: Schematic of strain vs. magnetic field [71].

During this stretching process, the cross-section of the material is reduced in such a way that the volume is kept nearly constant or the volume change is so minute that it can be neglected under normal operating conditions. Thus, the deformation can be termed as isochoric. Again, applying a stronger magnetic field leads to stronger and more definite re-orientation of increasingly more domains in the direction of magnetic field and when all the magnetic domains have become aligned with the magnetic field the saturation point is considered to be achieved. Thus, the basic theme of magnetostriction remains that the rotation and movement of magnetic domains causes a physical length change in the material.

Modern magnetostrictive materials, such as Terfenol-D, are often manufactured as rods with residual magnetic fields nearly perpendicular to the rod axis. This is due to the fact that domains in the material with magnetic fields already aligned with the rod axis do not change in direction when an external magnetic field is applied along the rod axis. Therefore, these domains do not contribute to the magnetostriction. Accordingly, a rod which has domains aligned randomly will only produce about two fifths of the maximum possible magnetostriction. Therefore it is desirable to arrange all the domains to be aligned perpendicular to the rod axis [66].

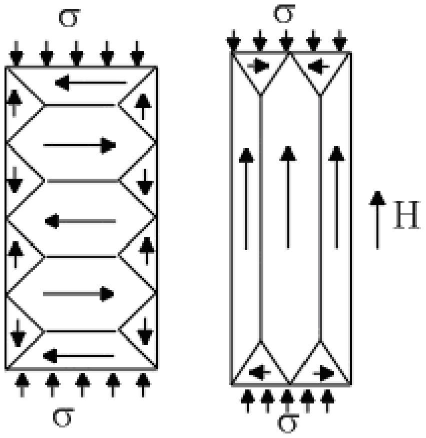

Figure 3.4: Application of compressive load to magnetostrictive materials [61].

Thus, in standard operations, magnetostrictive materials are mechanically biased. For a positive magnetostrictive material such as Terfenol-D, which generally consists of randomly oriented magnetic dipoles, a compressive load (σ) causes the orientation of these magnetic dipoles perpendicularly to the force, as shown in figure 3.4. This has the consequence of increasing the number of domains available for reorientation due to external magnetic field (H), thus maximizing stroke [72].

3.4 Fuel Injection

3.4.1 Prospect for smart materials

The fuel systems for internal combustion engines are critically important to meet the efficiency and emissions targets. A major motivation of engine research is to increase fuel efficiency and to lower the pollution to the environment. In order to improve efficiency and lower emissions, almost every step for improving control of the combustion process depends on improvements in the fuel injection system. Multiple fuel injections per combustion cycle can increase the fuel efficiency and lower the NOx and particulate emissions. However, due to the present stroke speed limitations of magnetic solenoid valves, multiple injections require the development of high-speed actuators. Also, precision manufacturing processes are influential in developing improved fuel injection systems. Focusing on the environmental concerns, in order to minimize particulate emissions, the electronic fuel injectors could operate at high pressures, such as about 20,000 psi [73]. To meet the emerging emissions regulations, the fuel injection pressure is also likely to increase to as much as 35,000 psi. This high-pressure fuel injection results in problems with wear and abrasion of fuel injector plungers and erosion, wear, and fatigue of fuel injector nozzles. In addition, low-sulfur fuels typically do not lubricate the fuel injector components. Moreover, the individual components must fit together with clearances sometimes smaller than 1×10^{-6} meters. Besides, control of the combustion process requires precise control of the size, shape, and surface finish of the injector components. In addition to new and improved materials, improved manufacturing and inspection methods for the injector components are needed as well. Although a single fuel injection event occurs in a brief fraction of a second, greater control of the rate and timing of the injection event is necessary to improve the control of combustion and resulting efficiency and emissions [73]. Pilot injection, for example, has shown to reduce NOx by spreading out the combustion event over time which reduces the maximum combustion temperature. Further reductions in NOx might be accomplished by spreading out the injection into several events, all of which must occur within a very brief time. The current systems for reliably controlling multiple injections are limited by the ability of mechanical and electronic systems to respond precisely and quickly enough to provide the additional control of injection.

In this context, smart materials, such as piezoelectric and magnetostrictive materials, offer the potential of better control of fuel injection. Due to lower materials costs and performance, some of the candidate devices for these actuators are lead zirconium titanate (PZT) [74]. Although multilayered PZT materials have been studied and are favored for their low power consumption and high precision control, a number of improvements and manufacturing methods for the materials are yet to be explored. As a result, the current research at Oak Ridge National Laboratory (ORNL) is directed towards developing a low cost multi-layer PZT actuator to be used in fuel injectors [74]. Besides, several innovations regarding the fuel injector actuator are currently under exploration with Terfenol-D as preferred actuator materials.

3.4.2 Comparative discussion between conventional solenoid injection and injection actuated by smart materials

Conventional method of actuating a fuel injector was by using an electromagnetic solenoid arrangement, which was an insulated conducting wire wound to form a tight helical coil within which a magnetic field was generated in a direction parallel to the axis of the coil when current passed through the wire. When the coil was energized, the resulting magnetic field exerted a force on a moveable ferromagnetic armature located within the coil, in that way causing the armature to move a needle valve into an open position in opposition to a force generated by a return spring. The force exerted on the armature was proportional to the strength of the magnetic field while the strength of the magnetic field depended on the number of turns of the coil and the amount of current passing through the coil [75].

In the conventional fuel injector, as shown in figure 3.5, the point at which the armature started to move varied primarily with factors such as the spring preload holding the injector closed, the friction and inertia of the needle, fuel pressure, eddy currents in the magnetic materials, and the magnetic characteristics of the design. The armature generally would not move until the magnetic force progresses to a level high enough to overcome the opposing forces. Similarly, the needle would not return to a closed position until the magnetic force decays to a low enough level for the closing spring to overcome the fuel flow pressure and needle inertia. In a conventional injector design, once the needle started actuating, it might continue to accelerate until it collided with its respective end-stops. This would eventually result in wear in the needle valve seat, needle bounce, and unwanted vibrations and noise problems. Therefore, an improved fuel injector actuation method was a requirement that would provide reduced noise, longer seat life, elimination of bounce and full actuator force applied during the entire armature stroke [75].

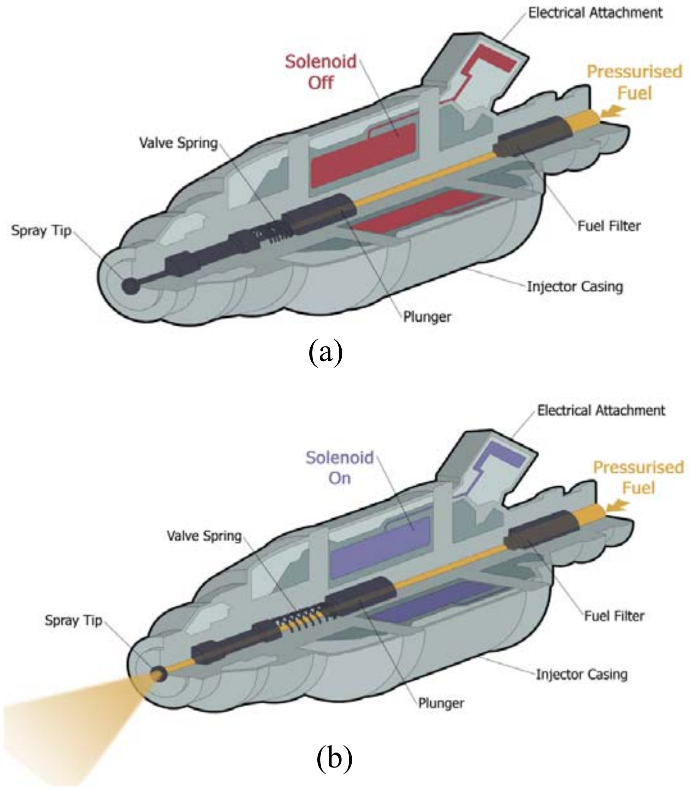

(a)

(b)

Figure 3.5: Traditional fuel injector; (a) solenoid off, valve closed position; (b) solenoid on, plunger movement and valve open position [76].

Again, a piezoelectric actuator consisting of a stack of piezoceramic or piezocrystal wafers bonded together to form a piezostack transducer, can convert energy in an electric field into a mechanical strain in the piezoelectric material. The piezostack might be attached to the mechanical member or needle performing a similar function as the needle in the conventional injector. When the piezostack has a high voltage potential applied across the wafers, the piezoelectric effect causes the stack to change dimension, thereby opening the fuel injector. However, piezoelectric transduction requires high voltages to generate a useful electric energy density and hence a useful strain in the piezoelectric material [75]. Thus, the necessity still existed for a fuel injector capable of operating on the magnetic equivalent of the piezoelectric effect.

In this context, magnetostriction could play a significant role. To illustrate the basic control operation of magnetostrictive transducers, we might consider the configuration as shown in figure 3.6. The primary components of the actuator generally consist of a cylindrical magnetostrictive rod, a wound wire solenoid, an enclosing permanent magnet and a prestress mechanism. The rod is usually constructed so that magnetic moments were primarily oriented perpendicular to the longitudinal rod axis. The number of perpendicular moments and compression in the rod could be further increased by the prestress mechanism. The application of current to the solenoid then would produce a magnetic field which would cause the moments to rotate so as to align with the field. The resulting strains and forces provide the actuator with the capabilities for transduction. The capability for attaining bidirectional strains and forces is usually provided by a magnetic bias generated by either the surrounding permanent magnet or an applied DC current to the solenoid [77].

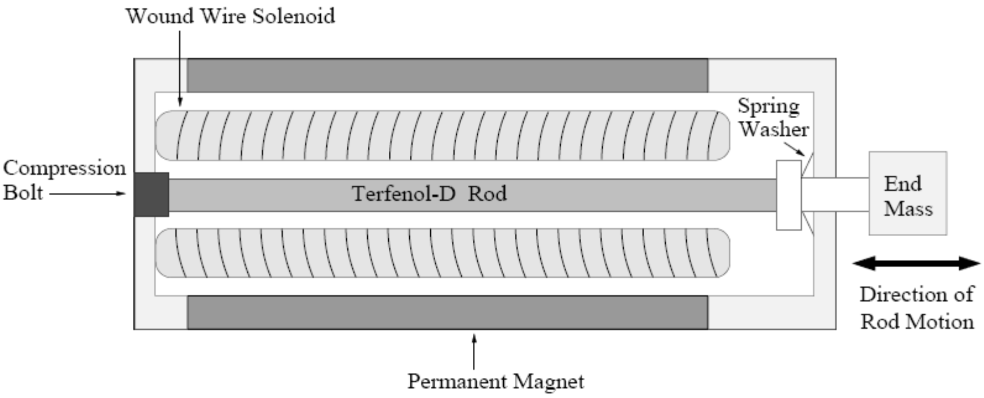

Figure 3.6: Cross section of a prototypical Terfenol-D magnetostrictive transducer [77].

It is thus apparent, that the exploitation of such exquisite characteristics of magnetostrictive materials, such as Terfenol-D, would unfold more design opportunities for many precision control applications including fuel injector design.

3.5 Magnetostrictive Material Terfenol-D

3.5.1 Terfenol-D properties

The alloy formulation of Terfenol-D is composed of, “Ter” from Terbium, “Fe” for iron, “NOL” as Naval Ordnance Laboratory and “D” from Dysprosium. Although magnetostriction only occurs in a material at temperatures below the Curie temperature, often the Curie temperature is below the temperature of the surroundings which eventually causes the magnetostriction effect to have little practical value [78]. In this context, in comparison with other magnetostrictive materials, Terfenol-D ($Tb_{0.3}D_{0.7}Fe_{1.9}$) possesses high strain, high Curie temperature, high reliability or unlimited cycle life, high force, attractive controllability with high power density and microsecond response time. Moreover, the elongation of the Terfenol-D shaft is proportional to the applied magnetic field and the magnetostriction is a reversible feature as without the magnetic field the shape of the magnetostrictive material reverts to its original shape. All of these unique utilitarian features make this material a potentially appropriate and enhanced alternative for automotive fuel injection actuation compared with the traditional solenoid fuel injection system. Terfenol-D was discovered by a research group led by A.E. Clark in the 1970's at the Naval Ordnance Laboratory. Terfenol-D is capable of providing a positive magneto-strain of typical range of 800-2000 ppm at 50-200 kA/m in bulk materials [79] and about 4000 ppm [80,101] at mechanical resonance frequencies and at high magnetic fields. Terfenol-D properties are summarized in table 3.1.

Table 3.1: Terfenol-D properties [71,79,81-88,101]

Terfenol-D properties		**Value range**
1. Nominal composition		$Tb_xD_{1-x}Fe_y$ [$0.27<x<0.3$, $1.9<y<2$]
2. Mechanical properties	Compressive strength	305-880 MPa
	Tensile strength	28-40 MPa
	Young's modulus E_H	10-75 GPa
	Young's modulus E_B	30-80 GPa
3. Thermal properties	Co-efficient of thermal expansion	12 ppm/°C
	Specific heat coefficient	0.35 kJ/kgK @25°C
	Thermal conductivity	13.5 W/mK @25°C
4. Electrical properties	Resistivity	(58-63)10-8 Ωm
	Curie Temperature	380 ºC
5. Magnetomechanical properties	Relative permeability μ_T/μ_0	9.0-12.0
	Relative permeability μ_S/μ_0	3.0-5.0
	Magnetic saturation occurs at	1.0 T
	MS coupling coefficient k_{33}	0.6-0.85
	MS strain coefficient d_{33}	8-20 nm/A
	MS quality factor Q_H	3.0-20.0

In general Terfenol-D rod applications, *parts per million* (ppm) values are expressed as the length change multiplied by a million divided by the length of the sample rod. Figure 3.7 shows the total range of length change for a given length of Terfenol-D rod.

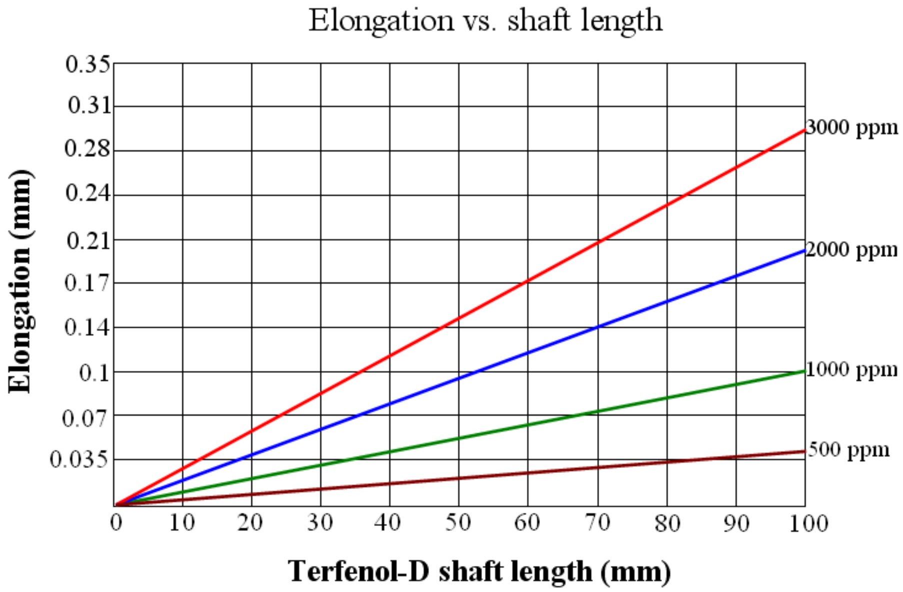

Figure 3.7: Length change versus Terfenol-D rod with strain as parameter [71].

3.5.2 *Young's modulus of Terfenol-D*

Young's modulus is among some features of Terfenol-D which are inconstant during an operation cycle varying almost linearly with the magnetic field [71]. The ΔE-Effect is showed in figure 3.8.

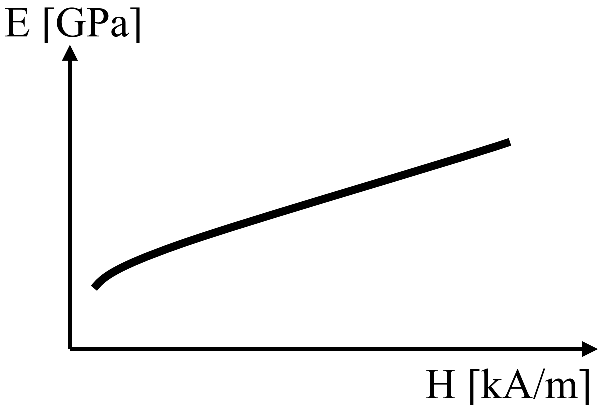

Figure 3.8: Young's modulus versus magnetic field.

At constant magnetic flux density, E_B, Young's modulus can be expressed as:

$$E_B = \frac{E_H}{(1-k_{33})} \tag{3-4}$$

According to Eq.(3-4), theoretically, for a value of flux density, Young's modulus becomes infinite. When this phenomenon occurs in a Terfenol-D sample, it is said to have reached "a blocked state". Consequently, no rotation of magnetic domains is possible and the material is prevented from changing its dimensions in response to stress [89].

3.5.3 The magnetomechanical coupling factor and the magnetostrictive coefficient

During transducer application, where the magnetic energy is converted into mechanical energy, the factor that regulates the efficiency of the energy conversion process is referred as magnetomechanical coupling factor, k_{33}. In applications where only the longitudinal elongation is of interest, the material properties related to the longitudinal axis are relevant. This mode is called *33-mode* [71]. The value of this factor usually varies between 0.5-0.8, indicating that the efficiency variation would be 50%-80% [90-92,101]. The magnetomechanical coupling factor, k_{33}, is expressed by Eq.(3-5).

$$k_{33}^2 = \frac{d_{33}^2}{\mu_{33}^T} \cdot E^H \tag{3-5}$$

In Eq.(3-5), the magnetostrictive coefficient d_{33} is the slope of the strain versus magnetic field (λ-H) curve represented in figure 3.9 and Eq.(3-6).

$$d_{33} = \frac{(d\lambda_{33})}{(dH_{33})} \tag{3-6}$$

According to figure 3.9, there is a region in the graph where the slope is high and the relationship between the strain and the magnetic field is almost linear. Therefore, this could be the optimal working range for converting the magnetic energy into mechanical energy.

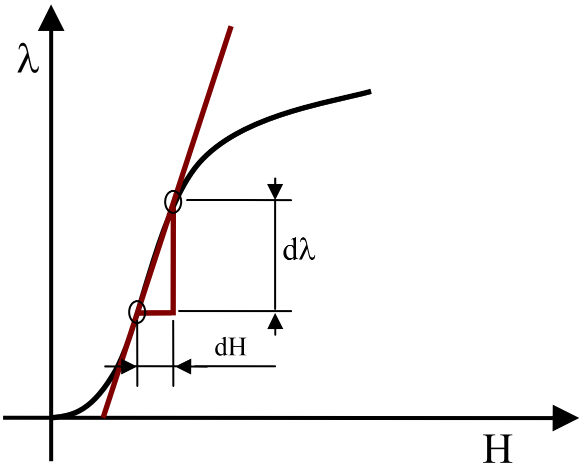

Figure 3.9: Strain versus magnetic field.

In practical applications, both magnetomechanical coupling factor k_{33} and magnetostrictive coefficient d_{33} are inconstant throughout the operating condition. These coefficients vary significantly according to both pre-stress and applied magnetic field. For Terfenol-D application, the influence of applied pressure on both k_{33} and d_{33} is depicted in figure 3.10 [90]. For effective and efficient operation, both coefficients need to be as high as possible.

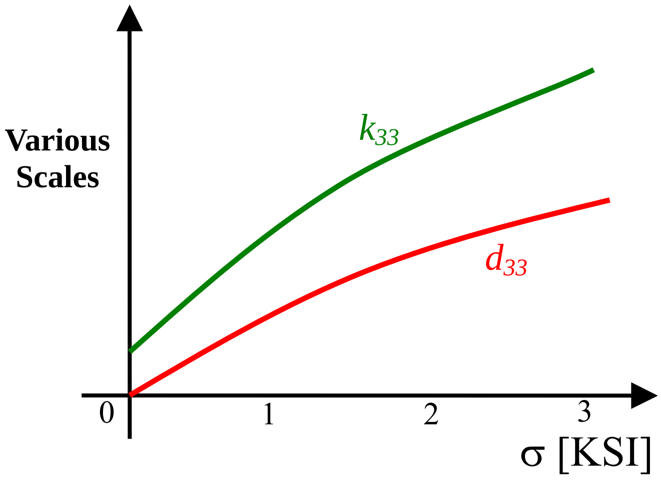

Figure 3.10: k_{33} and d_{33} versus applied stress.

3.5.4 Quality factor

When operating under a sinusoidal alternating current with constant excitation, otherwise referred as quasi-static condition, with assuming zero pre-stress and linear relationship between the strain and applied magnetic field, the strain can be expressed as in Eq.(3-7):

$$\lambda_{33} = d_{33} \cdot H_{33} \tag{3-7}$$

For most frequencies, magnetostrictive co-efficient d_{33} stays almost constant. However, when the frequency approaches towards the resonance value of the sample in its longitudinal direction, the amplitude of the vibration increases abruptly [78]. The strain caused at this resonance state is much higher compared to when it is under quasi-static condition. The strain caused under the resonance condition can be expressed as in Eq.(3-8):

$$\lambda_{33} = Q_m \cdot d_{33} \cdot H_{33} \tag{3-8}$$

In Eq.(3-8), the amplification factor of the strain at its first resonance over the strain under quasi-static conditions is the quality factor Q_m. In the case where the actuator’s vibrating end is totally free, the quality factor Q_m is due to mechanical losses occurring internally in the material [93,101] and is equal to Q_H. This internal material quality factor Q_H is in the range of 3-20 [93,101]. On the other hand, when there is a load, when the sample of Terfenol-D encounters a resistance to its free movement because of the surrounding assembly, a damping feature is introduced into the vibration and the quality factor Q_H is reduced to a value Q_m [71].

3.5.5 Permeability of Terfenol-D

In a vacuum, magnetic flux density B represents the magnitude of the internal field strength within a substance that is subjected to an H field [94] and is given by:

$$B = \mu_0 H \tag{3-9}$$

Where, μ_0 is the permeability of a vacuum = $4\pi \times 10^{-7}$ (NA^{-2}). If there is a material, other than vacuum, in the middle of the magnetic fields, the magnetic flux density now is [95]:

$$B = \mu H \tag{3-10}$$

Relative permeability, μ_r, (unitless) is used to measure the degree to which the material can be magnetized, where:

$$\mu_r = \frac{\mu}{\mu_0} \tag{3-11}$$

The relative permeability actually indicates the amplification of magnetic effects in magnetic materials. Although most ferromagnetic materials have got higher permeability, the relative permeability of Terfenol-D is much smaller compared to them. Table 3.2 represents a range of relative permeability values for different ferromagnetic materials with respect to Terfenol-D. For a material like Terfenol-D, the relative permeability depends on the prestress and the frequency used in its operation.

Table 3.2: Relative permeability of different ferromagnetic materials [96].

Materials	**Relative Permeability**	
Magnetic Iron	200	at magnetic flux density of 0.002 W/m^2
Permalloy (78.5% Nickel, 21.5% Iron)	8,000	
Mumetal (75% Nickel, 2% Chromium, 5% Copper, 18% Iron)	20,000	
Nickel	100	
Terfenol-D	<10	

Another way to specify the magnetic behavior is to use the term magnetic susceptibility; χ_m. Magnetic susceptibility is the degree of magnetization of a material in response to an applied magnetic field. Both relative permeability and magnetic susceptibility are related as follows:

$$\mu_r = 1 + \chi_m \tag{3-12}$$

Also for materials like Terfenol-D, another property connected with permeability can be defined. The permeability at constant strain is defined by:

$$\mu_{33}^{S} = \mu_{33}^{T} \cdot \left(1 - k_{33}^{2}\right) \tag{3-13}$$

This property applies to smart materials like Terfenol-D and is useful when it is in the “blocked” state. In the blocked state the material is prevented from increasing its strain by external forces and so no further rotations of magnetic domains are possible [89].

3.5.6 Hysteresis loop of Terfenol-D

A hysteresis loop contains information on magnetic properties of a material and can be represented by the relationship between magnetic flux density (*B*) and magnetic field intensity (*H*) and is normally called the *B-H* curve [94]. A material with a wide hysteresis loop has low permeability and high remanence, coercivity, reluctance and residual magnetism. On the contrary, a material with a narrower loop has the opposite characteristics. For a smart material sensor and actuator, the aim is to develop materials with the smallest hysteresis. On the other hand, a material to be used for magnetic memory with a high capacity, a large hysteresis is required, which is also the case in most permanent magnet applications figure 3.11 represents a sample hysteresis loop of a ferromagnetic material.

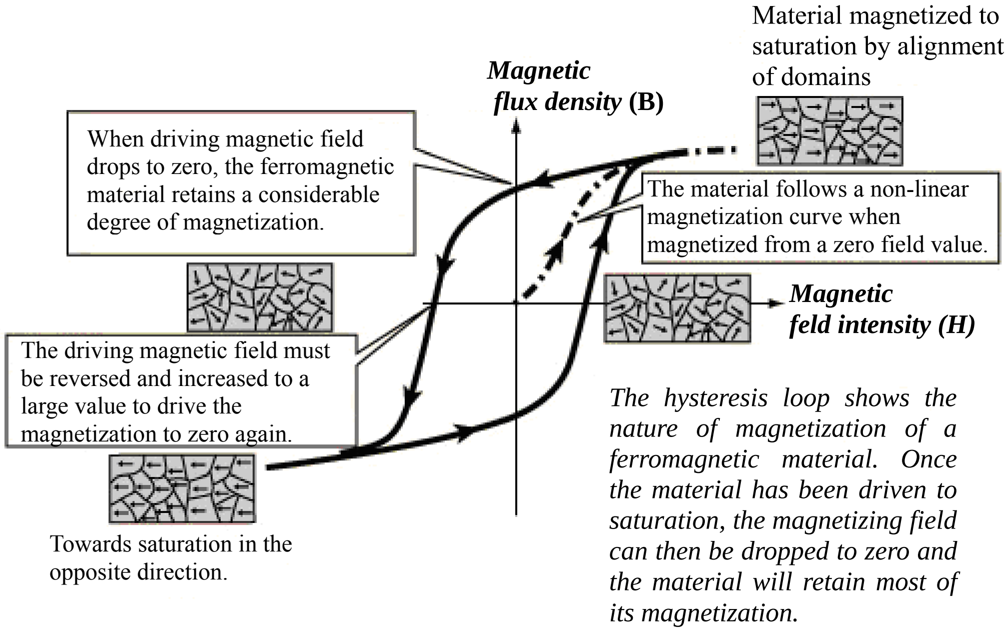

Figure 3.11: Hysteretic magnetization curve for ferromagnetic material [97].

Figure 3.12 represents the magnetic behavior of Terfenol-D, which shows the material response to an applied magnetic field (H) against magnetic flux density (B). It was found that for higher amounts of pre-stress, the relative permeability was reduced. This could be due to the fact that for positive magnetostrictive materials when the prestress is high, the domain movement requires more mechanical energy and therefore the material was unable to respond to the magnetic field as it could when the pre-stress was lower [71].

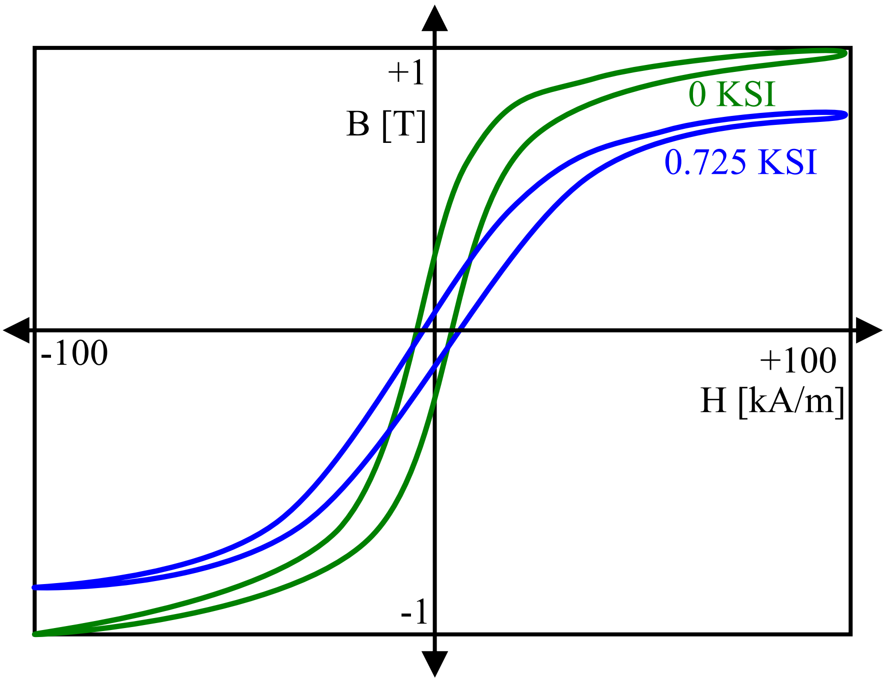

Figure 3.12: General B-H curve of Terfenol-D.

Furthermore, a typical hysteresis loop for a Terfenol-D sample, showing magnetostrictive strain in response to the magnetic field is shown in figure 3.13.

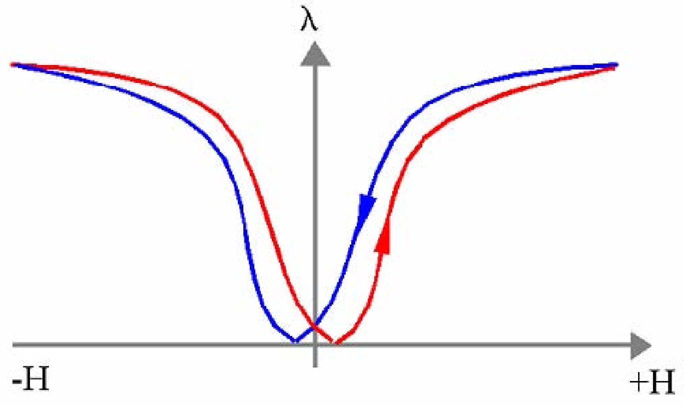

Figure 3.13: Full loop of magnetization [98].

In addition to the ferromagnetic effect or magnetic flux amplification, this change in strain is yet another response to the applied magnetic field. Although these two effects are related, their correlation is complicated. However, several hysteresis models have already been introduced regarding this purpose [99,100].

3.5.7 Blocked force of Terfenol-D

During magnetostrictive strain, the maximal achievable force is called the *blocked force*. A simple force-displacement relationship is valid for elastic behavior:

$$F_T = S_m \cdot \Delta L \tag{3-14}$$

In this equation S_m is the stiffness of the active element and is defined by:

$$S_m = \frac{E^H \cdot A}{L} \tag{3-15}$$

In this equation, E^H is the Young's modulus (at constant magnetic field), A is the cross sectional area and L is the length of the Terfenol-D element. Combining Eq.(3-12) and (3-13), substituting stiffness and magnetostrictive strain ($\lambda = \Delta L/L$) leads to equation of definition for a blocked force:

$$F_B^H = A \cdot E^H \cdot \lambda_{\max}^H \tag{3-16}$$

There is an axial force which refers to the maximum amount of magnetostrictive strain that can be applied to a sample of Terfenol-D. This occurs at very high magnetic field strengths (at $\lambda_{\max}$). According to this relationship the blocked force is proportional to the Young's modulus and the maximal strain at an applied magnetic field. [71,90].

3.6 Measurements of magnetostriction

Broadly, magnetostriction measurement techniques can be classified as either *Direct* or *Indirect*, depending on whether the strain is measured directly or the magnetostriction is derived from a measurement of some other property dependent upon strain. While direct methods enable the magnetostrictive strain to be measured as a function of the applied field, indirect methods are suitable only for measuring the saturation magnetostriction λ_{sat} [66]. Some of the most common direct measurement techniques include the *Strain Gauge* method, *Dilatometry* method and *Optical Interferometry*. In Dilatometry methods, the tunnelling tip dilatometer and Capacitance dilatometrys are mentionable. In addition, in case of indirect measurements, ferromagnetic resonance (FMR), small-angle-magnetization rotation (SAMR) and strain modulated ferromagnetic resonance (SMFMR) are some of the techniques to measure magnetostriction [66].

3.7 Production of smart materials

The raw materials of Terfenol-D are highly reactive and contain impurities. Thus, there is no straightforward way to produce it. However, at least four different methods have been developed for these purposes which are basically utilized on a near-production basis [71,101,102]. The methods are *Free Stand Zone Melting (FSZM)*, *Modified Bridgmann (MB)*, *Sintered Powder Compact* and *Polymer Matrix Composites* of Terfenol-D Powder Techniques [71,102]. Among these methods, the most common are MB and FSZM. In the FSZM-method, material in the melting zone is held in suspension by surface stress which is also known as *Directional Solidification Method*. In the MB-method, the material is melted completely and crystals are grown starting with a seed crystal [71,101]. Both methods are used to produce Terfenol-D rods with high magnetostriction and high energy density. On the other hand, the *sintered* and *composite* processes are used for the production of Terfenol-D rods for high frequency, such as higher than 1 kHz. Sinter technology methods are also suitable for forming complex geometries. In addition, new and optimized processing methods, like directional solidification or powder metallurgy methods possess good potential for high volume and cost-effective production [71,102].

In case of piezoelectric actuators, piezoceramic properties such as stiffness, capacitance, displacement, temperature stability, leakage current and lifetime are optimally combined. Recently, actuator design and electrode structure were enhanced by the latest advances in piezoelectric multilayer technology focusing on actuator design with buried electrodes (cofired encapsulation) [103,104]. In addition, *viscous plastic processing (VPP)* is another manufacturing method to produce lead zirconate titanate (PZT) fibres. PZT fibres produced by this method (VPP PZT) display high piezoelectric coefficients compared with other available PZT fibres [105].

3.8 Piezoelectric non-linearity

At low to moderate drive levels, the piezoelectric effects were relatively linear where linear models and control laws proved to be successful. But when operated under high power conditions, such as fast control of fuel injector, some non-linear behaviors and exhibition of significant hysteresis of piezoelectric materials were evident, which ought to be quantified before the materials could be employed to their full capacity. In dynamics applications, the materials also exhibited AC losses and resonance effects due to inherent magneto-mechanical coupling within the material [77]. Currently, limited understanding of the non-linear behavior of materials produced under these conditions is hindering commercialization [106].

To harness more of the piezoelectric material’s intrinsic properties, The UK's National Measurement Laboratory [106] would investigate on methods that could more accurately assess material performance in evermore demanding operating conditions. This project would specifically focus on the evaluation and prediction of heat generation and energy conversion efficiency, with the aim of enabling more cost effective materials selection. It was imagined that the project will provide a basis for a consistent approach to actuator selection and thus facilitate faster product development, cost effective testing for quality inspection and faster assessment of both new materials and product designs. It would also, in collaboration with industry, conduct a comparison of the energy efficiency of electrical to mechanical conversion of piezoelectric, magnetostrictive and solenoid systems. Again it would also investigate various new energy recovery techniques proposed for piezoelectric actuators by building and testing relevant driving circuits. They proposed that the inherent non-linearity and loss observed at high power and high frequency would be explored using three methods, a) *constant current in drive*; b) *constant voltage resonant drive* and c) *transient/burst mode drive*. These methods would then be compared on a range of materials which would enable the industries to select the method most suited to their requirements, materials and applications.

3.9 Real-time control of magnetostrictive actuators

It was apparent that the control of the magnetostrictive actuators was significant in case of fuel injection at different load conditions. The design of the control system required accurate modeling of either the static magneto-elastic constitutive relationship or rate-dependent behavior. Also when dynamic effects were not negligible, compensation of rate independent or hysteresis phenomena played a key role when real-time control tasks were of concern. Particularly, in the case of fuel injection, these types of control applications were of enormous significance due to the necessity of precise control of fuel valve. Thus finding out new and improved models for an advanced real-time control of these actuators were essential.

D. Davino and others [107] implied that giant magnetostrictive materials (GMM) could be employed as active materials in smart actuators either for quasi-static and dynamic applications requiring suitable modeling for control tasks. In particular, these materials could show either dynamic or rate-dependent memory effects mixed together. They also argued that the modeling of rate independent memory effects could be quite simple and eventually several models have been proposed and applied in this regard. Among them, the classical *Preisach* model was universally the most known [108], which allowed describing rate-independent memory phenomena (hysteresis) quite satisfactorily with acceptable computational cost. On the other hand, models taking dynamic effects into account have been proposed in later years [109], which were based on the superposition of dynamic versions of hysteresis operators (ideal relay and play operators). Unfortunately, they suffered of a quite heavy computational cost. To overcome these problems in cases where computational efficiency was obligatory, simple approaches obtained by Preisach-like operators and linear dynamic models were also investigated [110]. Furthermore, when feedback control applications were concerned, irrelevant to the model of the actuator employed, the availability of efficient procedures for hysteresis and non-linearity compensation was obligatory [111].

Cavallo and others [111] implied that the compensation of hysteretic operators was not only a tricky mathematical task, but could facilitate the design of feedback control systems employing nonlinear actuators with hysteresis. The problem was originally tackled by Krasnoselskii [112]. Furthermore, according to Krejci et al. [113], a class of simplified Preisach hysteresis operators having an exact inverse were defined. Recently, these results have been slightly generalized by Visone and others [114]. The employment of inverse of simplified Preisach hysteresis operators was effective in several applications like magnetic field computation in magnetic materials [115]. Conversely, in order to guarantee better accuracy, a general version of Preisach model was necessary for control purposes [107].

According to an experiment performed by D. Davino and others [107], where the performance of the feedback system comprised a standard regulator combined with two different compensation algorithms (pseudo-compensator operator and exact inverse numerical operator), showed good performance in terms of computational efficiency. According to them, both of the compensated algorithms outperformed the compensated case and the proposed fast inverse algorithm allowed both to reduce the tracking error while speeding up the computation improving real-time performances of the feedback control system.

3.10 Recent developments

According to an invention by P.R. Czimmek [75], his preferred embodiments overcame many of the limitations of conventional electromechanical fuel injectors and piezoelectric-actuated fuel injectors by providing a magnetostrictive material that enabled precise control of fuel through the metering valve by converting magnetic energy into mechanical energy using materials with giant magnetostrictive properties. Magnetostrictive actuation is especially advantageous in high pressure direct fuel injection applications because the high force of the magnetostrictive actuator easily overcomes the fuel pressure force. Czimmek mainly suggested that the coil current should be maintained within a reasonable range that would avoid saturating the magnetostrictive material or dissipating excessive power in the coil.

A collaborative project between ORNL, Detroit Diesel Corporation and Wayne State University [116] developed a piezoelectric control valve actuator which comprises of a piezo stack, piston, plunger and a control valve as main components. Their first phase focused on characterization of the piezo stacks and fuel injection application validation via static and dynamic tests where piezo stack gave shorter response time compared to solenoid actuated systems. Electric current and preload requirements were optimized at specified voltage levels. The required control valve motion was achieved through design and development of a hydraulic amplification system. For fuel systems, they used valves with shorter strokes which did not require motion amplification. At the end, they reduced the cost of actuator by allowing the use of lower-cost silver interlayer electrodes by fabricating the PZT stacks using ORNL low-sintering-temperature PZT. They were also able to increase the strength of ORNL composition by adding a ceramic agent to it, which eventually enhanced the reliability and life time of the actuator.

Regarding the actuation of a piezo driven control valve, according to a study by Detroit Diesel Corporation [117], the actuation delay was an order of magnitude shorter and the rise time was three times faster compared to a solenoid driven one. They also summarized that piezo actuators have a different dynamic behavior implying the necessity of different control strategies.

3.11 Summary of chapter three

Present solenoid fuel injection expertise might not be sufficient enough to meet the future emission reduction legislations due to its limitations regarding actuator response time. In this context, magnetostrictive materials offer enormous prospects in terms of their exquisite rapid response time through which precise amount of fuel can be injected according to the power requirement, which being the significant prerequisite for emission reduction. Furthermore, features like accuracy, power density and dynamic performance of this smart technology are excellent characteristics for the implementation of this technology into high volume automotive applications. In addition, stable characteristics over a wide temperature range and high magnetostrictive co-efficient are evident in enhanced materials like Terfenol-D, which are excellent parameters for actuation against high back pressure. However, further research for developing new and improved actuator structures is mandatory to enhance the capability of magnetostrictive technology regarding functional superiority and cost reduction. A concise and inclusive overview of the highlighted research process of this chapter is shown in figure 3.14.

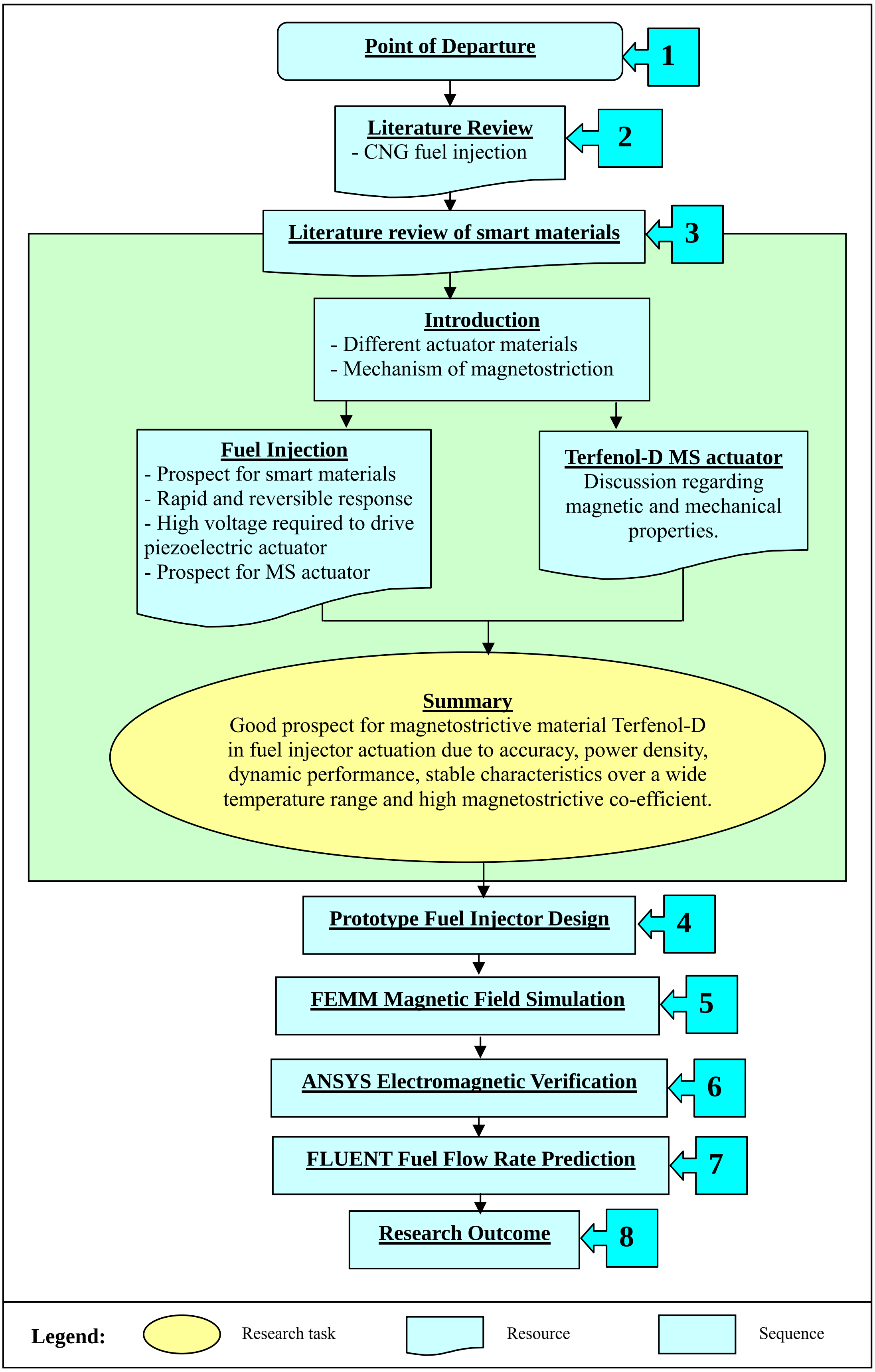

Figure 3.14: Summary of the research process in chapter three.

CHAPTER FOUR

FUEL INJECTOR DESIGN CONCEPT AND ACTUATING PARAMETER DETERMINATION

4.1 Introduction

This chapter presents a prototype CNG fuel injector design concept utilizing magnetostrictive material Terfenol-D as the fuel injector actuator. A detailed description of the mechanism of the fuel injector assembly will also be presented. Furthermore, the parameters required to actuate the injector, such as the required magnetic field strength to cause the necessary strain in the magnetostrictive material will also be determined.

4.2 Prototype CNG fuel injector

A prototype fuel injector assembly was designed using *Pro/Engineer Wildfire 3.0*, which is a 3D CAD parametric feature solid modeling software created by Parametric Technology Corporation (PTC), as shown in figure 4.1. A *Terfenol-D* shaft (30mm x 50mm) was used as the core actuator material. The injector housing was composed of *1020 Steel*, which is a low carbon steel having soft magnetic material properties. Regarding the coil material, in order to simulate the variation of the magnetic flux density and magnetizing force to achieve a desired strain output or injector lift, four different types of *American Wire Gauge (AWG)* were utilized, which is a standardized wire gauge system especially for nonferrous and electrically conducting wire. These are namely; 22 AWG, 24 AWG, 28 AWG and 30 AWG copper wires. The plunger was composed of *316 Stainless Steel* having non-magnetic properties. While a *Coil Spring* acted as the closing spring having the task of bringing the needle valve to a closed position, a *Belleville Spring* was used as the prestress spring which had the task of providing axial prestress to the Terfenol-D shaft. The fuel injector assembly and component dimensions are summarized in the appendix B.

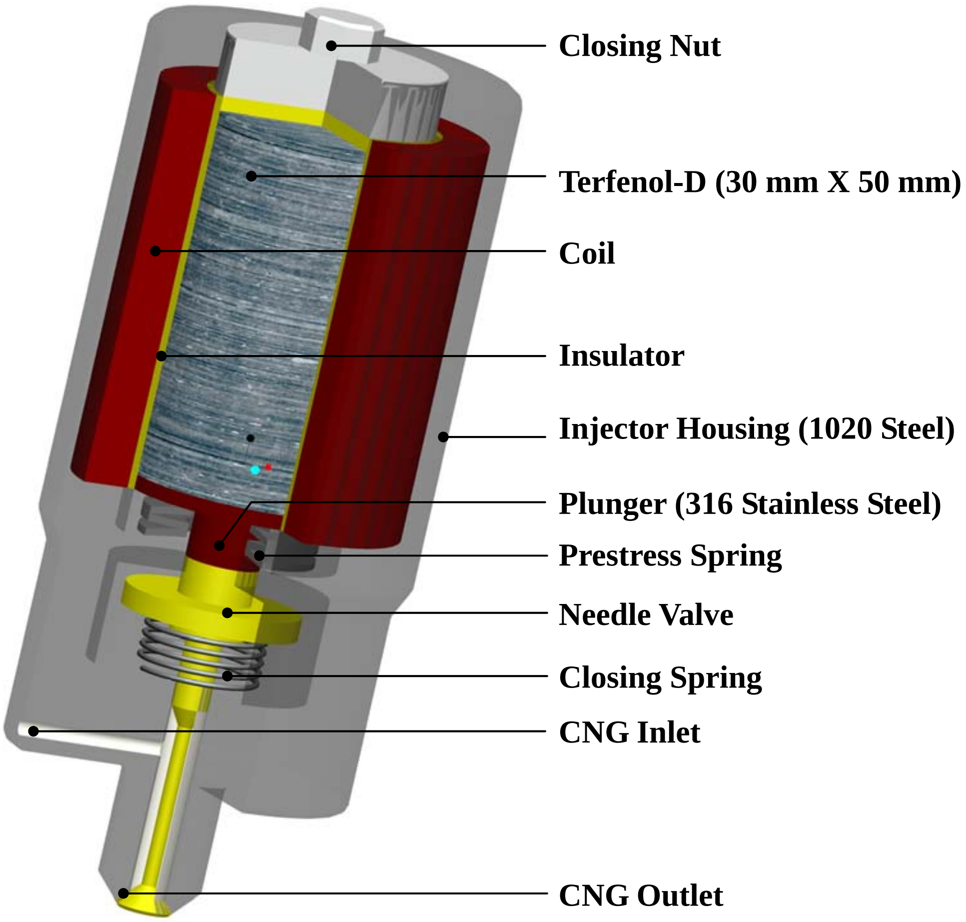

Figure 4.1: Prototype CNG fuel injector assembly.

4.2.1 Mechanism of the fuel injector

The prototype fuel injector possessed the capability to overcome many of the limitations of conventional fuel injectors through the utilization of the magnetostrictive material Terfenol-D that would enable the precise control of fuel through the metering valve by converting magnetic energy into mechanical energy. Besides acting as an injector in port fuel injection system, it also had the potential to be utilized in high pressure direct fuel injection applications because the high force of the MS actuator could easily overcome the fuel pressure. The primary design parameter required to consider in actuating the injector included selection of Terfenol-D rod which possessed the domain polarity which would be oriented to allow for a positive longitudinal magnetic field to provide maximum strains in a longitudinal direction, therefore lengthening the magnetostrictive member. Furthermore, a critical factor was selecting the prestress of the Terfenol-D rod which should not be so great as to prevent the displacement of the actuator.

The prototype fuel injector comprised an injector housing, composed of 1020 steel. The injector needle having the needle tip forming a valve in conjunction with the injector seat. The closing spring was operatively disposed to push the needle tip back into the sealing position with the injector seat. The Belleville prestress spring exerted force on the moving plunger, which was coaxially aligned with the injector needle and Terfenol-D member. Soft steel spacers might be positioned at both ends of the Terfenol-D member to cushion the movement of the member itself. The needle valve and plunger was arranged in such a way as to prevent fuel from entering the upper portion of the injector body. When the coil around the Terfenol-D member would be energized, that would generate a magnetic field around the member itself. Depending upon the magnetic field strength, the member would then elongate causing a strain. The contacting plunger would then transmit this strain in terms of displacement by pushing the needle valve in the outward direction. Consequently, as the needle valve would open, CNG from the fuel inlet, which was operatively connected to the valve body, would then pass through the needle tip openings at high pressure. Figure 4.2 depicts the needle valve with CNG inlet port.

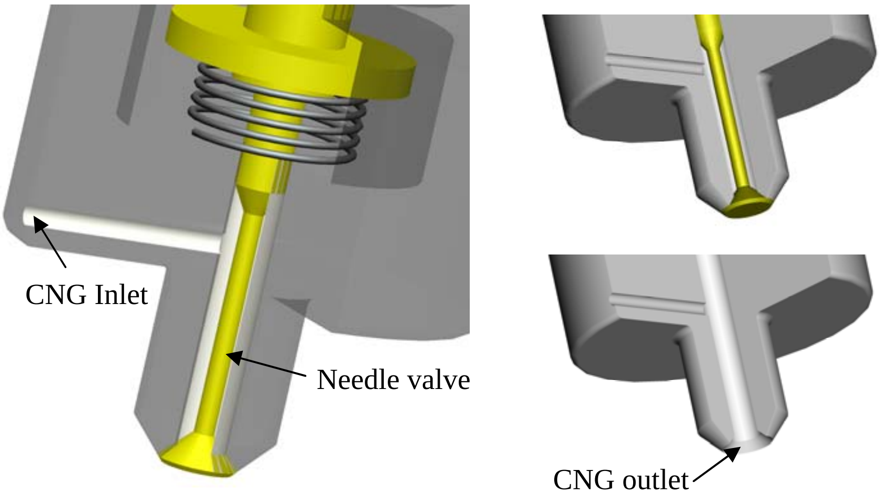

Figure 4.2: CNG inlet-outlet port and needle valve.

4.3 Fuel injector component material properties

The material properties of the injector housing and plunger were significant as these materials were utilized in the electromagnetic simulation of the fuel injector. In case of the injector housing and plunger, *1020 Steel* and *316 Stainless Steel* were utilized respectively. The detailed discussion regarding the material properties of Terfenol-D have already been discussed in section 3.5.

4.3.1 1020 Steel

1020, a commonly used plain carbon steel having soft magnetic properties, possess a nominal carbon content of 0.20% with approximately 0.50% manganese. Furthermore, it possess a good combination of strength and ductility and might be hardened or carburized. It also possesses good machinability and formability with readily weldable capability by all standard welding methods [118]. Moreover, table 4.1 shows the typical material properties and figure 4.3 describes the non-linear B-H properties of 1020 steel.

Table 4.1: Typical material properties of 1020 Steel [118,119]

Chemical properties	
Carbon (C)	0.17-0.23%
Iron (Fe)	Balance
Manganese (Mn)	0.3-0.6%
Phosphorus (P)	0.04% max
Sulphur (S)	0.05% max
Physical properties	
Density (x 1000 kg/m^3) @ 25^{o}C	7.7-8.03
Relative permeability	760
Poissons Ratio @ 25^{o}C	0.27-0.30
Thermal Expansion (10^{-6}/^{o}C) @ 20-700^{o}C annealed treatment	14.8
Elastic Modulus (GPa) @ 25^{o}C	190-210
Tensile Strength (MPa)	394.7
Yield Strength, (MPa)	294.8

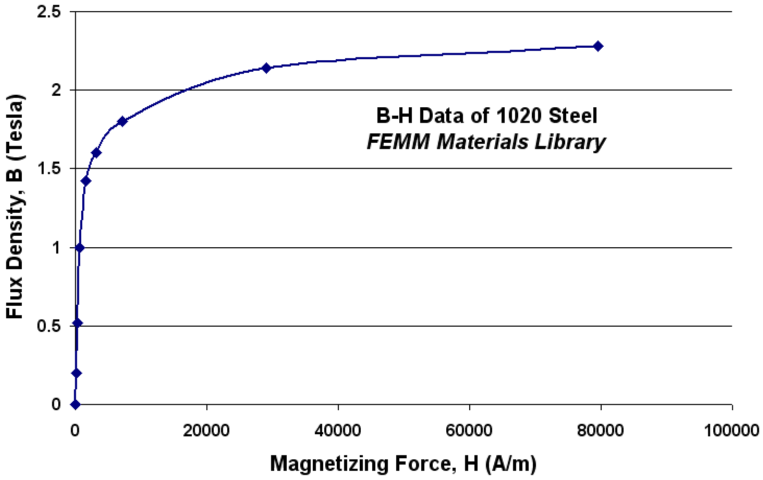

Figure 4.3: Non-linear B-H data of 1020 Steel from FEMM materials Library.

4.3.2 Grade 316 Stainless Steel

In case of the fuel injector, the plunger needed to be non-responsive to the magnetic field in order to avoid the solenoid effect in the plunger itself. Otherwise, there might be different relative motions generated between Terfenol-D and plunger resulting in less or improper injector lift. Besides, redundant impact resulting in wear might be another possibility.

Grade 316 is a standard molybdenum-bearing grade in austenitic range, thus having very low magnetic permeability showing no response to a magnet when in the annealed condition. The change in magnetic response is actually due to atomic lattice straining and martensite formation. Generally, if the nickel to chromium ratio in the material composition is higher, the austenitic structure becomes more stable showing less magnetic response. This high nickel to chromium ratio is evident in grade 316 stainless steel structure, thus imposing low magnetic response [120].

Furthermore, 316 Stainless Steel possess high corrosion resistance, more resistant to carbide precipitation, excellent weldability by all standard fusion methods and upgraded machining characteristics. The austenitic structure also gives these grades excellent toughness characteristics [120]. Table 4.2 depicts the typical material properties of the 316 Stainless Steel.

Table 4.2: Typical material properties of 316 Stainless Steel [120]

Chemical properties		
Carbon (C)	<0.03%	
Iron (Fe)	Balance	
Chromium (Cr)	16-18.5%	
Nickel (Ni)	10-14%	
Molybdenum (Mo)	2-3%	
Manganese (Mn)	<2%	
Silicon (Si)	<1%	
Phosphorus (P)	<0.045%	
Sulphur (S)	<0.03%	
Physical properties		
Density (kg/m^3)	8000	
Elastic Modulus (GPa)	193	
Thermal Conductivity (W/m.K)	@ 100^{o}C	16.3
	@500^{o}C	21.5
Specific Heat, 0-100^{o}C (J/kg.K)	500	
Electric Resistivity (nΩ.m)	740	

4.4 Actuating parameter determination

Before approaching the electromagnetic simulation, the required parameters for the desired magnetostrictive strain or injector lift had to be predetermined. For a desired injector lift of 50 microns and for a 50 mm long Terfenol-D member, the required magnetostrictive strain was around 1000 ppm. From figure 4.4, in order to achieve this amount of strain, for 1 KSI preload, the applied magnetic field needed to be around 500 Oersted (Oe), which was about 40,000 A/m of magnetizing force (H).

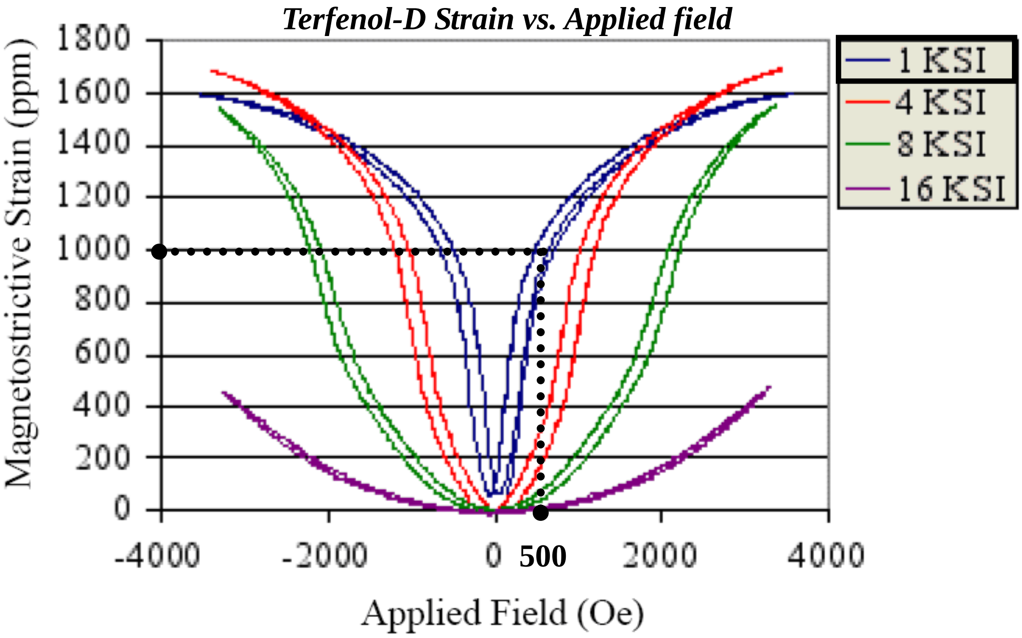

Figure 4.4: Terfenol-D strain vs. applied field at various preloads, data from ETREMA PRODUCTS INC.

Although the actual B-H curve of ferromagnetic materials could be represented as figure 4.5, in this case, the B-H curve of Terfenol-D was treated approximately as linear as the desired and operational values of the flux density and the magnetizing force were far below the saturation point. In this region, the graph could be represented as figure 4.6 where the Terfenol-D B-H data were provided by ETREMA PRODUCTS INC.

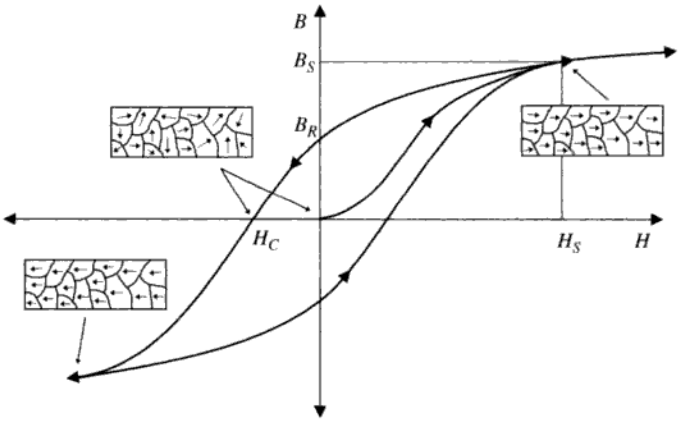

Figure 4.5: Hysteretic magnetization curve for a ferromagnetic material and relevant points: B_R, remnance; (H_S, B_S), saturation; and H_C, coercitive field strength [72].

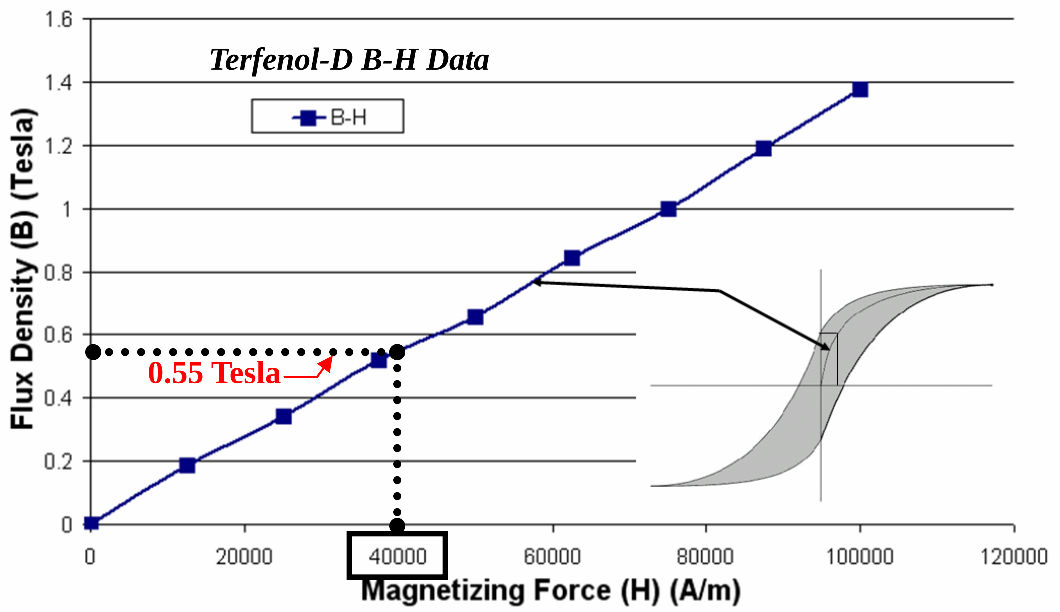

Figure 4.6: B-H data of Terfenol-D, data from ETREMA PRODUCTS INC.

Analyzing the Terfenol-D B-H data, for about 40,000 A/m of magnetizing force, the flux density (B) that was needed to be accomplished was about 0.55 Tesla, as shown in figure 4.6. Therefore, theoretically, in order to achieve 50 microns of injector lift, flux density, B = 0.55 Tesla (T) was needed to be accomplished for 1 KSI prestress, which is summarized in table 4.3.

Table 4.3: Required parameters to achieve in simulation

Terfenol-D MS shaft ***Dimension:*** *30 mm x 50 mm* ***Prestress:*** *1 KSI*	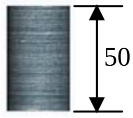 50 mm
	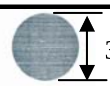 30 mm
Parameters to achieve	***Value***
Injector lift (Microns)	50
Required Flux density, B (Tesla)	0.55

4.5 Summary of chapter four

A prototype CNG fuel injector assembly was designed utilizing magnetostrictive material Terfenol-D as the actuator material. Furthermore, the associated fuel injector component material properties were highlighted. Next upcoming chapters would emphasize on generating the identical fuel injector model in the simulated environments with the corresponding material properties. In this context, the parameters required to achieve the desired magnetic field strength to cause the necessary magnetostrictive strain were predetermined in order to initiate the electromagnetic and computational fluid dynamics simulations. A concise and inclusive overview of the highlighted research process of this chapter is shown in figure 4.7.

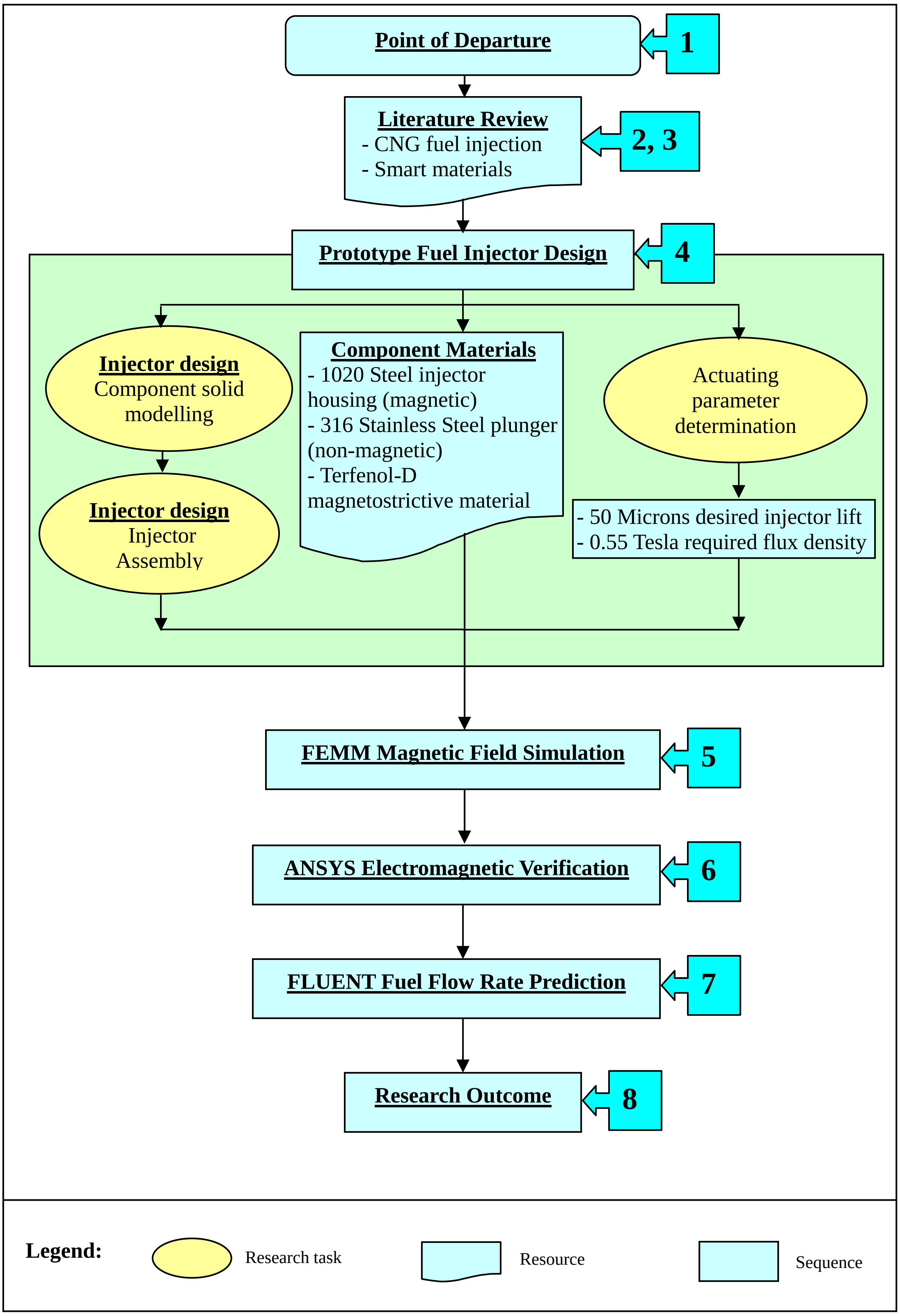

Figure 4.7: Summary of the research process in chapter four.

CHAPTER FIVE

FEMM MAGNETIC FIELD SIMULATION

5.1 Introduction

Finite Element Method Magnetics (FEMM) is a finite element software package for solving low frequency electromagnetic problems on two-dimensional planar and axisymmetric domains developed by David Meeker of Foster-Miller, Inc [121]. The package is composed of an interactive shell which is a Multiple Document Interface pre-processor and a post-processor, a triangular mesh generator and various solvers for linear or nonlinear magneto-static and time harmonic magnetic problems, linear electrostatic problems and steady-state heat flow problems. In this chapter, FEMM version 4.2 was utilized to perform the magnetics simulations.

The purpose of this chapter is to present the methodology and results of the non-linear, axisymmetric magnetics simulation to obtain the desired magnetic field strength in order to achieve the magnetostrictive strain while minimizing the power consumption of the coil circuitry.

5.2 Relevant Partial Differential Equations

5.2.1 Magnetostatic problems

In case of magnetostatic problems, the fields are time-invariant. For such cases, the field intensity ($\vec{H}$) and flux density ($\vec{B}$) must obey:

$$\vec{\nabla} \times \vec{H} = \vec{J} \tag{5-1}$$

Where, $\vec{J}$ denotes current density.

$$\vec{\nabla} \cdot \vec{B} = 0 \tag{5-2}$$

Again, the constitutive relationship between $\vec{B}$ and $\vec{H}$ for each material being:

$$\mu = \frac{\vec{B}}{\vec{H}} \tag{5-3}$$

However, for nonlinear material properties, the permeability μ is actually a function of $\vec{B}$:

$$\mu = \frac{\vec{B}}{\vec{H}(\vec{B})} \tag{5-4}$$

Now, flux density can be written in terms of vector potential, $\vec{A}$, as:

$$\vec{B} = \vec{\nabla} \times \vec{A} \tag{5-5}$$

FEMM actually searches for a field that satisfies from Eq. (5-1) to (5-3) via this magnetic vector potential approach. Now, as the definition of $\vec{B}$ always satisfies Eq. (5-2), then Eq. (5-1) can be written as:

$$\vec{\nabla} \times \left(\frac{1}{\mu\left(\vec{B}\right)} \vec{\nabla} \times \vec{A} \right) = \vec{J} \tag{5-6}$$

Again, for a linear isotropic material and also assuming the Coulomb gauge, $\vec{\nabla} \cdot \vec{A} = 0$, Eq. (5-6) reduces to:

$$-\frac{1}{\mu} \vec{\nabla}^2 \vec{A} = \vec{J} \tag{5-7}$$

In order to solve magnetostatic problems with a non-linear *B-H* relationship, FEMM utilizes Eq. (5-6) [122].

5.2.2 Time-harmonic magnetics problem

If the frequency is non-zero or the magnetic field is time varying, the program will perform a harmonic analysis, in which all field quantities are oscillating at this prescribed frequency. Denoting the electric field intensity as $\vec{E}$ and the current density as $\vec{J}$; they obey the constitutive relationship:

$$\vec{J} = \sigma \vec{E} \tag{5-8}$$

Where, σ represents electrical conductivity.

The induced electric field follows:

$$\vec{\nabla} \times \vec{E} = -\frac{\partial \vec{B}}{\partial t} \tag{5-9}$$

Substituting the vector potential form of $\vec{B}$ into Eq.(5-9) yields,

$$\vec{\nabla} \times \vec{E} = -\vec{\nabla} \times \dot{\vec{A}} \tag{5-10}$$

Now, in case of two-dimensional problems, Eq.(5-10) can be integrated to yield:

$$\vec{E} = -\dot{\vec{A}} - \vec{\nabla} V \tag{5-11}$$

Now, from Eq. (5-8),

$$\vec{J} = -\sigma \dot{\vec{A}} - \sigma \vec{\nabla} V \tag{5-12}$$

Now, substituting into Eq.(5-6) yields the partial differential equation,

$$\vec{\nabla} \times \left(\frac{1}{\mu\left(\vec{B}\right)} \vec{\nabla} \times \vec{A} \right) = -\sigma \dot{\vec{A}} + \vec{J}_{src} - \sigma \vec{\nabla} V \tag{5-13}$$

Where, $\vec{J}_{src}$ represents the applied current source and $\vec{\nabla} V$ is an additional voltage gradient which is constant over a conducting body in two-dimensional problems. FEMM considers Eq. (5-13) for the case in which the field is oscillating at one fixed frequency [122].

5.3 Model Construction and Analysis

As mentioned in the previous chapter, the FEMM magnetics simulations would be carried out for four different AWG wire types and four different coil thicknesses. The model to be analyzed is shown in figure 5.1.

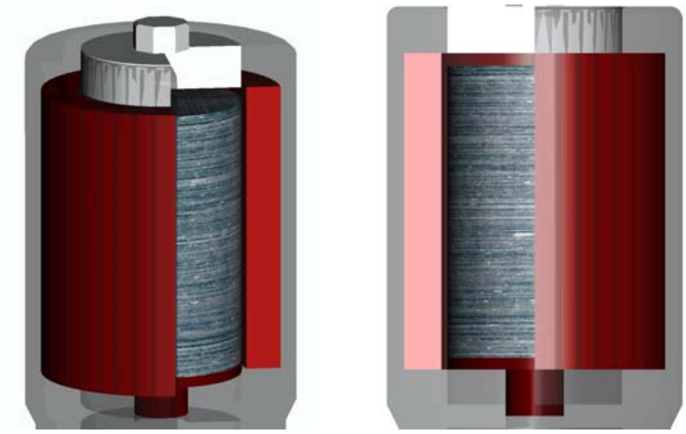

Figure 5.1: Injector components for FEMM simulation.

For a single coil thickness, the coil number of turns was varied according to the varying AWG wire type. Table 5.1 shows the four AWG wire types with the number of turns per centimetre length. For a fixed coil thickness, given the length of the coil and the AWG wire diameter, the value of the number of turns in layers could be retrieved. Therefore, for each coil thickness, there would be four different sets of coil number of turns according to their corresponding AWG wire types. Table 5.2 shows all the coil number of turns in layers used in this FEMM simulation. Then, for each AWG type, the current was varied in the coil circuitry from 0 to 5 amps to determine the variation of magnetic field strength with the consequent power output. Initially, all the calculations were performed with 0 Hz frequency, otherwise mentioned as magnetostatic problem. Then, for the optimized geometry, after analyzing the required current flow, power consumption and voltage drop which would meet the desired flux density of 0.55 Tesla, the simulations were repeated aging for harmonic magnetic problem with frequencies *10 Hz*, *20 Hz*, *50 Hz*, *100 Hz*, *250 Hz* and *500 Hz* to compare the variation of results with varying frequencies.

Table 5.1: Table of AWGs

AWG	Wire Diameter (mm)	Turns of Wire (per cm)	Copper Resistance (Ω/1 km)
22	0.6438	15.56	52.953
24	0.5106	19.59	84.219
28	0.3211	31.25	212.927
30	0.2546	39.37	338.583

Table 5.2: Coil number of turns in layers.

Coil Thickness, t mm	AWG	Number of Turns	Layers
2	22	252	3
	24	423	4
	28	1012	6
	30	1700	8
3	22	420	5
	24	635	6
	28	1518	9
	30	2551	12
4	22	504	6
	24	846	8
	28	2025	12
	30	3402	16
5	22	672	8
	24	1058	10
	28	2700	16
	30	4252	20

5.3.1 Problem definition and creating model geometry

FEMM contains a CAD like interface for laying out the geometry of the problem to be solved and for defining material properties and boundary conditions. Initially, the simulation type was set as magnetics. Then, in the *problem definition* dialog box, the *Problem Type* was set as axisymmetric, the *Length Units* was set to millimeters (mm) and the frequency was set according to the criteria, as shown in figure 5.2. The *depth* specification box only got enabled when a *Planer* problem was selected.

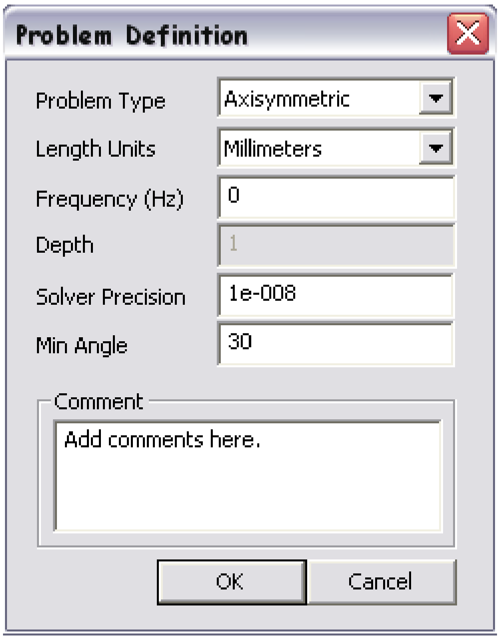

Problem Definition

Problem Type: Axisymmetric

Length Units: Millimeters

Frequency (Hz): 0

Depth: 1

Solver Precision: 1e-008

Min Angle: 30

Comment: Add comments here.

Figure 5.2: Problem definition in FEMM.

The *Solver Precision* edit box specified the stopping criteria of the linear solver where the linear algebra problem could be represented by:

$$Mx = b \tag{5-14}$$

Where, M is a square matrix, b is a vector, and x is a vector of unknowns to be determined. The solver precision value determines the maximum allowable value for $||b-Mx||/||b||$. The default value was 10^{-8} [122]. The *Min Angle* edit box was used as a constraint in the triangle meshing program ensuring that no angles smaller than the specified angle could occur [122]. In this case, the min angle was set to 30 degrees because practically it was found that the algorithm often succeeds for minimum angles up to 33.8 degrees [122].

In order to carry out the FEMM simulations, a two-dimensional cross-section of the injector geometry was built inside FEMM interface, which incorporated the injector housing, coil, Terfenol-D shaft and plunger. The corresponding regions included the real magnetic properties of corresponding materials. As the parametric prerequisite was to vary the coil thickness from 2 mm to 5 mm, four different sets of axisymmetric injector geometry representing four different coil thicknesses were modeled, as shown in figure 5.3.

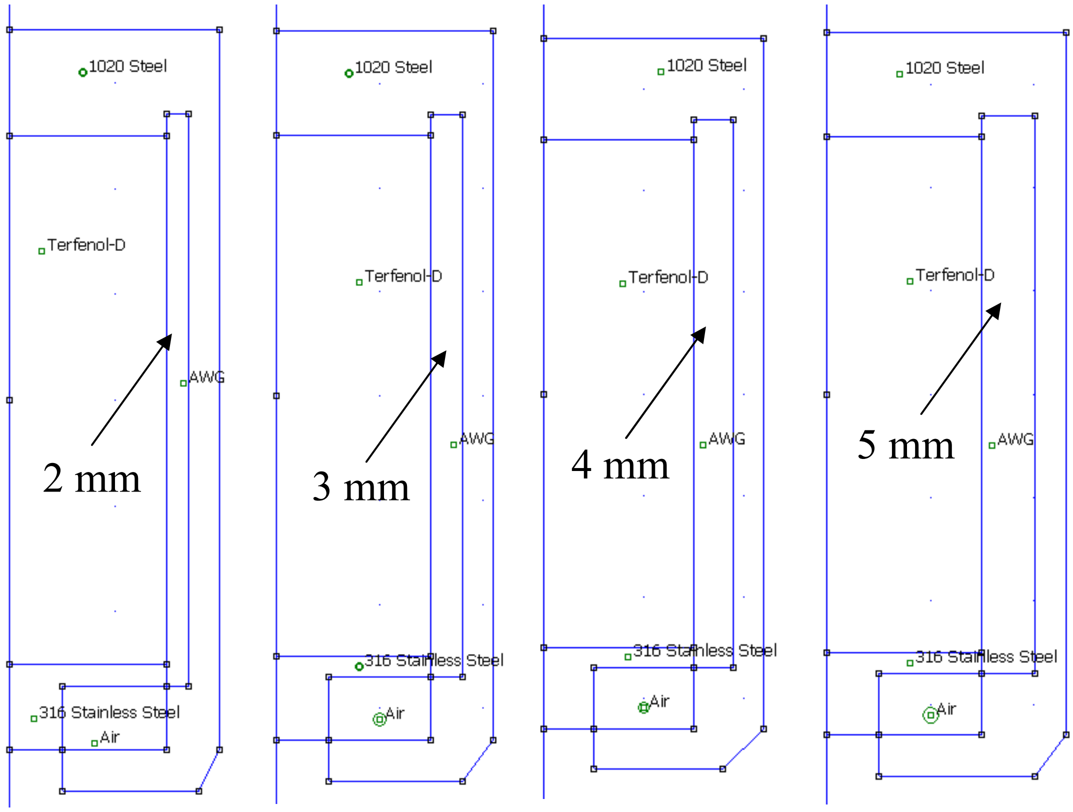

Figure 5.3: Injector geometry in FEMM with four coil thicknesses.

5.3.2 Boundary conditions

The purpose of specifying boundary condition was to assign the properties of line segments or arc segments that are to be boundaries of the solution domain. Boundary conditions for magnetic and electrostatic problems come in five varieties. These are namely, a) *Dirichlet*, where the value of potential A or V is explicitly defined on the boundary; b) *Neumann*, where the condition of normal derivative of A is specified which forces the flux to pass the boundary at exactly 90^{o} angle to the boundary; c) Robin, which is actually a sort of mix between Dirichlet and Neumann; d) *Periodic*, where two boundaries are joined together and the boundary values on corresponding points of the two boundaries are set equal to one another; and e) Antiperiodic, which also joins two boundaries together but the boundary values are made to be of equal magnitude but opposite sign [122].

For this FEMM simulation, the BC type was set as *Mixed* to create an *asymptotic boundary condition* that approximated the impedance of an unbounded, open space which enabled modeling of the field produced by the coil in an unbounded space while still only modeling a finite region of that space. *Mixed* denotes a boundary condition of the form:

$$\left(\frac{1}{\mu_r \mu_O}\right)\frac{\partial A}{\partial n} + c_O A + c_1 = 0 \tag{5-15}$$

Where, A is magnetic vector potential, μ_r is the relative magnetic permeability of the region adjacent to the boundary, μ_o is the permeability of free space and n represents the direction normal to the boundary. By carefully choosing the c_o coefficient and specifying $c_1 = 0$, this boundary condition could be applied to the outer boundary of the geometry to approximate an unbounded solution region described earlier. Thus, for the asymptotic boundary condition, the c_o and c_1 coefficients were specified as:

$$c_O = \frac{1}{\mu_r \mu_O R} \tag{5-16}$$

$$c_1 = 0 \tag{5-17}$$

Where, R was the outer radius of the spherical problem domain of 100 mm. This boundary condition was applied to the arc defining the outer boundary of the region. Furthermore, a zero potential was automatically applied along the $r = 0$ line for axisymmetric problem, as shown in figure 5.4.

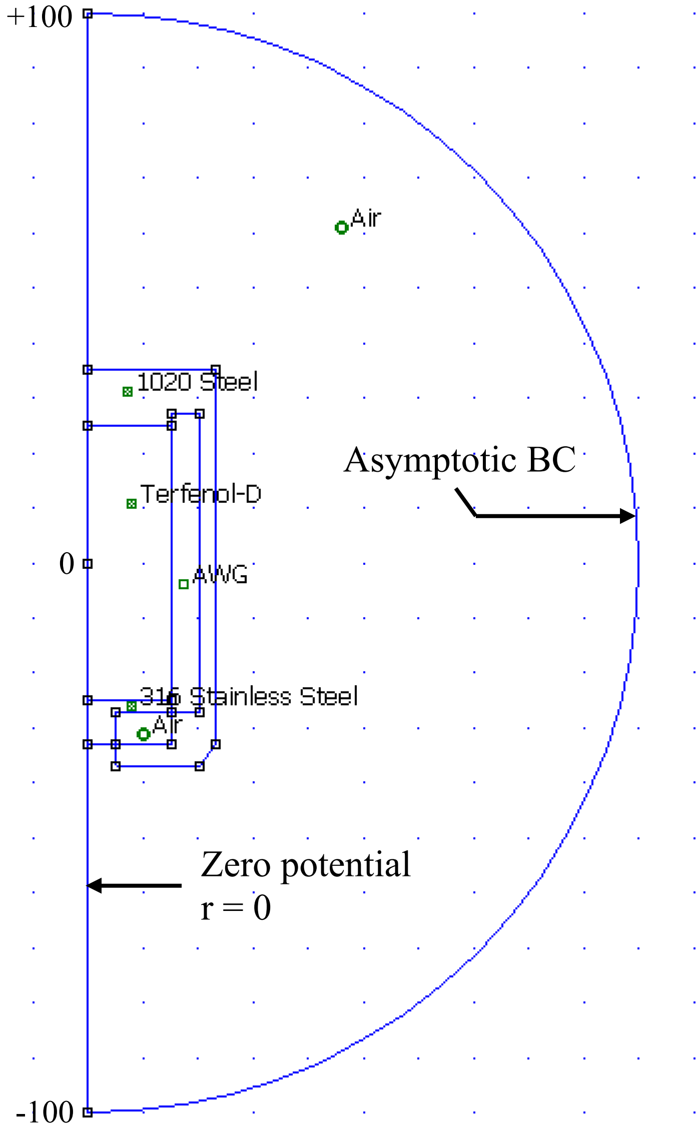

Figure 5.4: Applying boundary conditions in FEMM.

5.3.3 Material and circuit properties

FEMM provided a built-in material library which enabled the use of any available material properties according to the specification for the simulation purpose. In case of the fuel injector, the properties for *1020 steel*, *316 stainless steel*, *AWG copper wire* and *air* were selected, as shown in figure 5.5. The properties of these materials have already been depicted in chapter four.

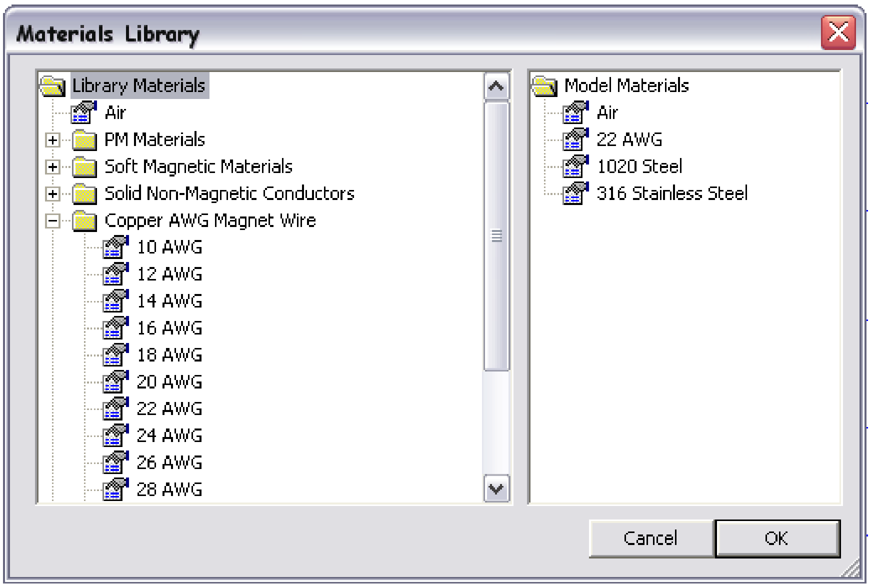

Materials Library

Library Materials
- Air
- PM Materials
- Soft Magnetic Materials
- Solid Non-Magnetic Conductors
- Copper AWG Magnet Wire
  - 10 AWG
  - 12 AWG
  - 14 AWG
  - 16 AWG
  - 18 AWG
  - 20 AWG
  - 22 AWG
  - 24 AWG
  - 26 AWG
  - 28 AWG

Model Materials
- Air
- 22 AWG
- 1020 Steel
- 316 Stainless Steel

Figure 5.5: Adding material properties to the model.

However, as the material properties of Terfenol-D was unavailable in the FEMM materials library, the Terfenol-D material model was constructed from the B-H data provided by the manufacturing company ETREMA Products, Inc., as shown in figure 5.6. The associated properties were then attached with the block labels into the FEMM interface which included the real magnetic properties of the corresponding materials.

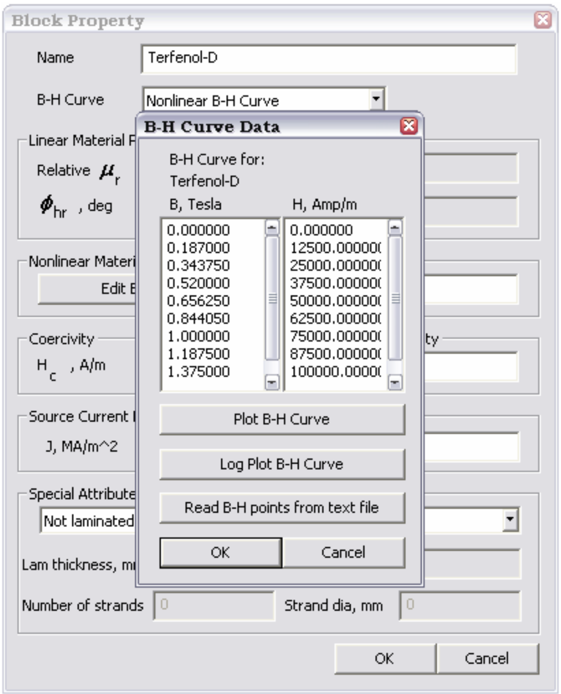

Block Property

Name: Terfenol-D

B-H Curve: Nonlinear B-H Curve

Special Attribute: Not laminated

Number of strands: 0

Strand dia, mm: 0

B-H Curve Data

B-H Curve for:
Terfenol-D

B, Tesla	H, Amp/m
0.000000	0.000000
0.187000	12500.00000
0.343750	25000.00000
0.520000	37500.00000
0.656250	50000.00000
0.844050	62500.00000
1.000000	75000.00000
1.187500	87500.00000
1.375000	100000.0000

Figure 5.6: Constructing Terfenol-D material model in FEMM.

In order to construct the circuit property, in the *circuit property dialog box*, a series circuit with circuit current (amps) was defined. For this simulation, the circuit current was varied from 0 to 5 amps. The circuit property was then assigned to the coil region in the injector model specifying the coil number of turns. A negative value of the coil number of turns would indicate that the turns are wrapped in a counter-clockwise direction.

5.3.4 Meshed geometry

The idea of finite element analysis was to discretize the problem into a large number of regions, each with a simple geometry. Specifically, FEMM discretizes the problem domain using *triangular* elements. Over each element, the solution is approximated by a linear interpolation of the values of potential at the three vertices of the triangle [122]. After assigning all the material properties and applying the boundary conditions, the two-dimensional model was eventually meshed with a coarse triangular mesh at the outside region and a finer triangular mesh at the significant regions such as Terfenol-D core, injector housing and plunger to get more accurate results, as shown in figure 5.7.

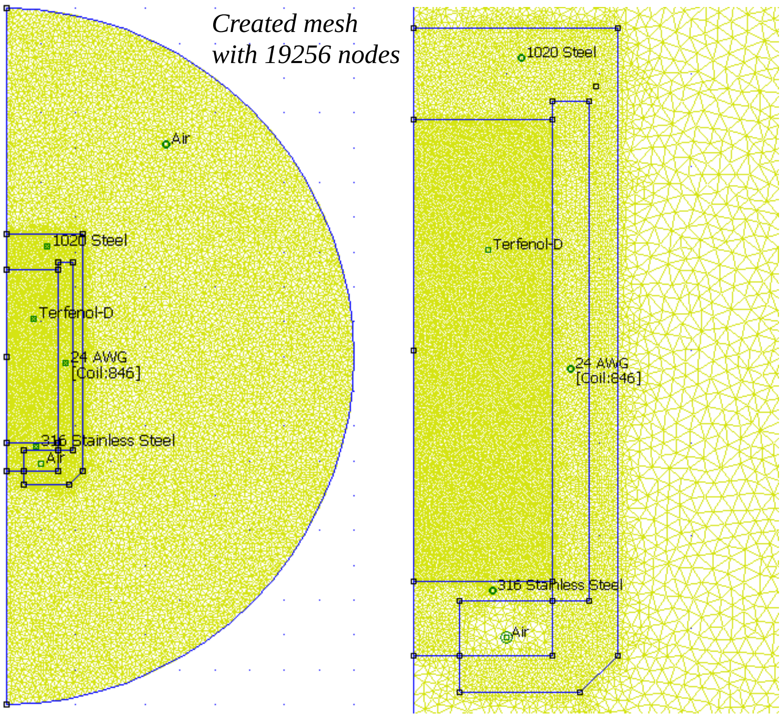

Figure 5.7: Meshed geometry in FEMM.

5.4 FEMM analysis results

5.4.1 Magnetostatic series circuitry

The purpose of the magnetic simulation was to get the desired flux density to achieve the required injector lift while minimizing the power consumption of the coil circuitry. It was found that, as the AWG number got higher, so did the power consumption of the corresponding coil, which was identical for all four coil thicknesses, as shown in figure 5.8.

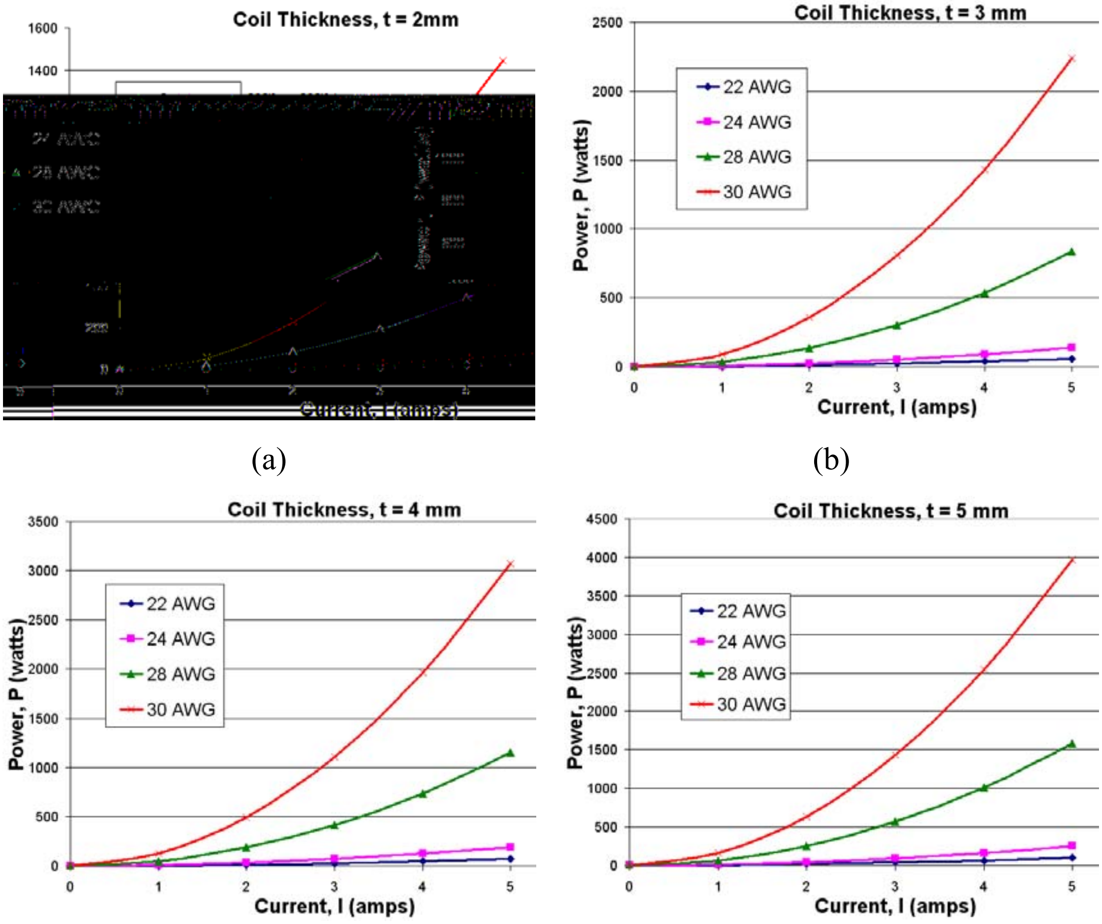

(a) (b)

(c) (d)

Figure 5.8: Power vs. current for coil thickness; (a) t = 2mm; (b) t = 3mm; (c) t = 4mm and (d) t = 5mm.

It was apparent that for any given coil thickness, the number of turns of higher AWG wires would also increase. However, as the magnetic field intensity was proportional to coil number of turns for a constant current flow, to achieve a desired flux density, the coil number of turns could not be compromised. This was critical in case of this injector model as the required injector lift could only be obtained if only the certain flux density or field intensity could be achieved, which would eventually cause the necessary amount of strain for a particular prestress (see figure 4.4). Thus, lowering the number of turns or the current flow to minimize power was not an option. Therefore, the power consumptions of high AWG wires with higher coil thicknesses got increasingly higher.

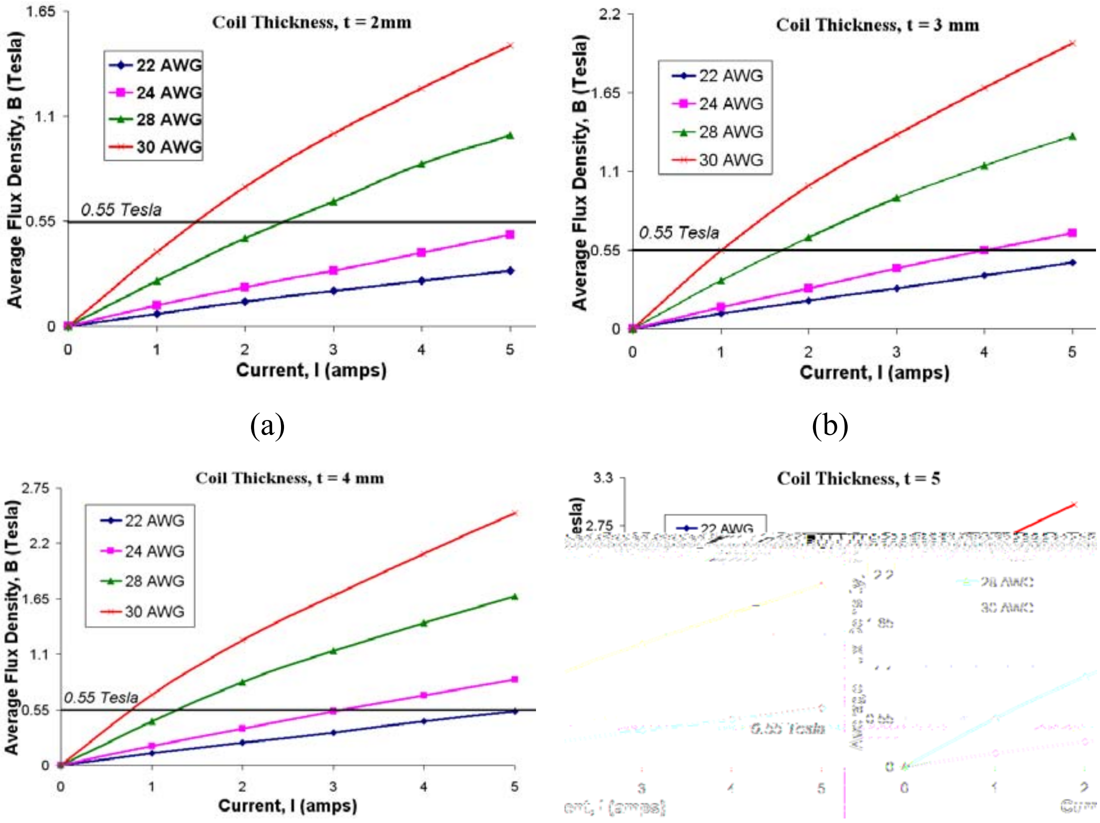

(a) (b)

(c) (d)

Figure 5.9: Average flux density vs. current for coil thickness; (a) t = 2mm; (b) t = 3mm; (c) t = 4mm and (d) t = 5mm.

Again, figure 5.9 showed the variation of flux density at varying circuit current for different AWG coil wires. The horizontal line indicated the desired flux density level. It was apparently clear that, although higher AWG coil types had low current requirement in order to reach the desired flux density, their power consumption and voltage requirement was relatively higher.

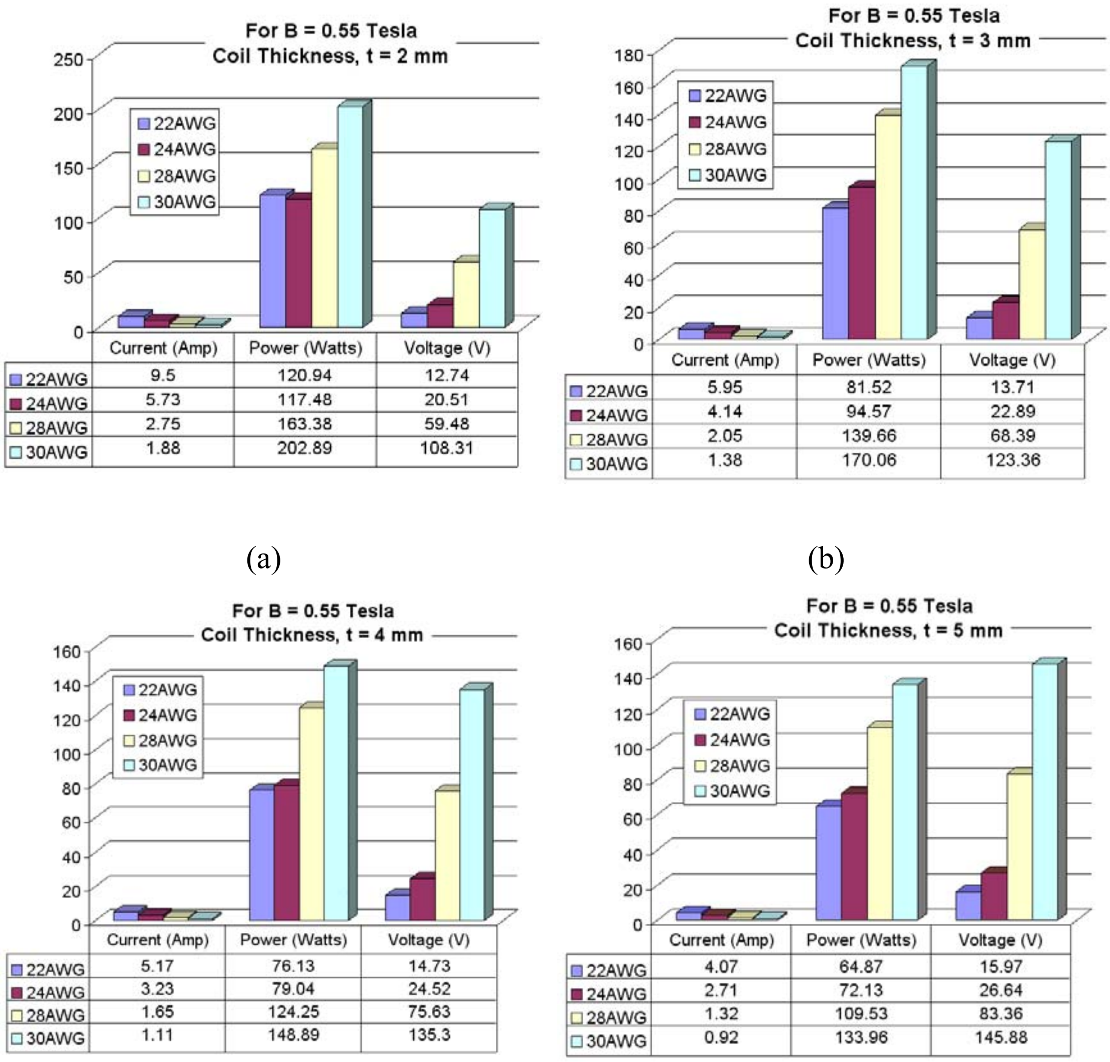

	Current (Amp)	Power (Watts)	Voltage (V)
22AWG	9.5	120.94	12.74
24AWG	5.73	117.48	20.51
28AWG	2.75	163.38	59.48
30AWG	1.88	202.89	108.31

(a)

	Current (Amp)	Power (Watts)	Voltage (V)
22AWG	5.95	81.52	13.71
24AWG	4.14	94.57	22.89
28AWG	2.05	139.66	68.39
30AWG	1.38	170.06	123.36

(b)

	Current (Amp)	Power (Watts)	Voltage (V)
22AWG	5.17	76.13	14.73
24AWG	3.23	79.04	24.52
28AWG	1.65	124.25	75.63
30AWG	1.11	148.89	135.3

(c)

	Current (Amp)	Power (Watts)	Voltage (V)
22AWG	4.07	64.87	15.97
24AWG	2.71	72.13	26.64
28AWG	1.32	109.53	83.36
30AWG	0.92	133.96	145.88

(d)

Figure 5.10: Current, power and voltage variation at flux density, B = 0.55 Tesla for coil thickness; (a) t = 2mm; (b) t = 3mm; (c) t = 4mm and (d) t = 5mm.

Subsequently, figure 5.10 shows all the variations of circuit current, power and voltage drop for the desired flux density, (B) = 0.55 Tesla. The corresponding values of required current flow, power consumption and voltage drop were determined by data analysis in *Microsoft Office Excel 2003* using the simulation results obtained from FEMM. Moreover, variations of power and average flux density with current for individual coil thicknesses are further summarized in the appendix C.

Analyzing these simulation results, for the coil thickness, t = 3 mm, *22 AWG with 420 turns in 5 layers*; for coil thickness, t = 4 mm, *22 AWG with 504 turns in 6 layers* and for coil thickness, t = 5 mm, *22 AWG with 672 turns in 8 layers* showed superior prospects as their required power consumption and voltage drop were low in comparison with the rest. In other cases, either it required a high level of current flow or the power consumption was too high to be convenient. Eventually, for the coil thickness, t = 5 mm, *22 AWG with 672 turns in 8 layers* was preferred due to its average required current flow and voltage drop for lowest power consumption. Subsequently, this data were again used as inputs in FEMM for evaluation purpose. The results are shown in table 5.3.

Table 5.3: Comparison between data analysis and FEMM result for 22 AWG with 5 mm coil thickness.

Coil Thickness, t = 5 mm		**Data Analysis Result**	**FEMM Result**	**Percentage Error (%)**
Average Flux Density (B.n) (Tesla)	22 AWG 672 turns	0.55*	0.56	1.81
Current (I) (Amp)	22 AWG 672 turns	4.07**		
Power (P) (Watts)	22 AWG 672 turns	64.87	65.06	0.29
Voltage (V) (Volts)	22 AWG 672 turns	15.97	15.98	0.062

** Desired Value*
*** Input Data*

Next, figure 5.11 shows the verified flux density plot of 22 AWG with 672 turns in 8 layers with 5 mm coil thickness.

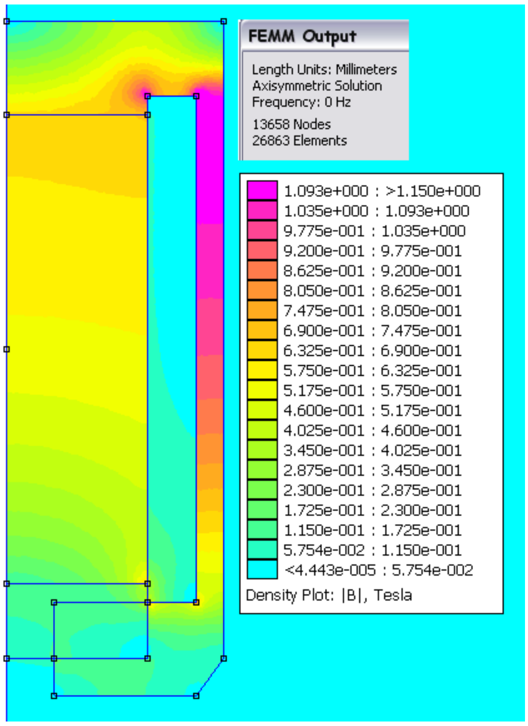

FEMM Output

Length Units: Millimeters
Axisymmetric Solution
Frequency: 0 Hz
13658 Nodes
26863 Elements

1.093e+000 : >1.150e+000
1.035e+000 : 1.093e+000
9.775e-001 : 1.035e+000
9.200e-001 : 9.775e-001
8.625e-001 : 9.200e-001
8.050e-001 : 8.625e-001
7.475e-001 : 8.050e-001
6.900e-001 : 7.475e-001
6.325e-001 : 6.900e-001
5.750e-001 : 6.325e-001
5.175e-001 : 5.750e-001
4.600e-001 : 5.175e-001
4.025e-001 : 4.600e-001
3.450e-001 : 4.025e-001
2.875e-001 : 3.450e-001
2.300e-001 : 2.875e-001
1.725e-001 : 2.300e-001
1.150e-001 : 1.725e-001
5.754e-002 : 1.150e-001
<4.443e-005 : 5.754e-002
Density Plot: |B|, Tesla

Figure 5.11: Flux density plot for 22 AWG with 672 turns in 8 layers; coil thickness, t = 5 mm.

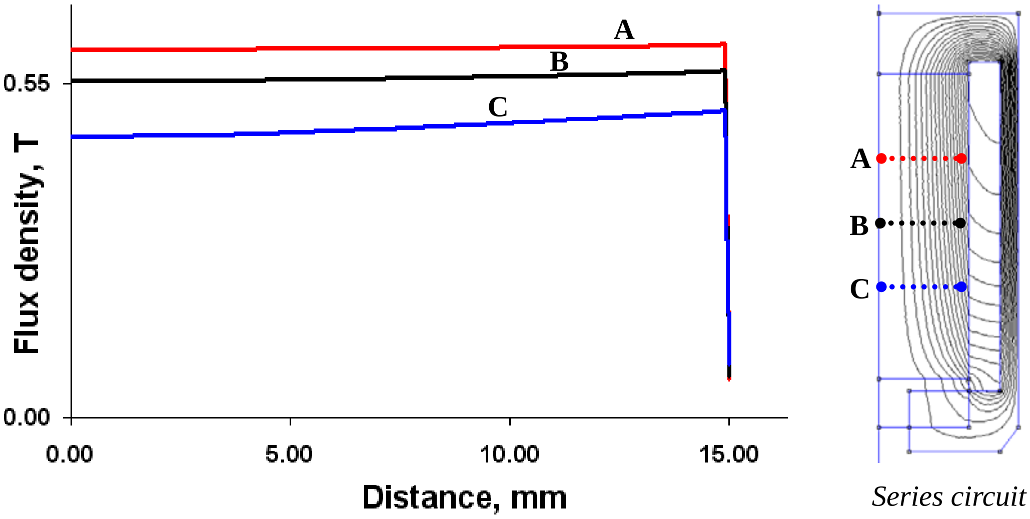

Series circuit

Figure 5.12: Change of flux density at different sections along the 15 mm half-section of the Terfenol-D shaft for 22 AWG with 672 turns in 8 layers.

Furthermore, figure 5.12 shows the change of flux density along the 15 mm half-section of the Terfenol-D shaft. The data series represented the flux density variation at different sections shown as the corresponding coloured contour lines on the right. According to figure 5.12, the flux density values were more or less consistent at an average flux density of 0.55 Tesla, which was excellent due to the fact that there would be no major fluctuations of flux density that the Terfenol-D member would have to encounter, resulting in some maximum possible strain of the member itself.

5.4.2 Magnetostatic parallel circuitry

In order to reduce the power consumption, a parallel coil circuitry was implemented as a trial basis in the FEMM magnetics simulation.

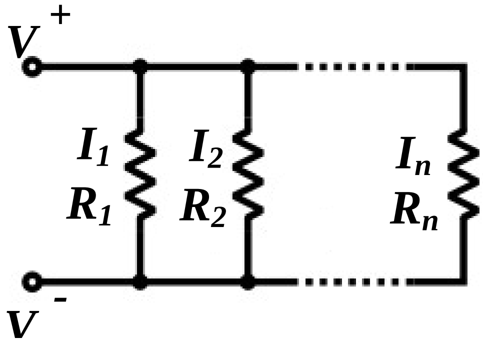

Figure 5.13: Parallel circuit.

Generally, if two or more components are connected in parallel, they have the same potential difference (voltage) across their ends, as shown in figure 5.13. Furthermore, the potential differences across the components are the same in magnitude having identical polarities. The total current *I* is actually the sum of the currents through the individual components.

$$I_{Total} = V\left(\frac{1}{R_1} + \frac{1}{R_2} + \cdots + \frac{1}{R_n}\right) \tag{5-18}$$

$$I_{Total} = I_1 + I_2 + \cdots + I_n \tag{5-19}$$

The current in each individual resistor could be found by Ohm's Law.

$$I_i = \frac{V}{R_i} \tag{5-20}$$

The total resistance, however, is the sum of the reciprocals of each component resistance.

$$\frac{1}{R_{Total}} = \frac{1}{R_1} + \frac{1}{R_2} + \cdots + \frac{1}{R_n} \tag{5-21}$$

The total power of the parallel circuit is,

$$P_{Total} = P_1 + P_2 + \cdots + P_n \tag{5-22}$$

Now, according to the FEMM results analysis, in order to achieve flux density of 0.55 Tesla to actuate the desired amount of injector lift of 50 microns, the preferred prerequisite was a coil of 5 mm thickness comprising 22 AWG with 672 turns in 8 layers with 4.07 amps current flow. In order to reduce the power consumption using parallel circuitry, four coils each having coil number of turns of 168 was connected in parallel. In this manner, each new coil would have the identical coil resistance. The total current, therefore, would be divided into four equal proportions of 1.0175 amps going through each coil.

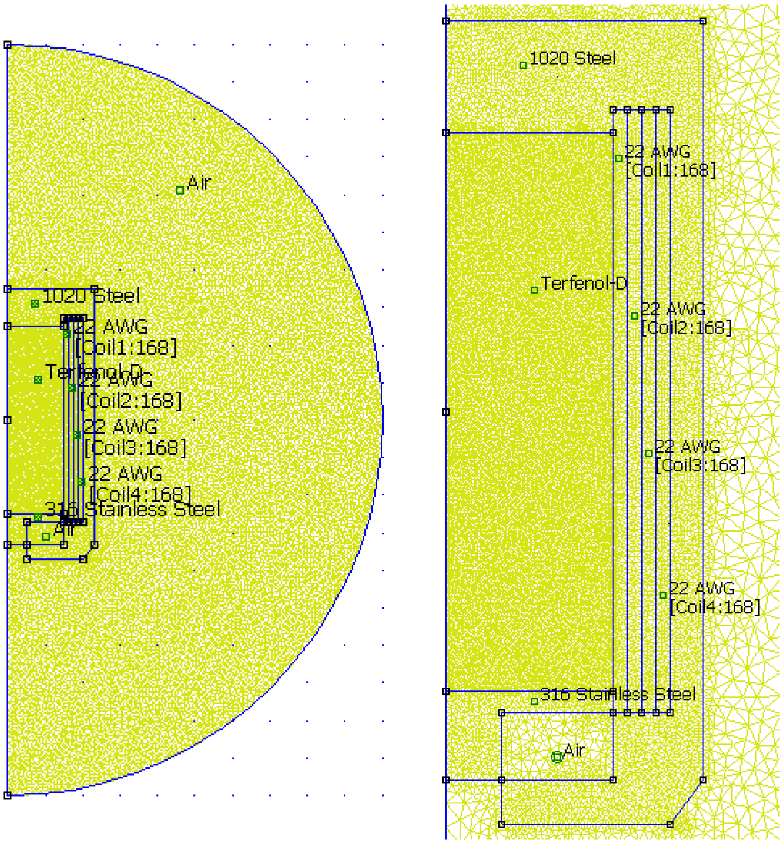

Figure 5.14: Parallel coil circuitry in FEMM.

Although, a current of 1.0175 amps through each coil or total current of 4.07 was thought to provide the same magnetic field strength, the parallel circuitry was unable to create the desired amount of flux density with that magnitude of current flow, as shown in figure 5.15. The reason behind this phenomenon might be, as the individual parallel coil number of turns was reduced, it resulted in generating less magnetic field strength for a given current flow and coil length.

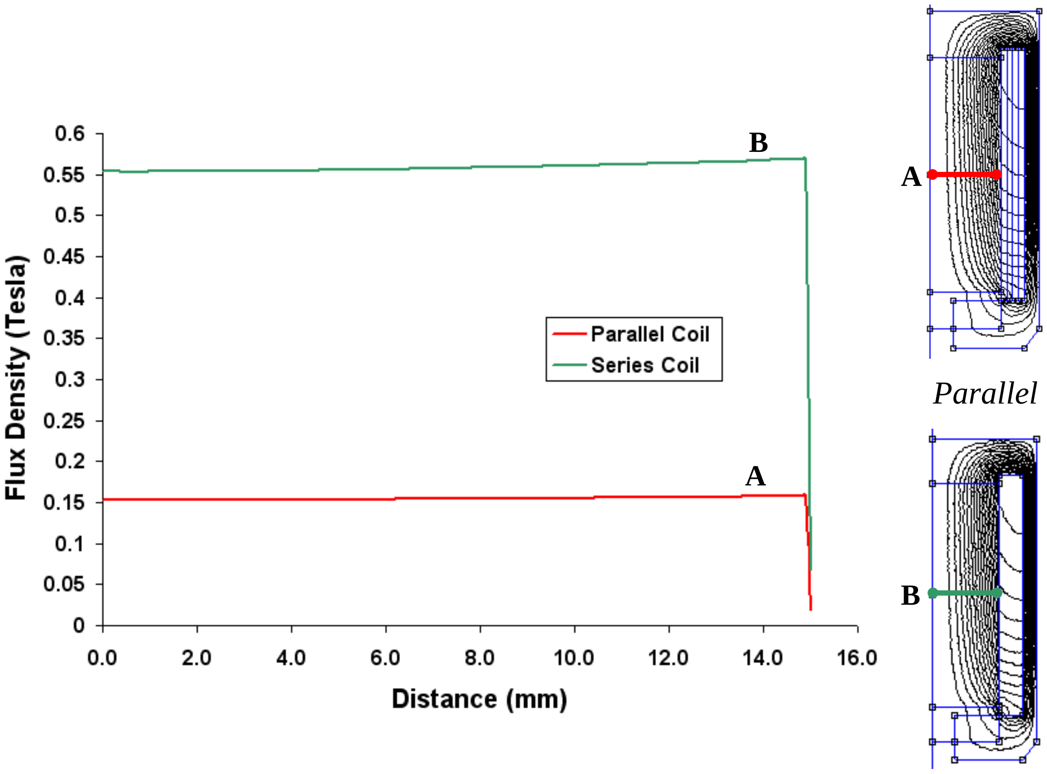

Parallel

Series

Figure 5.15: Flux density variation for parallel and series coil circuitry.

Eventually it was found that, an individual current flow of 4.07 amps in each parallel coil was essential to create the desired flux density of 0.55 Tesla, as shown in figure 5.16. In that case, however, although the total current flow became 16.28 amps, the total power level remained 65.02 Watts. Thus, the concluding remark would be, although it required 16.28 amps total current to derive the magnetic flux density of 0.55 Tesla necessary to cause the magnetostrictive strain, both total power and voltage drop were low considering the total current of the parallel circuit. However, the total power of the parallel circuit was unchanged compared to the series circuit having the current flow of 4.07 amps. The parallel circuit properties for 22 AWG with 672 turns in 8 layers is depicted in figure 5.17.

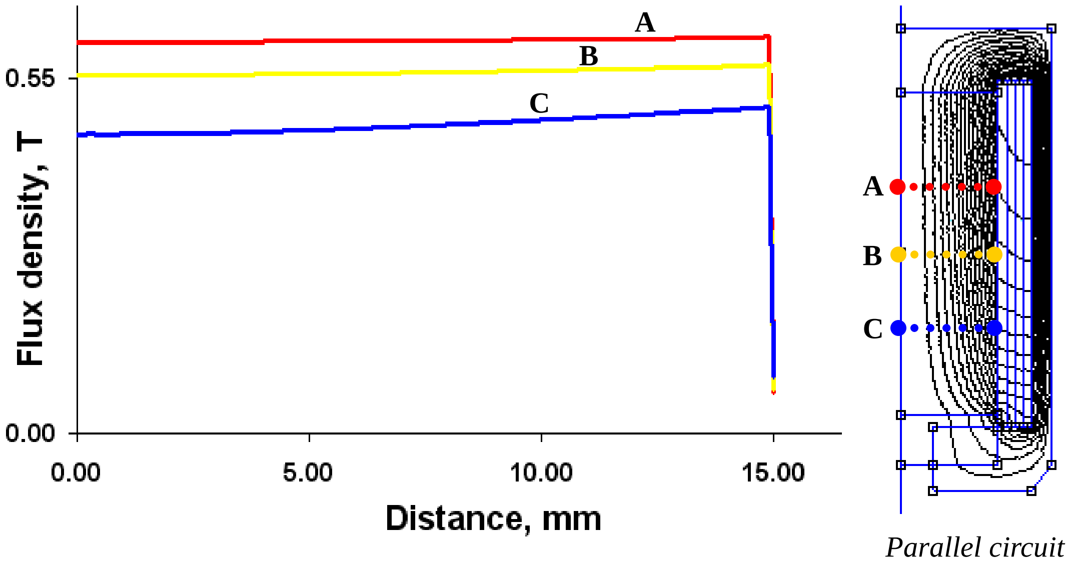

Figure 5.16: Change of flux density at different sections along the 15 mm half-section of the Terfenol-D shaft for 22 AWG with 672 turns in 8 layers (t = 5 mm).

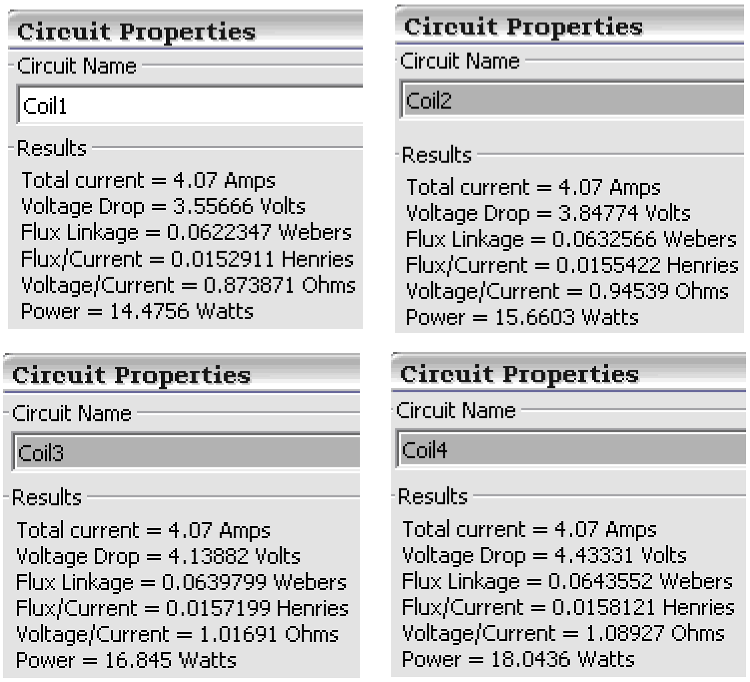
Circuit Properties
Circuit Name
Coil1
Results
Total current = 4.07 Amps
Voltage Drop = 3.55666 Volts
Flux Linkage = 0.0622347 Webers
Flux/Current = 0.0152911 Henries
Voltage/Current = 0.873871 Ohms
Power = 14.4756 Watts

Circuit Properties
Circuit Name
Coil2
Results
Total current = 4.07 Amps
Voltage Drop = 3.84774 Volts
Flux Linkage = 0.0632566 Webers
Flux/Current = 0.0155422 Henries
Voltage/Current = 0.94539 Ohms
Power = 15.6603 Watts

Circuit Properties
Circuit Name
Coil3
Results
Total current = 4.07 Amps
Voltage Drop = 4.13882 Volts
Flux Linkage = 0.0639799 Webers
Flux/Current = 0.0157199 Henries
Voltage/Current = 1.01691 Ohms
Power = 16.845 Watts

Circuit Properties
Circuit Name
Coil4
Results
Total current = 4.07 Amps
Voltage Drop = 4.43331 Volts
Flux Linkage = 0.0643552 Webers
Flux/Current = 0.0158121 Henries
Voltage/Current = 1.08927 Ohms
Power = 18.0436 Watts

Figure 5.17: The parallel circuit properties for 22 AWG with 672 turns in 8 layers (t = 5 mm).

Table 5.4: Summary of the results between series and parallel circuit properties

At B = 0.55 T *22 AWG with 672 turns in 8 layers; t = 5 mm*	**Parallel Circuit**				**Series Circuit**	**Remarks**
	Coil 1	***Coil 2***	***Coil 3***	***Coil 4***		
Total Current (amps)	4.07	4.07	4.07	4.07	4.07	Higher parallel circuit current
	16.28 (=Σ)					
Voltage Drop (Volts)	3.56	3.84	4.13	4.43	15.97	Lower parallel circuit voltage
	4 (=avg)					
Power (watts)	14.47	15.66	16.84	18.04	64.87	Identical power
	65.01 (=Σ)					

Furthermore, table 5.4 describes the summary of the results between series and parallel circuit properties to achieve the desired flux density of 0.55 Tesla for 22 AWG with 672 turns in 8 layers.

5.4.3 Time-harmonic series circuitry

In order to acquire further understanding regarding the variation of magnetic field strength with varying frequencies, the FEMM magnetic simulations were repeated again as harmonic magnetic problems with frequencies 10 Hz, 20 Hz, 50 Hz, 100 Hz, 250 Hz and 500 Hz. In this time-harmonic scenario, a series coil circuitry was used which had a coil thickness of 5 mm and was composed of 22 AWG with 672 turns in 8 layers. According to the previous findings, a current flow of 4.07 amps was applied as input circuit parameter to achieve the desired flux density of 0.55 Tesla.

According to figure 5.18, the flux density distribution along the 15 mm half-section of the Terfenol-D shaft was identical to that of magnetostatic series circuitry with the same amount of current flow. However, as the frequency was increased from 0 Hz to 10 Hz, an abrupt increase in the flux density was observed, as shown in figure 5.18 (d). Subsequently, as the frequency was increased further, the average value of flux density tended to decrease again, as shown in figure 5.18 (b)-(c).

Although this phenomenon had occurred over a fraction of flux density values, nevertheless, it was an evident feature.

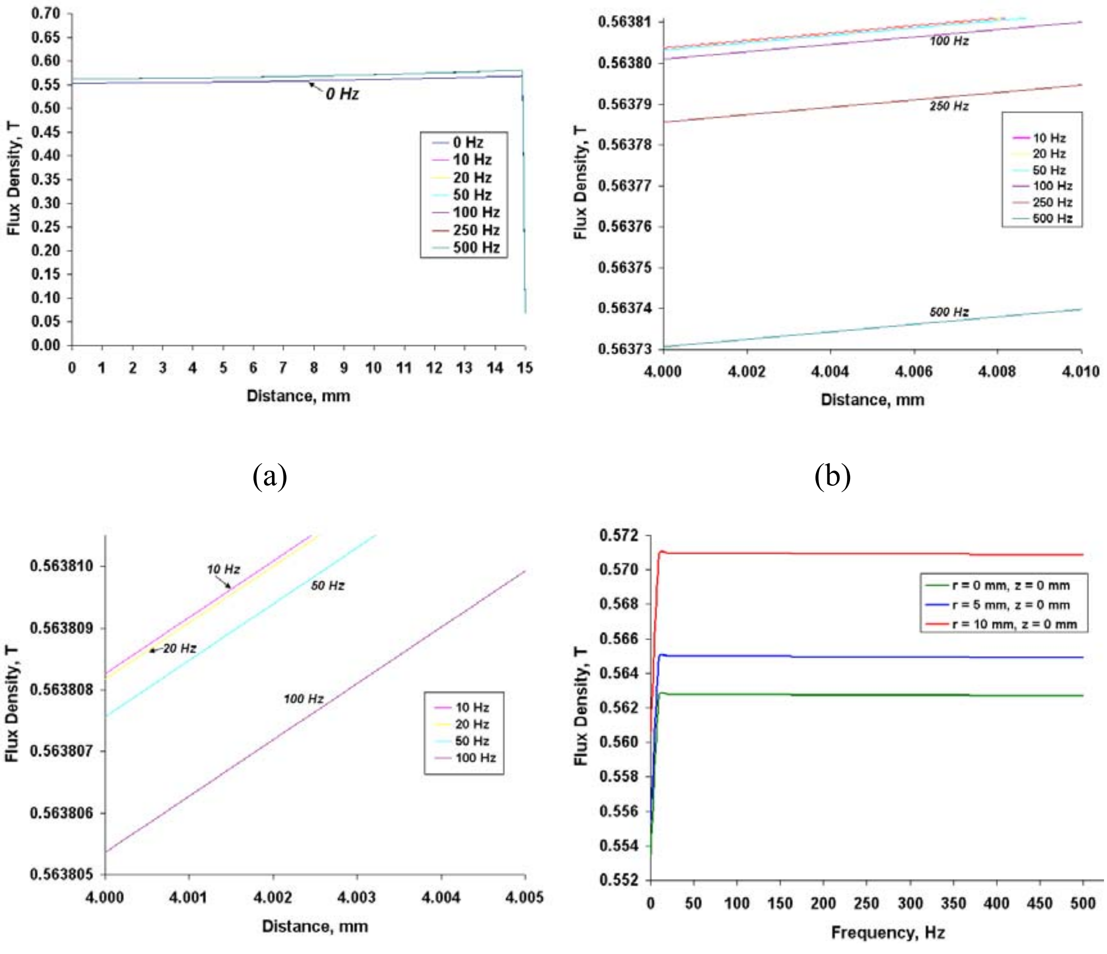

(a) (b)

(c) (d)

Figure 5.18: Variation of flux density for 22 AWG with 672 turns in 8 layers with 4.07 amps input current; (a) flux density vs. distance at different frequencies; (b) zoom in view of flux density vs. distance showing for 100 Hz, 250 Hz and 500 Hz; (c) zoom in view of flux density vs. distance showing for 10 Hz, 20 Hz, 50 Hz and 100 Hz; (d) Flux density vs. frequency at the points (0,0), (5,0) and (10,0).

Furthermore, figure 5.19 shows the flux density vector plot and all the time-harmonic series circuit properties output.

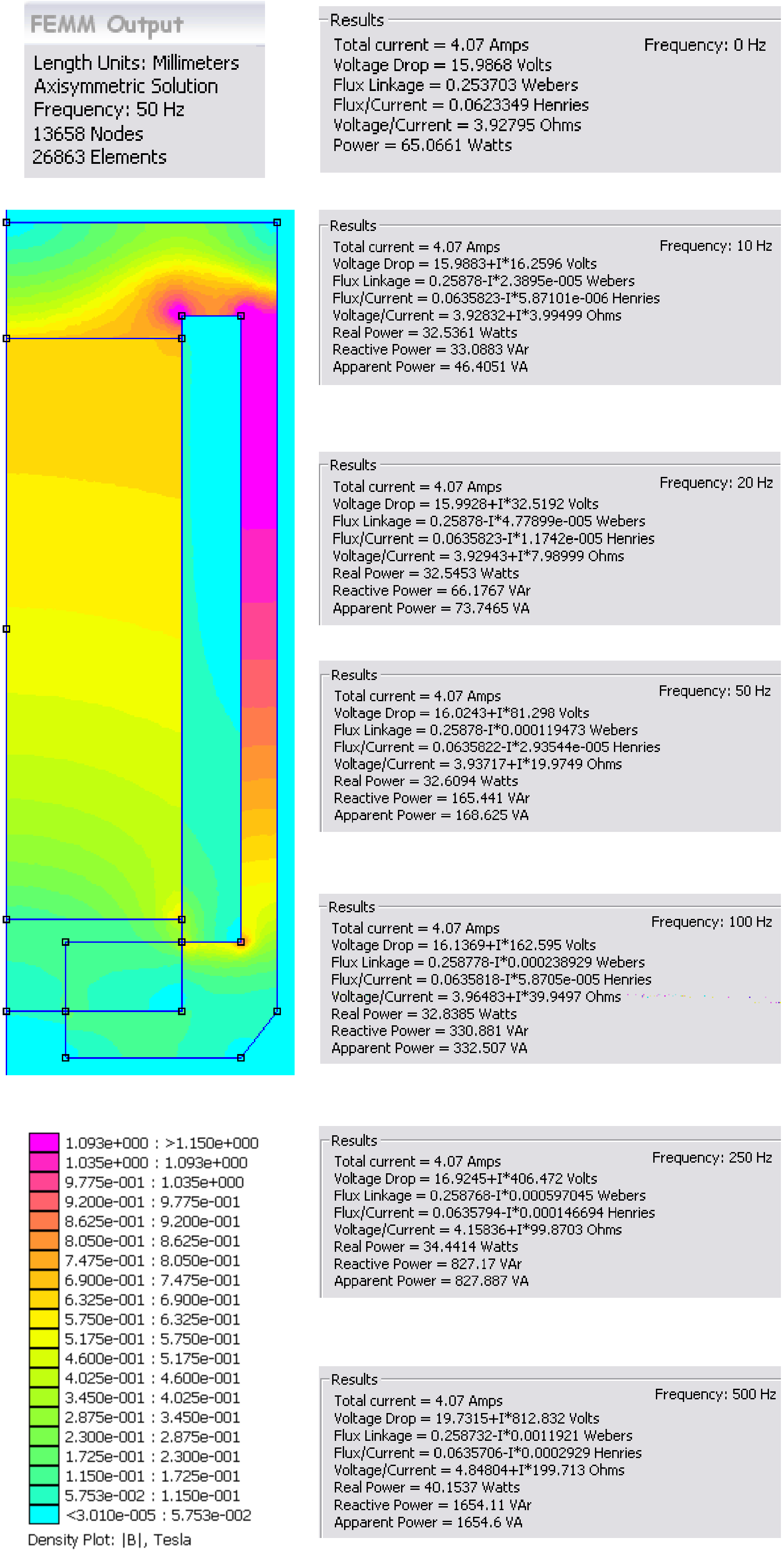

```
Length Units: Millimeters
Axisymmetric Solution
Frequency: 50 Hz
13658 Nodes
26863 Elements
```

```
Results
Total current = 4.07 Amps                    Frequency: 0 Hz
Voltage Drop = 15.9868 Volts
Flux Linkage = 0.253703 Webers
Flux/Current = 0.0623349 Henries
Voltage/Current = 3.92795 Ohms
Power = 65.0661 Watts
```

```
Results
Total current = 4.07 Amps                    Frequency: 10 Hz
Voltage Drop = 15.9883+I*16.2596 Volts
Flux Linkage = 0.25878-I*2.3895e-005 Webers
Flux/Current = 0.0635823-I*5.87101e-006 Henries
Voltage/Current = 3.92832+I*3.99499 Ohms
Real Power = 32.5361 Watts
Reactive Power = 33.0883 VAr
Apparent Power = 46.4051 VA
```

```
Results
Total current = 4.07 Amps                    Frequency: 20 Hz
Voltage Drop = 15.9928+I*32.5192 Volts
Flux Linkage = 0.25878-I*4.77899e-005 Webers
Flux/Current = 0.0635823-I*1.1742e-005 Henries
Voltage/Current = 3.92943+I*7.98999 Ohms
Real Power = 32.5453 Watts
Reactive Power = 66.1767 VAr
Apparent Power = 73.7465 VA
```

```
Results
Total current = 4.07 Amps                    Frequency: 50 Hz
Voltage Drop = 16.0243+I*81.298 Volts
Flux Linkage = 0.25878-I*0.000119473 Webers
Flux/Current = 0.0635822-I*2.93544e-005 Henries
Voltage/Current = 3.93717+I*19.9749 Ohms
Real Power = 32.6094 Watts
Reactive Power = 165.441 VAr
Apparent Power = 168.625 VA
```

```
Results
Total current = 4.07 Amps                    Frequency: 100 Hz
Voltage Drop = 16.1369+I*162.595 Volts
Flux Linkage = 0.258778-I*0.000238929 Webers
Flux/Current = 0.0635818-I*5.8705e-005 Henries
Voltage/Current = 3.96483+I*39.9497 Ohms
Real Power = 32.8385 Watts
Reactive Power = 330.881 VAr
Apparent Power = 332.507 VA
```

```
Results
Total current = 4.07 Amps                    Frequency: 250 Hz
Voltage Drop = 16.9245+I*406.472 Volts
Flux Linkage = 0.258768-I*0.000597045 Webers
Flux/Current = 0.0635794-I*0.000146694 Henries
Voltage/Current = 4.15836+I*99.8703 Ohms
Real Power = 34.4414 Watts
Reactive Power = 827.17 VAr
Apparent Power = 827.887 VA
```

```
Results
Total current = 4.07 Amps                    Frequency: 500 Hz
Voltage Drop = 19.7315+I*812.832 Volts
Flux Linkage = 0.258732-I*0.0011921 Webers
Flux/Current = 0.0635706-I*0.0002929 Henries
Voltage/Current = 4.84804+I*199.713 Ohms
Real Power = 40.1537 Watts
Reactive Power = 1654.11 VAr
Apparent Power = 1654.6 VA
```

Figure 5.19: FEMM time-harmonic series circuitry results output.

5.5 Summary of chapter five

According to the FEMM magnetic simulation results, for a coil thickness of 5 mm with 22 AWG wire having 672 turns in 8 layers, showed good prospect in actuating the desired amount of injector lift of 50 microns as the required magnetic field strength was achieved to cause the necessary amount of strain following the prestress of 1 KSI in the Terfenol-D strain chart. Furthermore, in case of magnetostatic parallel coil, it was observed that higher parallel circuit current and lower parallel circuit voltage were required to achieve the desired flux density of 0.55 Tesla, while the coil power remained identical in both cases. Moreover, in case of time harmonic series circuit, by implementing the frequency factor, apparently the flux density seemed to increase suddenly. The reason behind the phenomenon of the slight increase in flux density might be due to the fact that, as the frequency was increased slightly, the rate of change electric field was increased also. As the strength of the magnetic field is proportional to the time rate of the change of the electric field, this would have resulted in an increase of magnetic field strength, resulting in an increase in flux density. A concise and inclusive overview of the highlighted research process of this chapter is shown in figure 5.20.

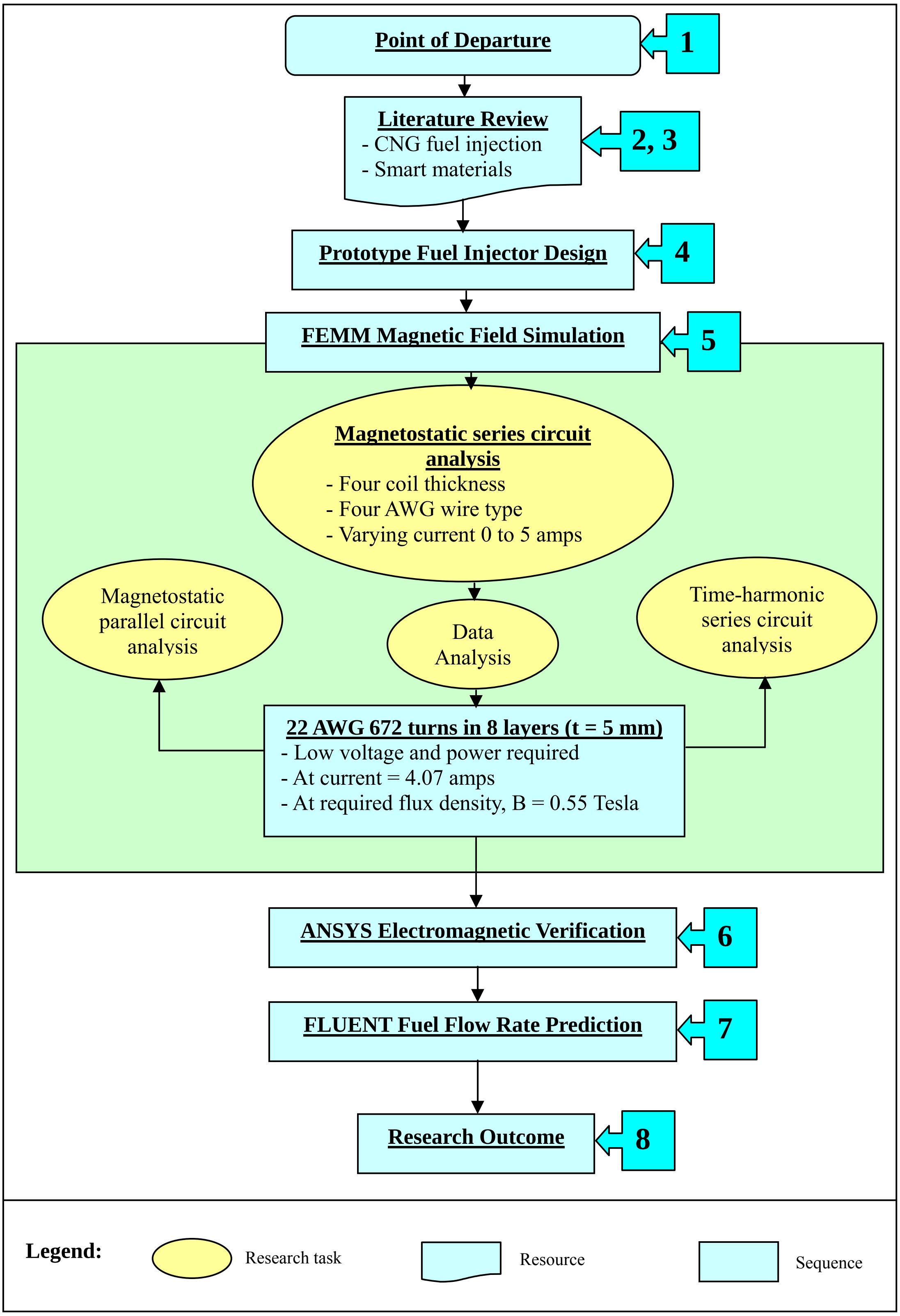

Figure 5.20: Summary of the research process in chapter five.

CHAPTER SIX

ANSYS ELECTROMAGNETIC VERIFICATION

6.1 Introduction

ANSYS is a general purpose finite element modeling package to numerically solve a wide variety of structural, thermal, fluid dynamics and electromagnetic problems provided by the engineering simulation software provider ANSYS Inc. ANSYS Electromagnetic is a part of ANSYS, Inc software products which emphasizes in simulating both low and high frequency electromagnetic analysis. In order to verify the Finite Element Methods Magnetics (FEMM) result with ANSYS Electromagnetic, a low-frequency electromagnetic analysis was implemented which contained a comprehensive tool set for static, transient and harmonic low-frequency electromagnetic studies, permitting the simulation of electrostatic, magnetostatic, electromagnetic, electric circuit and current conduction. ANSYS Electromagnetic also features a complete range of automatic calculations for force, torque, inductance, impedance, capacitance, Joule losses, field leakage, saturation, and electric and magnetic field strengths [123]. The ANSYS software package that was utilized to verify the results of FEMM was *ANSYS Academic Teaching Introductory, Release 11.0 SP1*.

6.2 Low-frequency electromagnetic analysis

In case of low-frequency, the ANSYS program uses Maxwell’s equations as the basis for electromagnetic field analysis. Magnetic field quantities such as magnetic flux density, current density, force, loss, inductance, energy and capacitance are generally derived from primary unknowns like *magnetic and electric potentials*, often referred as *degrees of freedom*. The finite element solution actually tries to calculate these degrees of freedom, which can either be a *scalar* or *vector* magnetic potential, as well as edge flux, non-time integrated and time integrated electric potential.

In this case, the FEMM results analysis was verified against a 2-D static magnetic analysis which analyzes magnetic field caused by direct current (DC). In order to verify the results, the same optimized current of 4.07 amps was used as input parameter which was supposed to yield a magnetic flux density of 0.55 Tesla causing the necessary strain in Terfenol-D shaft. Now, in ANSYS electromagnetic, any current flow parameter had to be entered as an input in terms of *current density*.

This current density, J, could be defined as the number of coil windings times the current, divided by the coil area, as shown in figure 6.1.

$$J = \frac{NI}{A} \tag{6-1}$$

Where, N = number of turns, I = current flow and A = coil cross section area.

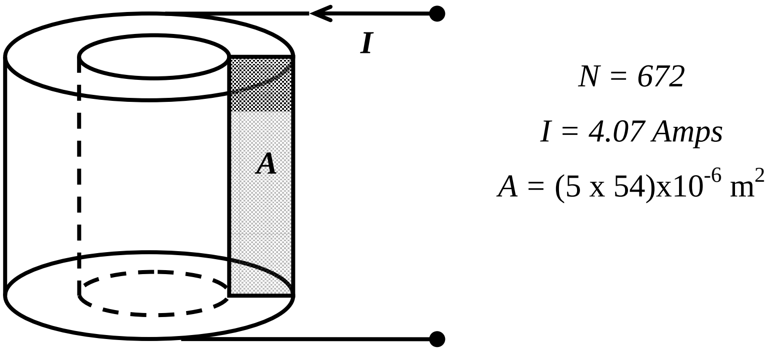

Figure 6.1: Current density.

Although static magnetic analysis primarily enables the option to model both saturable and non-saturable magnetic materials, as well as permanent magnets, it does not consider time-dependent effects such as eddy currents.

6.2.1 Element type used in 2-D static magnetic analysis

In order to represent the geometry of the structure, the two-dimensional injector model was constituted by a two-dimensional element in the static magnetic analysis. Generally, modeling through this approach is much easier to generate and usually takes less time to solve. Eventually, this 2-D static magnetic nodal analysis was executed with *PLANE13*, which was a two dimensional, coupled solid element type having up to four degrees of freedom per node. These degrees of freedom could be magnetic vector potential (AZ), displacements, temperature or time-integrated electric potential. Furthermore, PLANE13 had a 2-D magnetic, thermal, electrical, piezoelectric and structural field capability with limited coupling between the fields. The shape or characteristics of PLANE13 could either be a *4-node quadrilateral* or *3-node triangular*, as shown in figure 6.2. In this simulation problem, however, the 4-node quadrilateral shape was preferred.

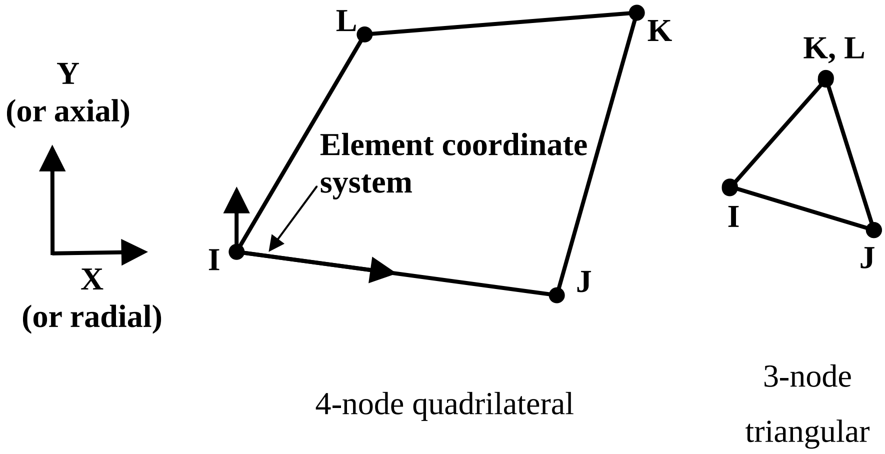

Figure 6.2: PLANE13 element type geometry with nodes I, J, K and L.

PLANE13 also featured nonlinear magnetic capability for modeling B-H curve which facilitated in defining Terfenol-D non-linear B-H material property. Furthermore, according to PLANE13 element type input characteristics, it did not require defining any *real constants* in ANSYS Electromagnetic interface.

6.2.2 Magnetic formulation

ANSYS Electromagnetic offers several formulations, depending on the type of analysis, the material properties and the overall characteristics of the analysis. ANSYS supports two nodal-based formulation methods; (a) the *magnetic scalar potential (MSP)* formulation, and (b) the *magnetic vector potential (MVP)* formulation. Where MSP formulation is appropriate only for most 3-D static analysis applications, MVP formulation is preferable for both 2-D and 3-D dimensions with static, harmonic and transient analysis types. Furthermore, MVP formulation has three more degrees of freedom (DOF) per node than the scalar method. These are magnetic vector DOFs in the *X*, *Y* and *Z* directions, namely *AX*, *AY* and *AZ*. Voltage-fed or circuit coupled analysis may add up to three additional degrees of freedom to the magnetic vector DOFs. These are namely *current (CURR)*, *electromotive force drop (EMF)*, and *electric potential (VOLT)*. For a 2-D static magnetic analysis, using MVP formulation would result in a single vector potential degree of freedom, *AZ*. Therefore, this ANSYS Electromagnetic simulation incorporating PLANE13 element type was solved with nodal based magnetic vector potential (MVP) formulation method, which in addition, enabled modeling the current conducting regions as an integral part of the finite element model.

6.3 ANSYS Electromagnetic nodal analysis preprocessor

In order to verify the results of FEMM, the ANSYS 2-D static magnetic nodal simulation was carried out for a coil thickness of 5 mm comprising 22 AWG copper coil wire with 672 turns in 8 layers.

6.3.1 Geometry modeling

ANSYS incorporates a *graphical user interface (GUI)* which is an interactive way to perform any analysis without relying on *ANSYS Commands*. Actually, each GUI option activates one or more ANSYS commands to perform the requested operation. However, in case of some operations, ANSYS commands have to be entered in the command input area or via a batch file. Subsequently, utilizing this graphical user interface, a two-dimensional half cross-section injector geometry was modeled in ANSYS, as shown in figure 6.3.

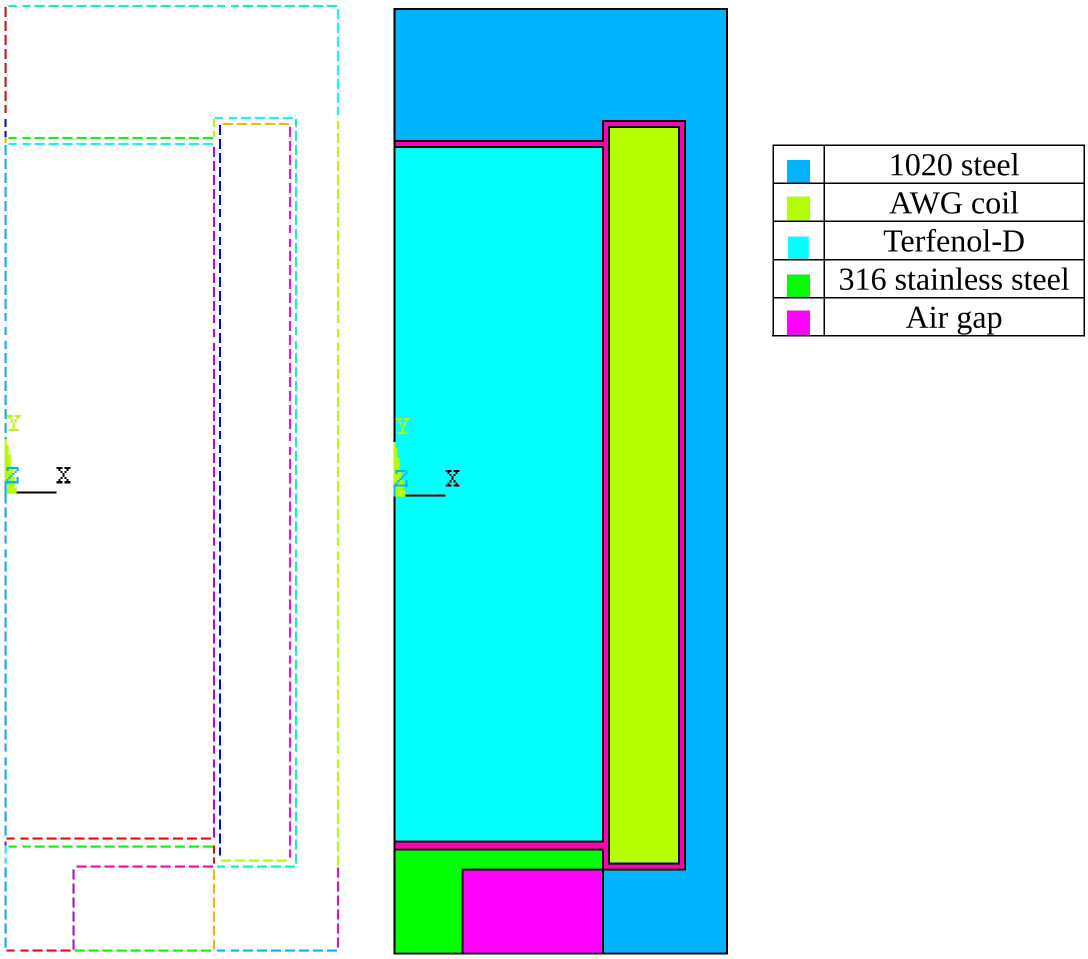

Line plot Area plot

Figure 6.3: 2-D cross-sectional geometry in ANSYS showing line and area plot.

6.3.2 Defining element type and material properties

As discussed earlier, the 2-D static magnetic nodal analysis was executed with *PLANE13* which was a two dimensional, quadrilateral, coupled solid element type having four nodes with up to four degrees of freedom per node. The element behavior was set as axisymmetric, as shown in figure 6.4.

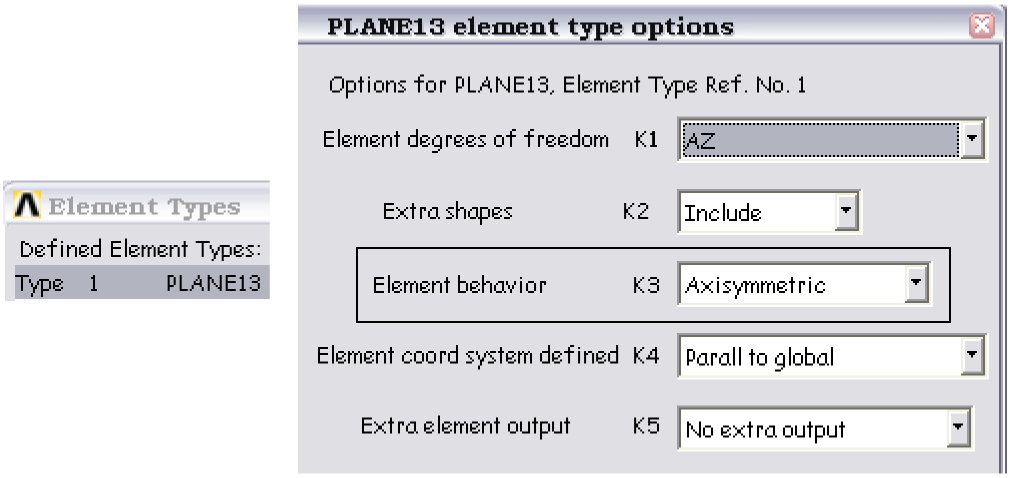

Defined Element Types:
Type 1 PLANE13

Options for PLANE13, Element Type Ref. No. 1

Element degrees of freedom K1 AZ

Extra shapes K2 Include

Element behavior K3 Axisymmetric

Element coord system defined K4 Parall to global

Extra element output K5 No extra output

Figure 6.4: Defining PLANE13 element type.

In order to assign the material properties, the material model behaviors for 1020 steel, 316 stainless steel, air gap and AWG copper wire were defined based on the *constant relative permeability (MURX)* values of the corresponding materials. However, for Terfenol-D, the non-linear B-H characteristics were assigned as the material model properties, as shown in figure 6.5.

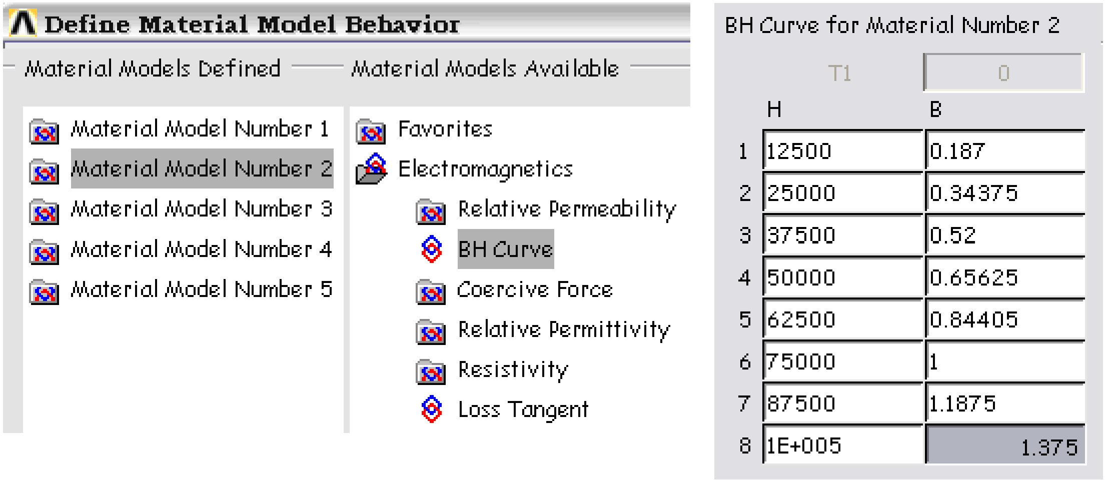

BH Curve for Material Number 2

T1 0

	H	B
1	12500	0.187
2	25000	0.34375
3	37500	0.52
4	50000	0.65625
5	62500	0.84405
6	75000	1
7	87500	1.1875
8	1E+005	1.375

(a) (b)

Figure 6.5: (a) Defining material model behavior, (b) Terfenol-D B-H data input.

In this context, table 6.1 explains the assigned materials against their model numbers.

Table 6.1: Assigned material model number in ANSYS

Material model number in ANSYS	Assigned materials
1	1020 Steel
2	Terfenol-D
3	316 Stainless Steel
4	Copper
5	Air

6.3.3 Meshed geometry

Meshing is a fundamental part of the finite element analysis process, which influences the accuracy, convergence and rapidity of the solution process. ANSYS provides powerful tools for mesh generation irrespective of the geometry, element type, analysis characteristics and application.

Subsequent to creating the geometry and defining the material models, each area representing corresponding material properties were attributed with respective material number and element type, as shown in figure 6.6. Then after implementing the mesh size controls for the corresponding material areas, a *quadratic mesh* was generated throughout the injector cross-sectional area, as shown in figure 6.7.

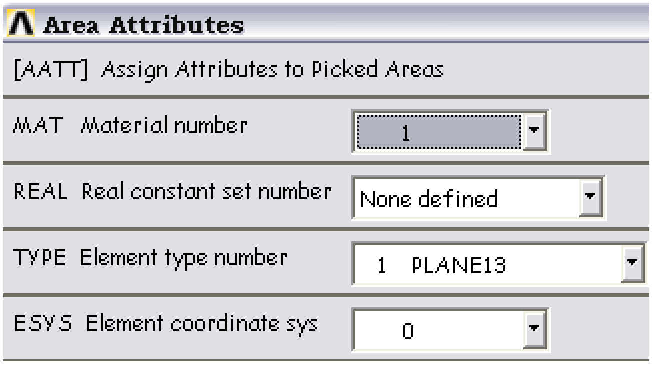

Area Attributes

[AATT] Assign Attributes to Picked Areas

MAT Material number: 1

REAL Real constant set number: None defined

TYPE Element type number: 1 PLANE13

ESYS Element coordinate sys: 0

Figure 6.6: Defining mesh attributes by area.

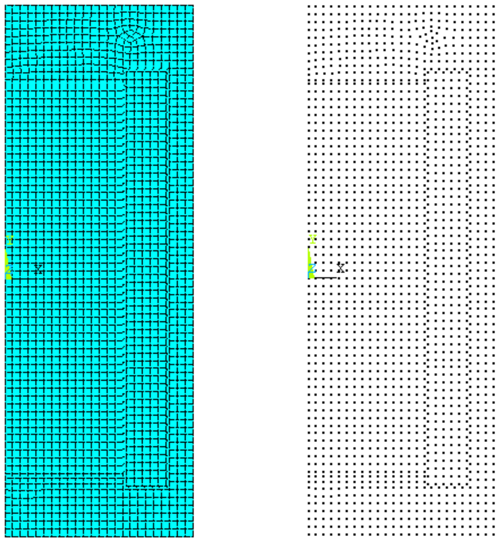

Elements *Nodes*

Figure 6.7: Meshed geometry in ANSYS.

6.3.4 Applying magnetic excitation and boundary condition

As mentioned earlier, ANSYS static magnetic analysis required to enter the current input in terms of *current density*. Furthermore, a perimeter boundary condition was applied to obtain a *flux parallel* field solution. This boundary condition assumed that the flux would not leak out at the perimeter of the model. However, at the centerline, this stipulation was already valid due to the axisymmetric analysis.

Subsequently, to verify the FEMM result with ANSYS, exactly the same amount of direct current flow, coil thickness, and coil number of turns were applied as magnetic excitation in terms of current density. In this case, the coil area or material model number 4 was the region where this current density was assigned. Moreover, the lines around the perimeter of the geometry were selected as the magnetic vector potential boundary, as shown in figure 6.8.

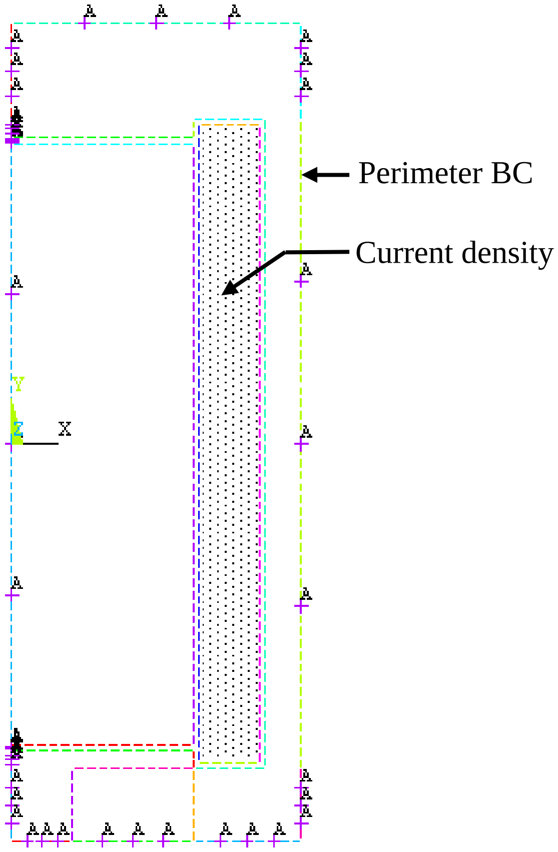

Figure 6.8: Applying current density and boundary condition.

6.4 ANSYS Electromagnetic results

Subsequently, the ANSYS 2-D static magnetic simulation was run with nodal based Magnetic Vector Potential (MVP) formulation, as shown in figure 6.9.

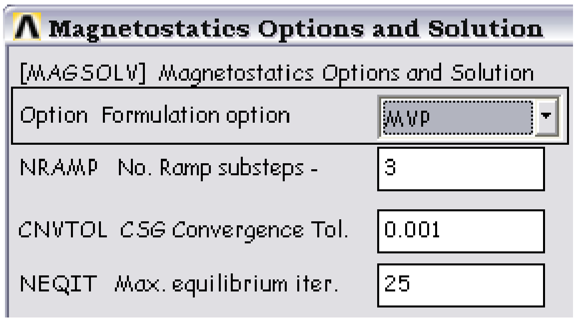
Magnetostatics Options and Solution

[MAGSOLV] Magnetostatics Options and Solution

Option	Formulation option	MVP
NRAMP	No. Ramp substeps -	3
CNVTOL	CSG Convergence Tol.	0.001
NEQIT	Max. equilibrium iter.	25

Figure 6.9: Magnetostatic options and solutions.

Figure 6.10 shows the 2D flux lines and flux density vector sum generated from ANSYS post-processor.

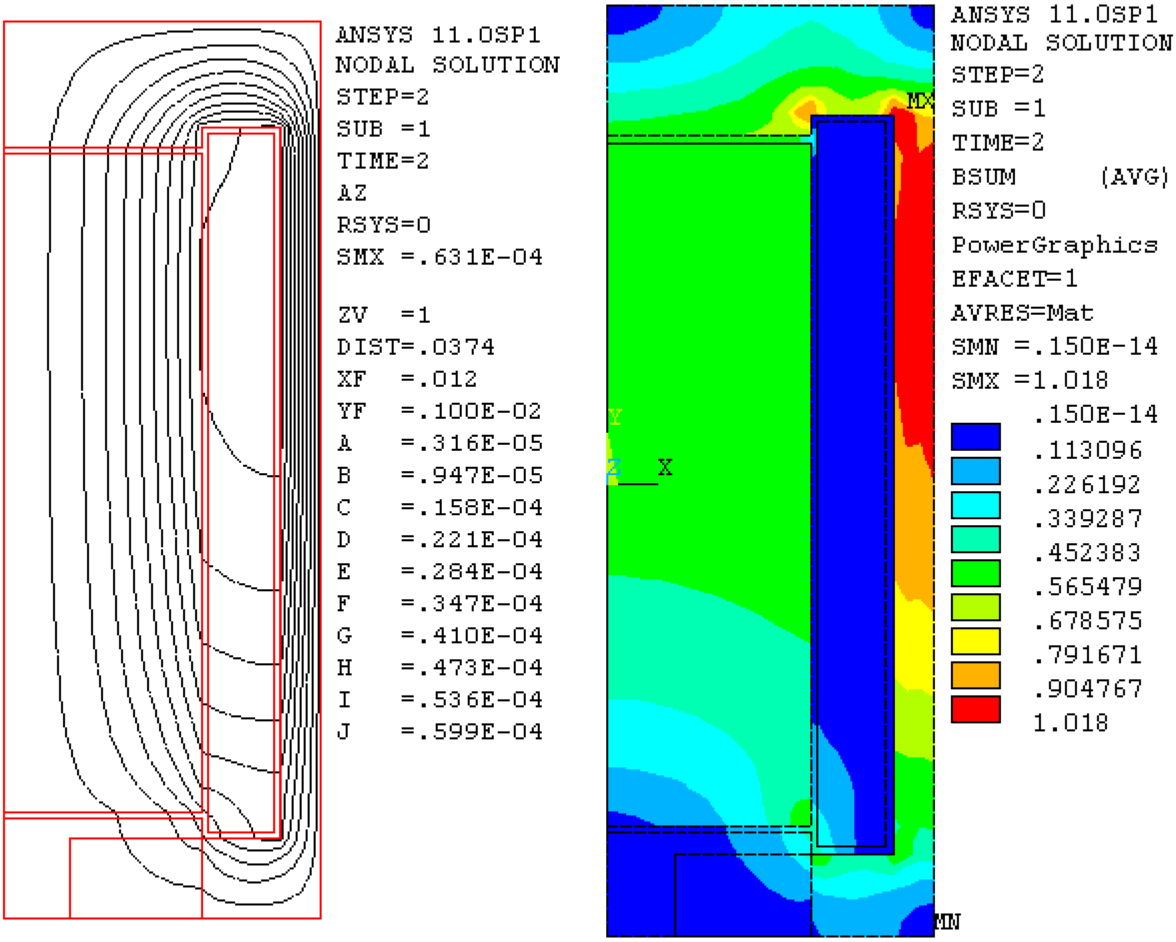

(a) (b)

Figure 6.10: (a) 2D flux lines; (b) Flux density vector sum nodal solution.

The resultant flux density vector sum represented the magnitude of flux density generated at each node without averaging the results across material discontinuities. Furthermore, figure 6.11 shows the flux density distribution throughout the entire injector actuator by producing a half (½) expanded plot representation based on the defined axisymmetry.

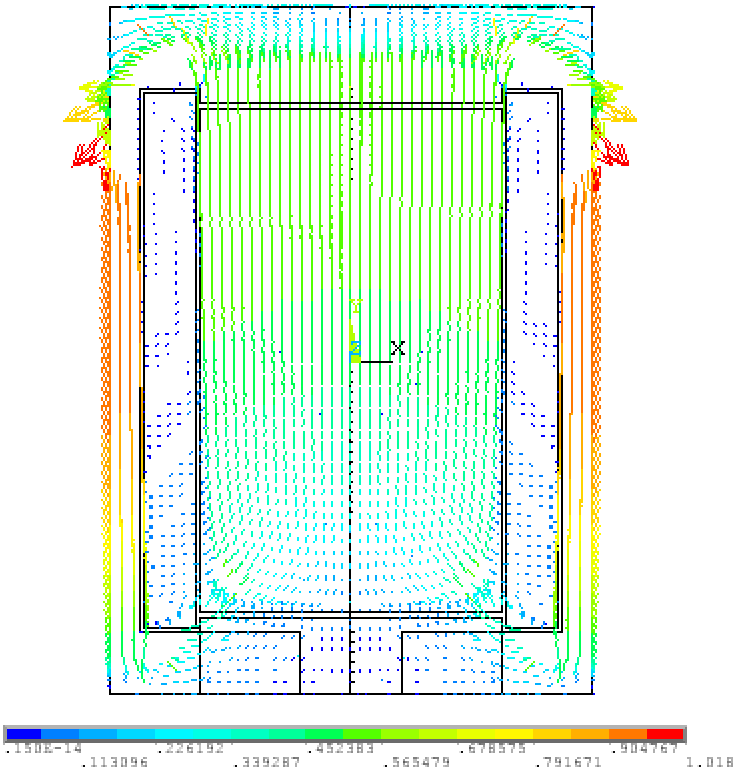

Figure 6.11: Flux density vector sum vector plot for 2D ½ expansion.

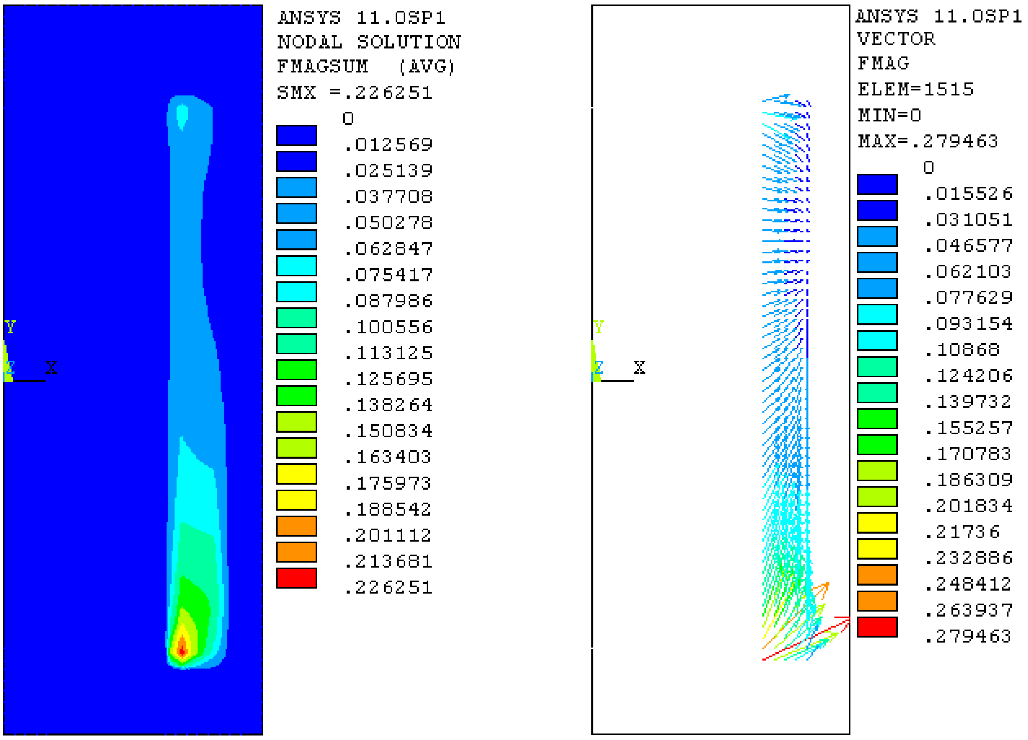

(a) (b)

Figure 6.12: Electromagnetic force calculation, (a) Nodal solution, and (b) Vector plot.

Moreover, figure 6.12 represents electromagnetic force calculations on element components, where the command *FMAGSUM* invoked an ANSYS macro that summarized the Maxwell forces. As seen from figure 6.12, a relatively higher electromagnetic force was generated in the region of the coil area which was closer to the non-magnetic plunger zone.

6.5 ANSYS and FEMM results verification

As described earlier, in order to verify the FEMM result with that of ANSYS, exact same amount of direct current flow, coil thickness, and coil number of turns were applied as magnetic excitation in terms of current density. Figure 6.13 explains the comparison between the resultant flux density vector sum output for both FEMM and ANSYS.

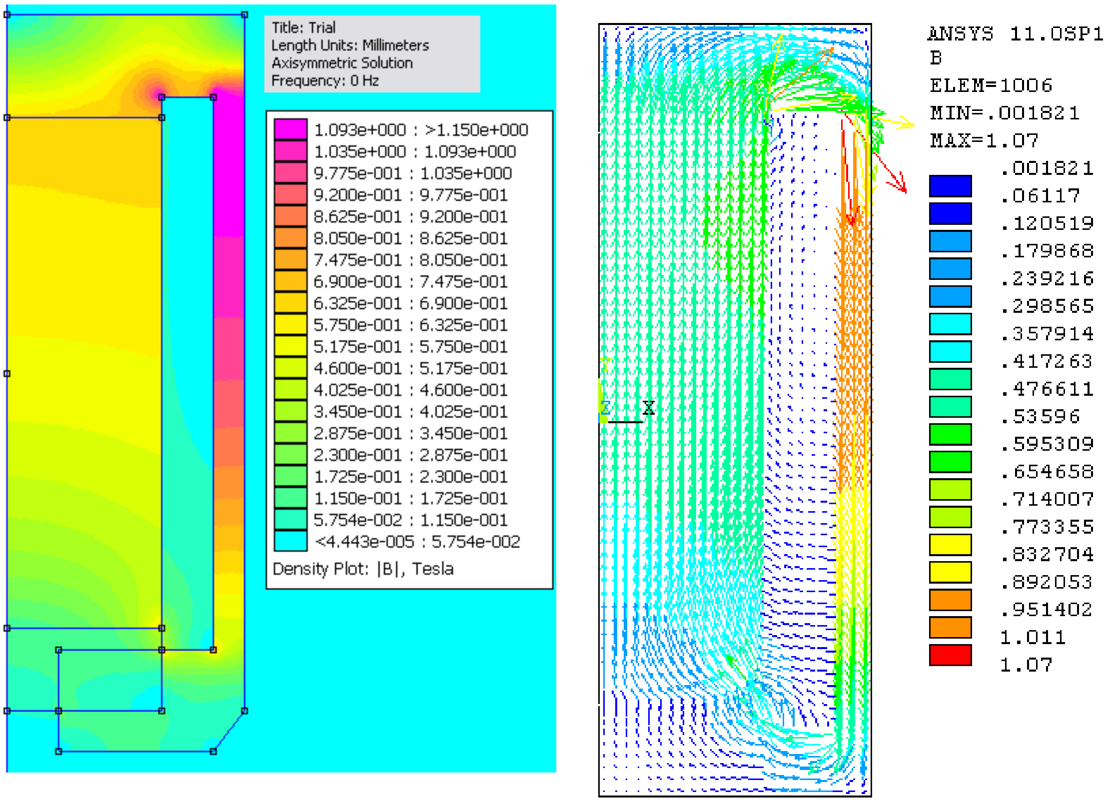

(a) (b)

Figure 6.13: Flux density plot; (a) FEMM output, and (b) ANSYS output.

Figure 6.14 explains the flux density distribution along the three different contour lines. As seen from the figure 6.14, the flux density distribution stays more or less uniform along the different contour regions, implying no major fluctuations of flux density along the Terfenol-D member resulting in maximum possible strain output.

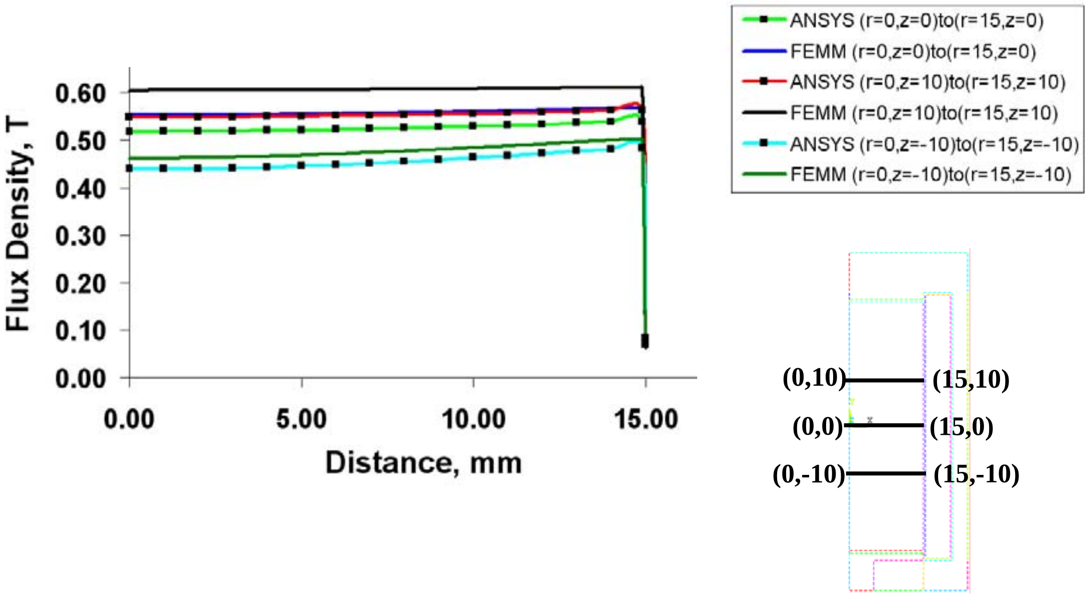

Figure 6.14: Flux density distribution along the indicated contour lines.

Table 6.2: Percentage error calculation for FEMM and ANSYS flux density output.

Contour lines (r$_1$,z$_1$) to (r$_2$,z$_2$)	**Average flux density, Tesla (T)**		**Percentage Error (%)**
	FEMM Results	**ANSYS Results**	
(0,10) to (15,10)	0.60752	0.55430	9.6%
(0,0) to (15,0)	0.55867	0.52626	6.15%
(0,-10) to (15,-10)	0.47762	0.45655	4.61%

Table 6.2 explains the percentage error between the FEMM and ANSYS average flux density output. Although the analysis showed the derived percentage errors in case of the average flux density output, considering mesh variance and element type difference between ANSYS and FEMM simulation environments, these simulation results could be treated as satisfactory.

6.6 Summary of chapter six

The purpose of this chapter was to verify the results obtained from FEMM with ANSYS. Eventually, according to the verified results, for a coil thickness of 5 mm with 22 AWG wire having 672 turns in 8 layers, possessed good prospect in actuating the desired amount of injector lift of 50 microns as the required magnetic field strength was achieved to cause the necessary amount of magnetostrictive strain. A concise and inclusive overview of the highlighted research process of this chapter is shown in figure 6.15.

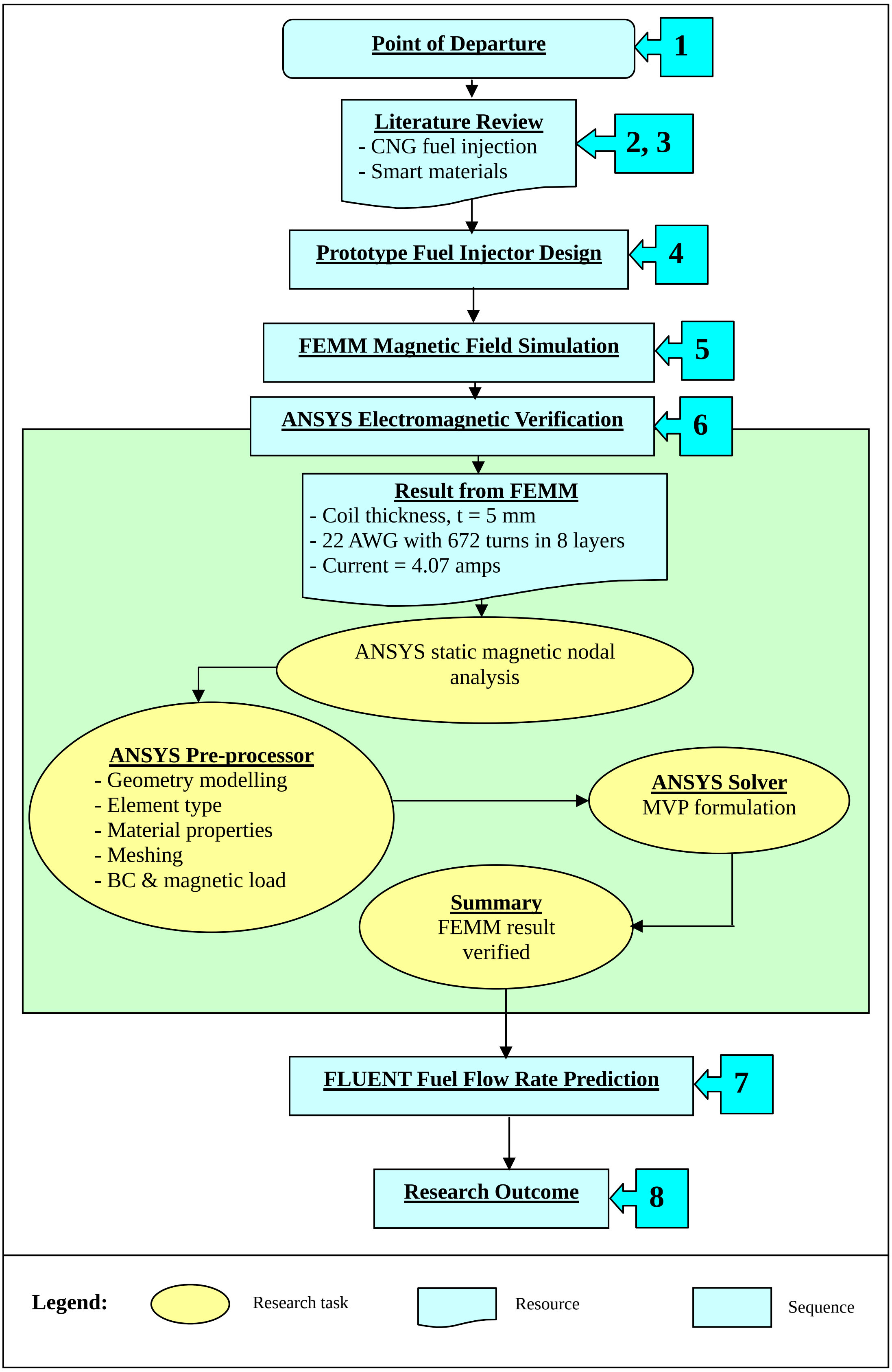

Figure 6.15: Summary of the research process in chapter six.

CHAPTER SEVEN

CNG FUEL INJECTOR MASS FLOW RATE PREDICTION BY FLUENT

7.1 Introduction

Computational fluid dynamics (CFD) is one of the branches of fluid mechanics that uses numerical methods and algorithms to solve and analyze problems that involve fluid flow utilizing computer software [124]. The advent of high speed and large memory computers has enabled users to obtain solutions to many flow problems such as compressible or incompressible, potential or non-potential, laminar or turbulent, multiphase and chemically reacting or non-reacting [125]. In case of the fluid flow problems, the governing equations such as *continuity* (conservation of mass), *the Navier-Stokes* (conservation of momentum), *species* and *energy* equations makeup a system of coupled non-linear partial differential equations [124,125]. However, due to the non-linearity of these partial differential equations, the analytical methods yield a small number of solutions. Furthermore, in order to obtain closed from analytical solutions, the partial differential equations need to be made linear or higher orders of linearity are neglected. Therefore, numerical methods need to be implemented in most engineering flow simulations where the non-linearity cannot be neglected. In this context, CFD replaces the partial differential equations governing the fluid flow with algebraic equations, which in turn can be solved with the assistance of a digital computer to get an approximate solution [126].

In CFD analysis, various discretization methods are implemented in order to transfer continuous models and equations into discrete counterparts. These are mainly, *finite difference method* (FDM), *finite volume method* (FVM), *finite element method* (FEM) and *boundary element method* (BEM) [127,128]. In this case, the software that was utilized in order to simulate the mass flow rate of CNG was *FLUENT Inc. version 6.2.16*, which employed the *FVM* method. This FVM method featured the benefit of allowing direct discretization in the physical space without the necessity of an explicit computation of metric co-efficient for arbitrary mesh configuration.

7.2 Turbulence models

In order to solve various fluid problems, a number of turbulence models are generally available. However, no single turbulence model is universally accepted as a superior model for all classes of problems. The choice of turbulence model generally depends on conditions such as the physics encompassed in the flow, the established practice for a specific class of problem, the level of accuracy required, the available computational resources and the amount of time available for the simulation. Furthermore, in order to make the most appropriate choice of model for a certain application, the user needs to understand the capabilities and limitations of the various models [127,129]. The different types of turbulence models are as follows [128-130]:

- Spalart-Allmaras model
- $k-\varepsilon$ models
    - Standard $k-\varepsilon$ model
    - Renormalization-group (RNG) $k-\varepsilon$ model
    - Realizable $k-\varepsilon$ model
- $k-\omega$ models
    - Standard $k-\omega$ model
    - Shear-stress transport (SST) $k-\omega$ model
- v^2-f model
- Reynolds stress model (RSM)
- Large eddy simulations (LES) model

In the present study, *the Standard* $k-\varepsilon$, *the Realizable* $k-\varepsilon$ and *RSM* models were utilized for the modeling of the CNG flow conduit to predict the mass flow rate of CNG for the injector lift of 50 microns.

7.2.1 The Standard $k-\varepsilon$ model

The standard $k-\varepsilon$ model is the simplest, fastest and most validated model for turbulence proposed by Launder and Spalding [131], which brings the solution of two separate transport equations and allows the turbulent velocity and length scales to be independently determined. It is a semi-empirical model based on model transport equations, as shown in Eq.7.1 and Eq.7.2, for the turbulence kinetic energy (*k*) and its dissipation rate (ε) [125].

$$\frac{\partial}{\partial t}(\rho k)+\frac{\partial}{\partial x_i}(\rho k \upsilon_i)=\frac{\partial}{\partial x_j}\left[\left(\mu+\frac{\mu_t}{\sigma_k}\right)\frac{\partial k}{\partial x_j}\right]+G_k+G_b-\rho\varepsilon-Y_M+S_k \qquad (7\text{-}1)$$

$$\frac{\partial}{\partial t}(\rho \varepsilon)+\frac{\partial}{\partial x_i}(\rho \varepsilon \upsilon_i)=\frac{\partial}{\partial x_j}\left[\left(\mu+\frac{\mu_t}{\sigma_\varepsilon}\right)\frac{\partial \varepsilon}{\partial x_j}\right]+C_{1\varepsilon}\frac{\varepsilon}{k}(G_k+C_{3\varepsilon}G_b)-C_{2\varepsilon}\rho\frac{\varepsilon^2}{k}+S_\varepsilon \qquad (7\text{-}2)$$

Where, G_k represents the generation of turbulence kinetic energy due to the mean velocity gradients, G_b is the generation of turbulence kinetic energy due to buoyancy and Y_M represents the contribution of the fluctuating dilatation in compressible turbulence to the overall dissipation rate. Furthermore, $C_{1\varepsilon}$, $C_{2\varepsilon}$ and $C_{3\varepsilon}$ are constants; S_k and S_ε are user-defined source terms and σ_k and σ_ε are the turbulent Prandtl number for *k* and ε respectively. Moreover, the turbulent or eddy viscosity, μ_t, is computed by combining *k* and ε as follows:

$$\mu_t=\rho C_\mu \frac{k^2}{\varepsilon} \qquad (7\text{-}3)$$

Where, C_μ is a constant. In the derivation of the $k-\varepsilon$ model, the assumption is that the flow is fully turbulent, and the effects of molecular viscosity are negligible. Therefore, standard $k-\varepsilon$ model is only valid for fully turbulent flows [125]. Two improved versions of the standard model are also available in FLUENT, namely the *realizable* $k-\varepsilon$ *model* and the *RNG* $k-\varepsilon$ *model*.

7.2.2 The Realizable $k-\varepsilon$ *model*

One of the more successful recent developments of the standard $k-\varepsilon$ model is the realizable $k-\varepsilon$ model developed by Shih et al. [132], which contains a new transport equation for the turbulent dissipation rate (ε). Furthermore, a critical coefficient of the model, C_μ, is expressed as a function of mean flow and turbulence properties, rather than assumed to be constant as in the standard model. The one limitation of the realizable $k - \varepsilon$ model is that it produces non-physical turbulent viscosities when the computational domain contains both rotating and stationary fluid zones. However, in case of spray models, this model provides satisfactory results [132].

7.2.3 The Reynolds Stress Model (RSM)

The RSM is the most classical model based on the initial work of Launder [131], which solves the transport equations for the Reynolds stresses together with an equation for the dissipation rate. Which eventually means that five additional transport equations are required in 2D flows and seven additional transport equations must be solved in case of 3D problems. The RSM model has a greater potential to represent turbulent flow phenomena more correctly than the two other models. However, it takes more computational time and is slow to converge [133].

7.3 Modeling of the CNG conduit

In the present research, a three dimensional replica of the CNG flow conduit was modeled in GAMBIT with the resultant injector lift of 50 Microns. For the CFD analysis, the following steps were implemented;

- Geometry creation
- Specifying zone types
- Meshing
- FLUENT Solver

7.3.1 Geometry creation

The 3D geometry of the CNG flow conduit was created in the Pro-Engineer Wildfire 3.0 which was then imported in Gambit version 2.4.6 as IGES format. The

Gambit allows geometry to be constructed or imported from alternative packages as different formats, such as ACIS, IGES, STEP, Parasolid, Catia and CAD with cleanup and modification capabilities.

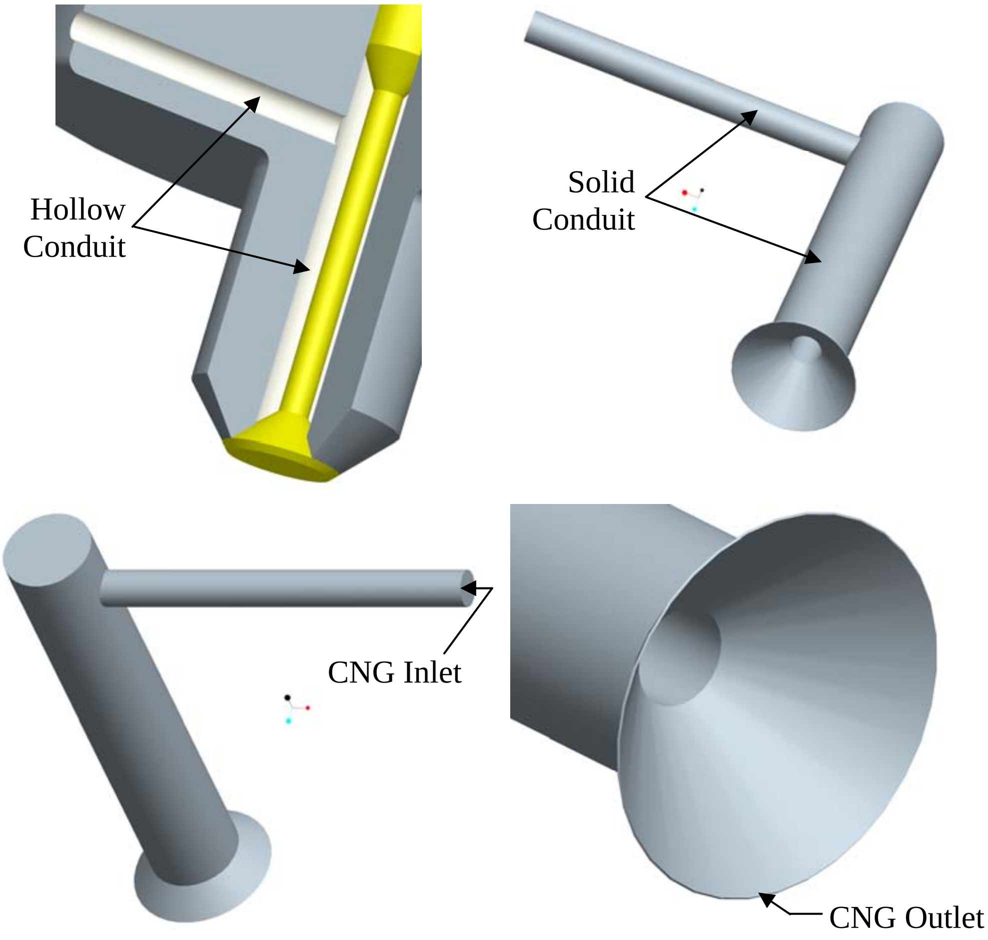

Figure 7.1: Pro-Engineer model of the CNG flow conduit.

The Pro-E 3D solid model of the CNG flow conduit was constructed from the inner hollow channel of the original injector assembly having the same dimensions, as shown in figure 7.1. The Pro-E part file was then imported as IGES format in GAMBIT, as shown in figure 7.2.

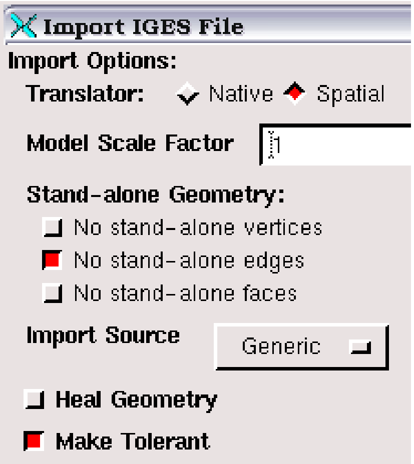

Import IGES File

Import Options:

Translator: ○ Native ● Spatial

Model Scale Factor 1

Stand-alone Geometry:

☐ No stand-alone vertices

☒ No stand-alone edges

☐ No stand-alone faces

Import Source Generic

☐ Heal Geometry

☒ Make Tolerant

Figure 7.2: Importing Pro-E model as IGES in GAMBIT

Eventually the model was cleaned by using *Virtual Cleanup* tool in GAMBIT. Furthermore, specifying the *No-stand alone edges* in the *Stand-alone Geometry* option enabled GAMBIT not to read in any edges that do not belong to faces or volumes. Fig.7.3 shows the imported geometry in GAMBIT graphical user interface.

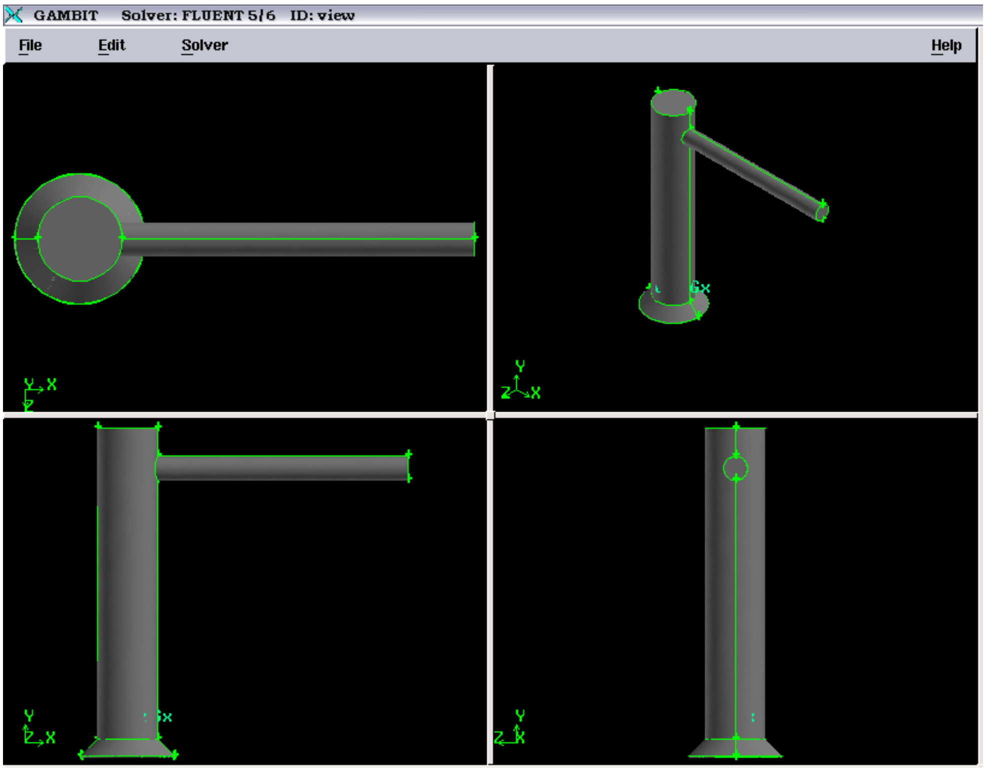

Figure 7.3: Imported CNG flow conduit model in GAMBIT.

In this research, *FLUENT 5/6* solver was selected in *GAMBIT version 2.4.6* for CFD analysis.

7.3.2 Specifying zone types

Zone-type specifications define the physical and operational characteristics of the model at its boundaries and within specific regions of its domain. There are two classes of zone-type specifications, namely *Boundary types* and *Continuum types*.

Where *Boundary-type* specifications defined the physical and operational characteristics of the model at those topological entities that represent model boundaries, *Continuum-type* specifications defined the physical characteristics of the model within specified regions of its domain. In this research, the CNG inlet and CNG outlet face regions were consecutively defined as *pressure inlet* and *pressure outlet* boundary types. Furthermore the rest of the faces were defined as *wall* boundary type and the volume was defined as the continuum type. In this regard, table 7.1 describes all the zone type specifications.

Table 7.1: Zone type specifications

Entity	Zone	Zone Type
face.8	Boundary	PRESSURE_INLET
face.1 face.17	Boundary	PRESSURE_OUTLET
face.(2-7) face (9-16)	Boundary	WALL
volume.1	Continuum	FLUID

7.3.3 Meshing

The meshing of the model geometry is an important and challenging task because the quality of the mesh affects the accuracy of the solution, the CPU time and memory requirements [134]. In this simulation, the *Mesh Volumes* command allowed to create the mesh for the entire volume of the model. When meshing the volume, GAMBIT created mesh nodes throughout the volume according to the specified meshing parameters. In order to specify the meshing scheme, two parameters were defined. These are *Elements* and *Type*.

The *Elements* parameter defined the shape of the elements that were used to mesh the volume. In this case, a *Tet/Hybrid* element type was chosen which specified that the mesh was composed primarily of tetrahedral mesh elements but may include hexahedral, pyramidal and wedge elements where appropriate. Subsequently, the *TGrid* type was associated with the *Tet/Hybrid* element type. The *TGrid* meshing scheme enabled GAMBIT to create an array of pyramidal mesh elements in proximity of the faces and furthermore creating tetrahedral elements throughout the rest of the volume. The meshed geometry is shown in figure 7.4.

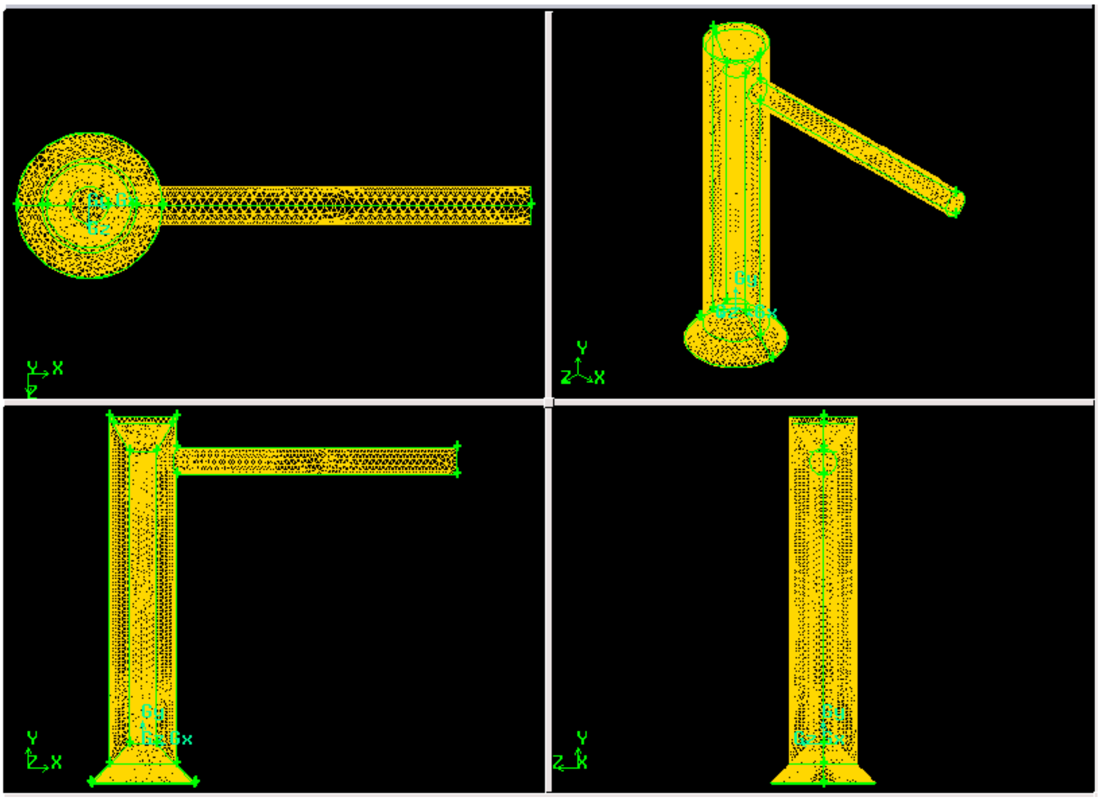

Figure 7.4: Meshed geometry in GAMBIT.

7.3.3.1 Mesh checking

It is important to check the quality of the resulting mesh, because properties such as skewness can greatly affect the accuracy and robustness of the CFD solution. GAMBIT provides several quality measures which can assess the quality of the mesh generated. Table 7.2 describes the resulting mesh characteristics based on corresponding quality types.

Table 7.2: GAMBIT mesh investigation

Quality type	**Highest active elements (%)**	**Range**	
		Lower limit	**Upper limit**
EquiAngle Skew	95.24%	0	0.75
EquiSize Skew	95.26%	0	0.75

An important factor regarding mesh checking was to ensure that the equi-angle skewness was not to exceed the value 0.75 [135]. As seen from table 7.2, a high percentage of the 3D elements were within this range. For an ideal mesh, in the statistical distribution of mesh elements represented by a histogram, the bars on the left of the histogram would be large and those on the right would be small. In this case, each element would possess a value of skewness between 0 and 1, where 0 would represent an ideal element. Fig. 7.5 depicts a sample display of equi-angle skewness quality.

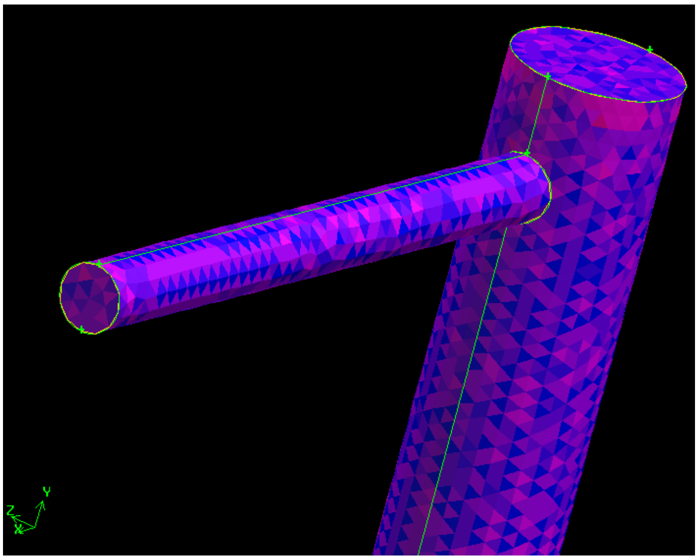

Figure 7.5: Equi-angle skewness quality.

7.3.4 FLUENT solver

The FLUENT 6.2.16 solver provides comprehensive modeling capabilities for a wide range of compressible and incompressible, laminar and turbulent fluid flow problems. Generally, two numerical methods are utilized to solve the fluid flow problems. These are namely, *coupled solver* and *segregated solver*. The coupled solver solves the governing equations of continuity, momentum and energy and species transport simultaneously. Where as, the segregated solver algorithm solves governing equations sequentially in order to obtain the solution [136]. Furthermore, each iteration follows the algorithm, shown in figure 7.6, and loops until the convergence criteria are met. In the present research, segregated solver was used which was fast and had less memory usage compared to coupled solver [136].

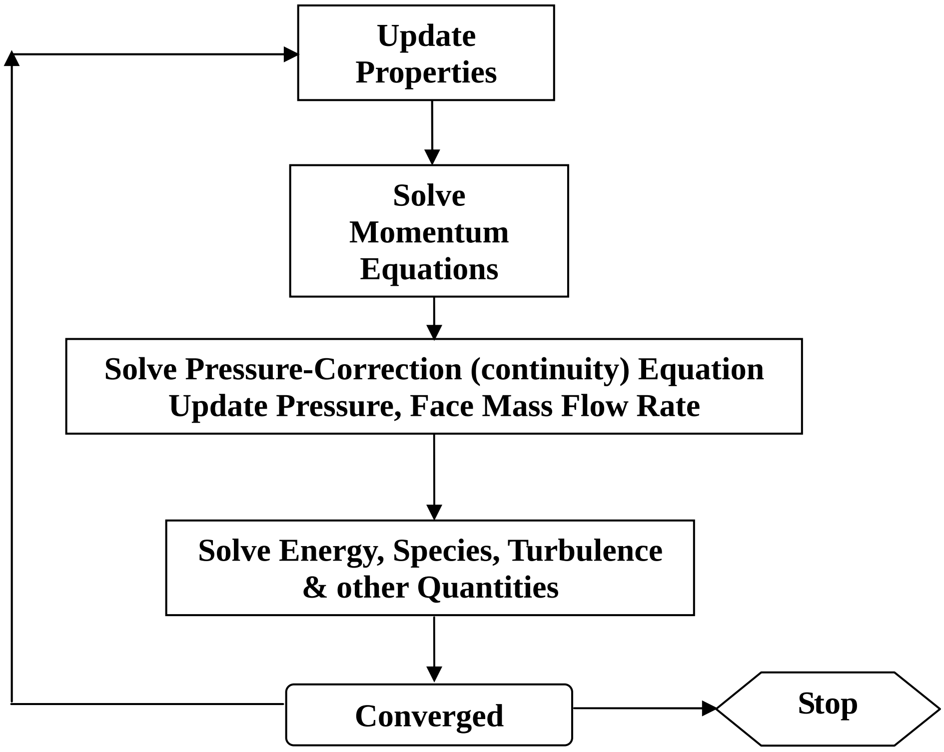

Figure 7.6: Overview of the segregated solution method [130].

7.4 FLUENT simulation results

The purpose of the CFD simulation was to determine the mass flow rate of CNG at the pressure outlet of the fuel injector. Subsequent to reading the **.mesh** file from GAMBIT, FLUENT created the **.case** and **.data** file decipherable for CFD analysis. The pressure at the inlet and the outlet of this flow conduit could then be varied depending on whether the injector to be utilized in case of either port injection or direct injection applications. In this research, in order to compare the resultant simulated mass flow rate with a standard intake port injected natural gas engine having identical fuel injection operating conditions, the following assumptions were made, as shown in table 7.3. As mentioned earlier, the FLUENT simulations were carried out for three different turbulent models, namely *the Standard $k-\varepsilon$, the Realizable $k-\varepsilon$* and *RSM* models.

Table 7.3: Assumptions for CFD analysis

Turbulence Model	Standard k–ε Model		
	Realizable k–ε Model		
	Reynolds Stress Model (RSM)		
Solver	Segregated	***Formulation***	Implicit
		Time	Steady
		Space	3D
		Velocity Formulation	Absolute
Boundary Conditions	***Pressure Inlet (psig)***	85	
	Pressure outlet (psig)	0	
	Wall	Stationary, No slip	
	Fluid	Methane (CH_4)	

Subsequently, figure 7.7 shows the static pressure distribution at the outlet region of the fuel injector for all three turbulent models.

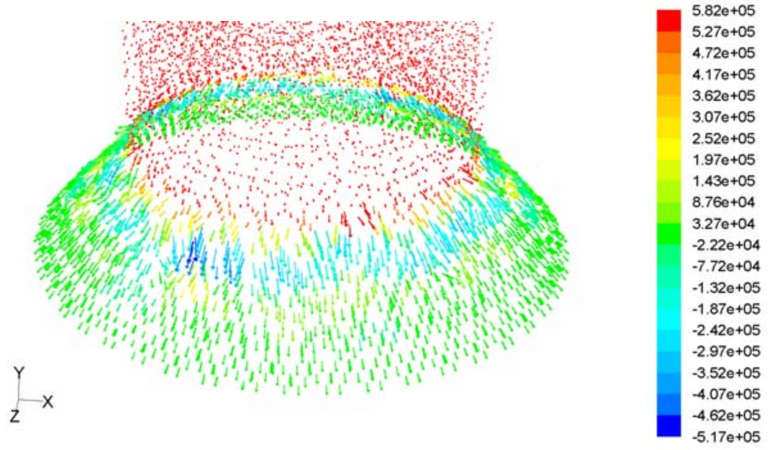

FLUENT 6.2 (3d, segregated, standard k-ε)

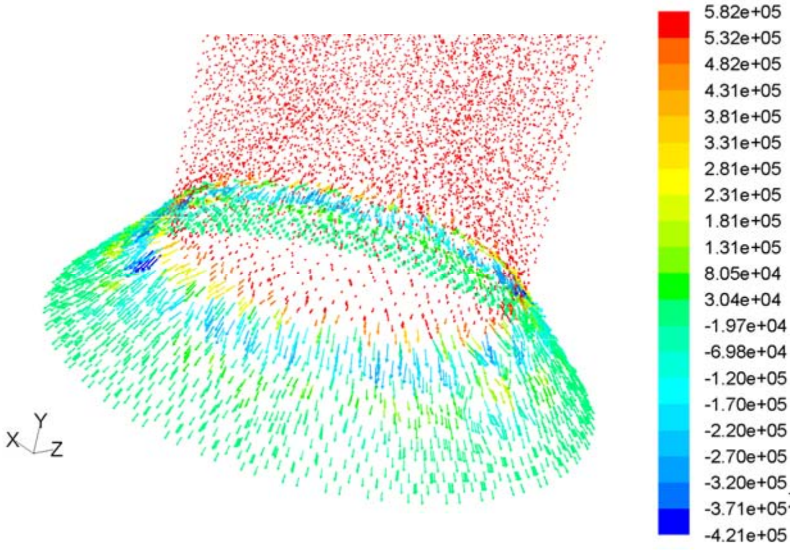

FLUENT 6.2 (3d, segregated, realizable k-ε)

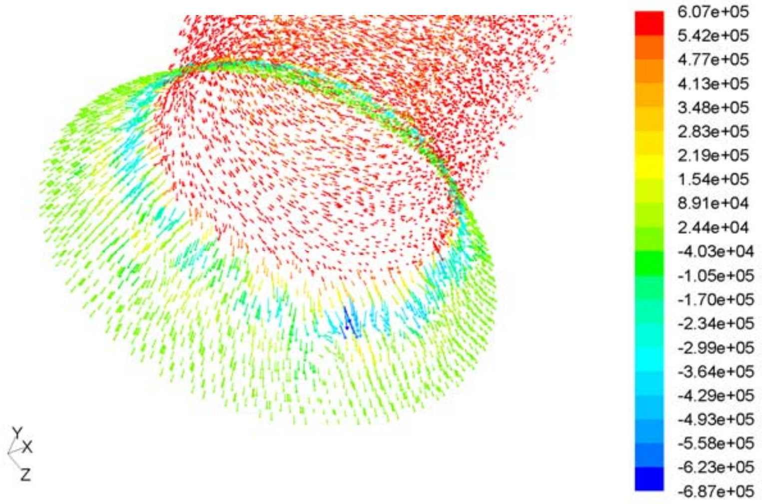

FLUENT 6.2 (3d, segregated, RSM)

Figure 7.7: Velocity vector colored by static pressure (Pa).

Eventually, the simulated mass flow rates at the pressure outlet of the fuel injector for the three turbulent models are depicted in the table 7.4. However, these values would depend on the inlet and outlet pressures of the fuel injector.

Table 7.4: Results of mass flow rates at the pressure outlet of the injector for P_{inlet}: 85 psig, P_{outlet}: 0 psig

Turbulent model	**Mass flow rate (kg/sec)**
Standard k-ε	0.00527488
Realizable k-ε	0.005214056
Reynolds Stress Model (RSM)	0.005530861

7.4.1 *Sample calculation of injector flow rate*

The *brake specific fuel consumption* (BSFC) of an automotive engine is a measure of engine efficiency expressed as the rate of fuel consumption divided by the power produced, which could be represented as,

$$B.S.F.C = \frac{Fuel\_Flow\_Rate}{Horsepower} \tag{7-4}$$

Considering the *duty cycle* of the fuel injector, the required injector static flow rate at 43.5 psig was [137]:

$$Injector\_Static\_Flow\_Rate_{43.5\,psig} = \frac{Horsepower \times B.S.F.C}{Injector\_Number \times Duty\_Cycle} \tag{7-5}$$

Again, in order to find the new fuel flow rate after the change of fuel pressure [137]:

$$New\_Flow\_Rate = \sqrt{\frac{New\_\Pr essure}{Old\_\Pr essure}} \times Old\_Fuel\_Rate \tag{7-6}$$

The assumptions for this calculation are shown in table 7.4.

Table 7.4: Assumptions for sample fuel flow calculation

Entity	**Value**	**Remark**
B.S.F.C	0.50	For naturally aspirated engine (0.45-0.50)
Duty Cycle	0.80	Accepted industry standard for safe operation
Crankshaft Horsepower (BHP)	250	Assumption
Number of Injectors	6	Assumption
Old Pressure (psig)	43.5	Functional pressure for Eq.7-5
New Pressure (psig)	85	Inlet pressure of fuel injector in CFD analysis

Now from Eq.7-5,

$$Injector\_Static\_Flow\_Rate_{43\cdot 5\,psig} = \frac{Horsepower \times B.S.F.C}{Injector\_Number \times Duty\_Cycle}$$

$$= \left(\frac{250 \times 0.5}{6 \times 0.8}\right) = 26.04\frac{lbs}{hr} = 273.42\frac{cc}{\min}$$

Again, from Eq.7.6,

$$New\_Flow\_Rate = \sqrt{\frac{New\_\Pr essure}{Old\_\Pr essure}} \times Old\_Fuel\_Rate$$

$$= \sqrt{\frac{85}{43.5}} \times 26.04 = 36.40\frac{lbs}{hr} = 382.20\frac{cc}{\min}$$

$$= 0.0045\frac{kg}{\sec}$$

Thus, a typical fuel injector operated under the same pressure conditions as in the case of the simulated prototype fuel injector would provide a mass flow rate of 0.0045 kg/sec. The percentage differences between the simulated and numerically derived fuel injector mass flow rates are depicted in table 7.5:

Table 7.5: Percentage difference between simulated and numerically derived mass flow rate

Turbulent model	**Simulated mass flow rate (kg/sec)**	**Numerically derived mass flow rate (kg/sec)**	**Percentage difference (%)**
Standard k-ε	0.00527488	0.0045	15.85%
Realizable k-ε	0.005214056		14.70%
Reynolds Stress Model (RSM)	0.005530861		20.55%

7.5 Summary of chapter seven

The purpose of the CFD analysis of the prototype fuel injector was to predict the mass flow rate of CNG at a specific operating condition. In this research, the analysis was performed to simulate the injection environment as if the injector was operated in case of an inlet port fuel injection system, where a standard port operated fuel injector inlet pressure was considered. Although the prototype injector model successfully operated under this simulated environment, the amount of mass flow rate at the pressure outlet was found to be slightly higher compared to the mathematically derived one. However, the mathematical model disregarded factors such as the cross-sectional area of injector outlet, turbulent flow and wall conditions. A concise and inclusive overview of the highlighted research process of this chapter is shown in figure 7.8.

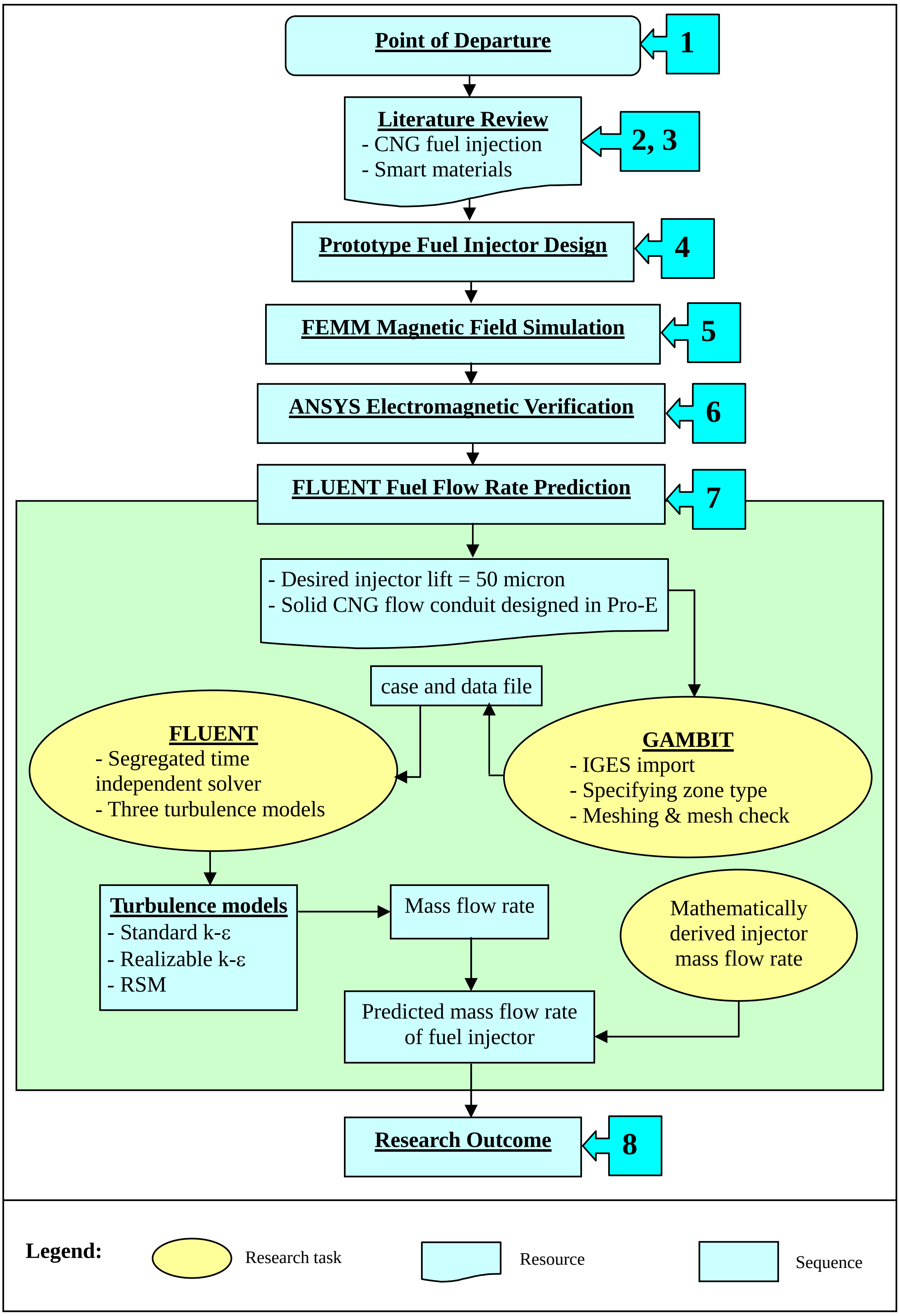

Figure 7.8: Summary of the research process in chapter seven.

CHAPTER EIGHT

CONCLUSIONS & RECOMMENDATIONS

8.1 Conclusions

In order to harness the exquisite properties of magnetostrictive material Terfenol-D in automotive CNG fuel injection actuation, a prototype CNG fuel injector was designed utilizing Terfenol-D as the actuator material. The research successfully demonstrated the prospect for implementing such materials in automotive fuel injection system through electromagnetic and computational fluid dynamics simulations. Although the present solenoid fuel injection systems suffer due to lack of actuator response time resulting in poor control of fuel injection at moderate to high speed levels, prospects for implementing magnetostrictive materials in these systems would still be less due to high cost involved in their production. Therefore, further attention should be given towards the monetary value regarding the production of these materials for more practical usage and also to achieve better fuel injection control, thereby minimizing the environmental pollution. The conclusions of the study could be summarized as follows:

a) Fuel injector design: A prototype CNG fuel injector assembly was designed using *Pro-Engineer*. The new design primarily included magnetostrictive material Terfenol-D as the actuator material, *1020 Steel* having soft magnetic properties as the injector housing material, *AWG* copper wire as the coil material and *316 Stainless Steel* having non-magnetic properties as the plunger material. While a *Coil spring* was designed to act as the closing spring having the task of bringing the needle valve to a closed position, a *Belleville spring* was designed as the prestress spring which had the task of providing axial prestress to the Terfenol-D shaft.

b) FEMM magnetic field simulation: After determining the required flux density of 0.55 Tesla for 1 KSI prestress to achieve the desired injector lift of 50 microns, a 2D cross-sectional geometry including the injector housing, coil, Terfenol-D shaft, and plunger, was modelled in *Finite Element Method Magnetics (FEMM)* for 2D axisymmetric magnetic simulation. The material models comprised the real linear or non-linear magnetic properties of the corresponding materials. The FEMM *magnetostatic series circuit* simulations were carried out with *22*, *24*, *28* and *30 AWG* coil wires and for injector coil thicknesses of *2*, *3*, *4* and *5* mm in order to evaluate the relationship between the different coil types and thicknesses against the achieved strain or injector lift. After analyzing the results, for the coil thickness of 5 mm, *22 AWG with 672 numbers of turns in 8 layers* showed superior prospect in actuating the desired amount of injector lift.

Furthermore, the FEMM *magnetostatic parallel circuit* simulations showed that higher parallel circuit current and lower parallel circuit voltage were required to achieve the desired flux density of 0.55 Tesla, while the coil power remained identical in both cases. Moreover, the FEMM *time-harmonic series circuit* simulations demonstrated that the flux density tended to increase suddenly for the same amount of current flow as the frequency was increased. However, as the frequency was increased further, the average value of flux density tended to decrease again.

c) ANSYS electromagnetic verification: The results obtained from FEMM simulation were verified by ANSYS electromagnetic simulation software. The analysis showed some slight variations in case of the average flux density output. However, these variations might be due to the mesh variance and element type difference between ANSYS and FEMM simulation environments.

d) Injector mass flow rate prediction by FLUENT: A three dimensional replica of the CNG flow conduit was modelled in *GAMBIT* with the resultant injector lift of 50 microns. The meshed conduit was then simulated in *FLUENT* using the *3D time independent segregated solver* with *standard* k-ε, *realizable* k-ε and *RSM* turbulent models to predict the mass flow rate of CNG to be injected, which showed successful injector function under these simulation environments. Eventually, the simulated flow rates were verified against mathematically derived static flow rate required for a standard automotive fuel injector, which showed that the amount of mass flow rate at the pressure outlet was slightly higher for the CFD models compared to the mathematically derived one. However, the mathematical model disregarded factors such as the cross-sectional area of injector outlet, turbulent flow and wall conditions.

8.2 Contributions of the thesis

The exquisite magnetostrictive actuating capabilities at micron scale and the incompetence of traditional solenoid fuel injection system motivated this research to contribute towards developing an automotive fuel injection system actuated by magnetostrictive material Terfenol-D. In this context, the electromagnetic and computational fluid dynamics analyses confirmed the possibility of developing such an actuator for fuel injection actuation. Consequently, the contributions of the thesis could be summarized as follows:

- The thesis contributed in designing a prototype automotive compressed natural gas fuel injector with the magnetostrictive material Terfenol-D as the actuator.

- The thesis contributed in establishing the capability of actuating such an injector by providing the coil-circuit parameters required to achieve a specific magnetostrictive strain resulting in an injector lift.

- The thesis contributed in establishing the capability of the prototype fuel injector in case of injecting compressed natural gas fuel at regular mass flow rates.

8.3 Recommendations for future work

The simulation results of this thesis have provided substantial groundwork for developing a CNG fuel injector actuated by magnetostrictive material Terfenol-D for practical implementation. Consequently, some recommendations for the future work regarding further development and construction of such an injector are as follows:

- Further investigation in verifying the produced magnetostrictive strain by constructing a test rig, where the strain could be measured directly by *laser displacement sensor*.

- Further investigation regarding the transient response of the prototype fuel injector.

- Further investigation regarding developing the fuel injector control circuit.

- Further investigation regarding the determination of spring forces required in case of both *closing* and *pre-stress* spring for practical implementation.

8.4 Summary of chapter eight

The summary of research outcome is shown in figure 8.1.

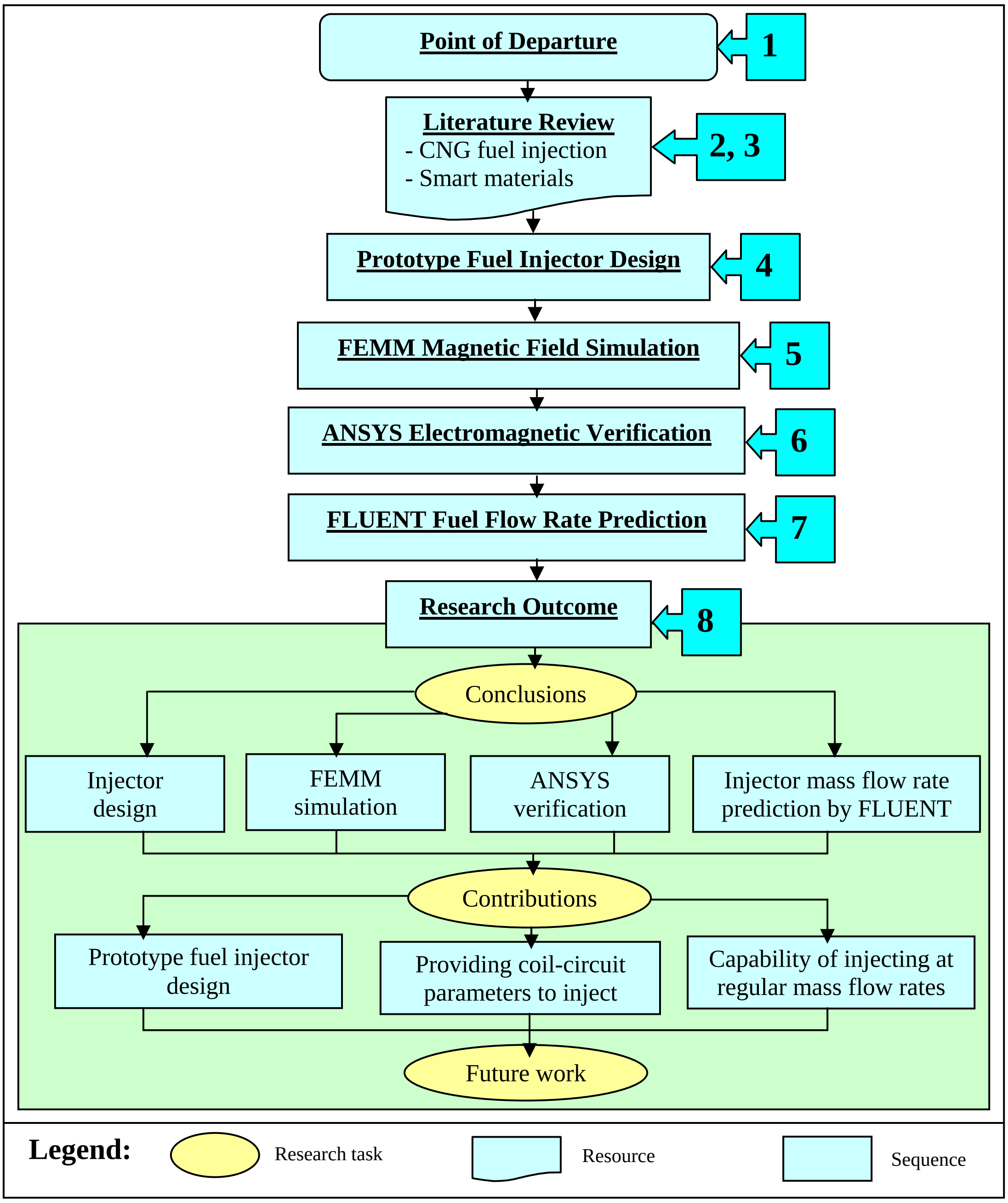

Figure 8.1: Summary of the research process in chapter eight.

REFERENCES

[1] Natural Gas Vehicle Technology, http://engva.org, accessed 10/07/06.

[2] J. G. Ingersoll, Natural Gas Vehicles: Economic, Environmental and Infrastructure Strategies, Fairmont Press, Inc., Georgia, USA, ISBN 0881732184, 1995.

[3] R. Schmer, The Motor Gasoline Industry: Past, Present & Future, DIANE Publishing, Darby, PA, USA, ISBN 0788187368, 2000.

[4] B. Onursal, S. P. Gautam, Vehicular Air Pollution: Experiences from Seven Latin American Urban Centers, World Bank Publications, Washington DC, USA, ISBN 0821340166, 1997.

[5] D. J. Podnar and J. T. Kubesh, Development of the Next Generation Medium-Duty Natural Gas Engine, Final Report-NREL/SR-540-27503, 2000.

[6] A. A. Quader, The Axially Stratified Charge Engine, SAE technical paper 820131, 1982.

[7] J. T. Kubesh, Development of a Throttleless Natural Gas Engine, Final Report-NREL/SR-540-31141, 2001.

[8] G. B. Cox, K. A. DelVecchio, W. J. Hays, J. D. Hiltner, R. Nagaraj, and C. Emmer, Development of a Direct-Injected Natural Gas Engine System for Heavy-Duty Vehicles, Final Report Phase II, NREL/SR-540-27501, 2000.

[9] S. Shiga, S. Ozone, H. T. C. Machacon, T. Karasawa, H. Nakamura, T. Ueda, N. Jingu, Z. Huang, M. Tsue and M. Kono, A Study of the Combustion and Emission Characteristics of Compressed-Natural-Gas Direct-Injection Stratified Combustion Using a Rapid-Compression-Machine, Combustion And Flame, 2002, Vol. 129, pp 1-10.

[10] H. T. C. Machacon, T. Yamagata, H. Sekita, K. Uchiyama, S. Shiga, T. Karasawa and H. Nakamura, JSAE Review 21, 2000, Vol. 4, p. 568.

[11] T. J. Callahan and J. T. Kubesh, Contribution of Prechamber Combustion to Engine CO and FC Emissions, Gas Machinery Conference, 1988.

[12] C. Y. Liu, R. Chen and S. F. Hussain, Development of Gaseous Injector for Propane and CNG, Part I, SAE technical paper 981355, 1998.

[13] G. Thomas, J. Goulding and C. Munteanu, Measurement, Approval and Verification of CNG Dispensers, NMSPU Project KT11 Report, www.nwml.gov.uk, accessed 10/07/06.

[14] P. Ouellette and A. Welch, Progresses in High Pressure Direct Injection (HPDI) of Natural Gas in Automotive Diesel Engines, Proc 8th Int Conf on NGV, 2002, pp. 1-11.

[15] T. Fukuda, T. Komoda, K. Furushima, M. Yanagihara and Y. Ito, Development of the Highly Efficient Gas Injection Diesel Engine with Glow Plug Ignition Assist for Cogeneration Systems, JSME-ASME International Conference on Power Engineering (ICOPE-93),1993, Vol. 1.

[16] A. K. Chan, Ignition Assist Systems for Direct-Injected, Diesel Cycle, Medium-Duty Alternative Fuel Engines, Final Report Phase I, NREL/SR-540-27502, 2000.

[17] C. A. Kroeger, A Neat Methanol Direct Injection Combustion System for Heavy-Duty Applications, SAE technical paper 861169, 1986.

[18] B. G. Richards, Methanol-Fueled Caterpillar 3406 Engine Experience in On-Highway Trucks, SAE technical paper 902160, 1990.

[19] B. G. Richards and M. L. Willi, Design and Development of a Direct Injected, Glow Plug Ignition Assisted, Natural Gas Engine, in M. R. Goyal (Ed.)Heavy Duty Engines: A Look at the Future, ASME 100375, 1994, Vol. 22, pp. 31-36.

[20] A. Vilmar, Hot Surface Assisted Compression Ignition in a Direct Injection Natural Gas Engine, Ph.D. Thesis, University of Trondheim, 1996.

[21] B. G. Richards, Development of a Direct Injection Natural Gas Engine System for Heavy Duty Vehicles, Phase 1 Final Report, NREL ZCI-6-15107-01, 1997.

[22] B. G. Richards, Direct Gas Injection with Glow Plug Ignition, GRI Final Report, 1997.

[23] M. L. Willi and B. G. Richards, Design and Development of a Direct Injected, Glow Plug Ignition Assisted, Natural Gas Engine, Journal of Engineering for Gas Turbines and power, 1995, Vol. 117, pp. 799-803.

[24] Development of a Direct-Injected Natural Gas Engine System for Heavy-Duty Vehicles-Final Report Phase 1, NREL/SR-540-27500, 2000, www.nrel.gov, accessed 12/05/06.

[25] O. Beppu, T. Fukuda, T. Komoda, S. Miyake and I. Tanaka, Service Experience of Mitsui Gas Injection Diesel Engines, Mitsui-MAN B&W 12K80MC-GI-S and Mitsui 8L42MB-G, Proceedings of the 22nd CIMAC International Congress on Combustion Engines, Copenhagen, May 18-21, 1998.

[26] M. Shioji, T. Ishiyama and M. Ikegami, Approaches to High Thermal Efficiency in High Compression Ratio Natural Gas Engines, Proceedings of the 7th International Conference and Exhibition on Natural Gas Vehicles, Yokohama, October 17-19, 2000.

[27] B. Bartunek and U. Hilger, Direct Induction of Natural Gas (DING): A Diesel-Derived Combustion System for Low Emissions and High Fuel Economy, SAE technical paper 2000-01-2827, 2000.

[28] Y. Takeda, K. Nakagome and K. Niimura, Emission Characteristics of Premixed Lean Diesel Combustion with Extremely Early Staged Fuel Injection, SAE technical paper 961163, 1996.

[29] H. Yokota, Y. Kudo, H. Nakazima, T. Kakegawa and T. Suzuki, A New Concept for Low Emission Diesel Combustion, SAE technical paper 970891, 1997.

[30] H. Yanagihara, Y. Sato and J. Mizuta, A Simultaneous Reduction of NOx and Soot in Diesel Engines under a New Combustion System (Uniform Bulky Combustion System-UNIBUS), 17th International Vienna Motor Symposium, 1996, pp. 303-314.

[31] H. Suzuki, N. Koike, H. Ishii and M. Odaka, Exhaust Purification of Diesel Engines by Homogeneous Charge with Compression Ignition, SAE technical paper 970313, 1997.

[32] Y. Daisho, T. Yaeo, T. Koseki, R. Kihara, and T. Saito, Combustion and Exhaust Gas Emissions in a Direct-Injection Diesel Engine Dual-Fueled with Natural Gas, SAE technical paper 950645, 1995.

[33] Y. Daisho, K. Takahashi, Y. Iwashiro, S. Nakayama, R. Kihara, and T. Saito, Controlling Combustion and Exhaust Gas Emissions in a Direct-Injection Diesel Engine Dual-Fueled with Natural Gas, SAE technical paper 952436, 1995.

[34] H. Ogawa, N. Miyamoto, C. Li, S. Nakazawa and K. Akao, Smokeless and Low NOx Combustion in a Dual-Fuel Diesel Engine with Induced Natural Gas as the Main Fuel, The Fifth International Symposium on Diagnostics and Modeling of Combustion in Internal Combustion Engines (COMODIA 2001), Nagoya, July 1-4, 2001.

[35] M. Ishida, N. Amimoto, T. Tagai and D. Sakaguchi, Effect of EGR and Preheating on Natural Gas Combustion Assisted with Gas-Oil in a Diesel Engine, The Fifth International Symposium on Diagnostics and Modeling of Combustion in Internal Combustion Engines (COMODIA 2001), Nagoya, July 1-4, 2001.

[36] M. U. Aslam, H. H. Masjuki, M. A. Kalam, H. Abdesselam, T. M. I. Mahlia and M. A. Amalina, An Experimental Investigation of CNG as an Alternative Fuel for a Retrofitted Gasoline Vehicle, Fuel, 2006, Vol. 85, pp. 717-724.

[37] M. A. Kalam, H. H. Masjuki, and M. A. Maleque, Gasoline Engine Operated on Compressed Natural Gas, Proceedings of Advanced Malaysian Energy Research (Am), Malaysia, 2001, pp. 307-316.

[38] N. J. Beck, R. L. Barkhimer, W. P. Johnson, H. C. Wong and K. Gebert, Evolution of Heavy Duty Gas Engines -Stoichiometric, Carbureted and Spark Ignited to Lean Burn, Fuel Injected and Micro-Pilot, SAE technical paper 972665:1, 1997.

[39] M. U. Aslam, H. H. Masjuki, M. A. Maleque and M. A. Kalam, Prospect of CNG as an Automotive Fuel Instead of Gasoline, Proceedings of the seventh Asia-pacific international symposium on combustion and energy utilization, Hong Kong, Paper No., C1-170 (2004) 1.

[40] C. Bach, C. Lammle, R. Bill, P. Soltic, D. Dyntar, P. Janner, et al, SAE Tech Paper 0645 (01), pp. 227–229.

[41] A. L. Jones and R. L. Evans, Journal of Engineering for Gas Turbine Power, 1985, Vol. 107, p. 908.

[42] R. L. Evans and J. Blaszczyk, A Comparative Study of the Performance and Exhaust Emissions of a Spark Ignited Engine Fuelled by Natural Gas and Gasoline, Proceedings of the Institution of Mechanical Engineers, Part D: Journal of Automobile Engineering, 1997, Vol. 211, Issue 1, pp. 39-47.

[43] H. A. Hamid and A. S. Ahmed, Development of Monofuelled Natural Gas Vehicles: A Malaysian Experience, Malaysia: Special Project of Petronas Research, 2002. p.10.

[44] Y. Goto and Y. Sato, NOx Reduction on Direct Injection Natural Gas Engines, SAE technical paper 1999-01-3608, 1999.

[45] Y. Goto and Y. Sato, Combustion Chamber Improvement and Emissions Characteristics in a Direct Injection Natural Gas Engine by Throttling and Exhaust Gas Recirculation, SAE technical paper 2001-01-0737, 2001.

[46] C. Arcoumanis, H. Flora, J. W. Kim and H. M. Xu, A Direct Injection Natural Gas Engine for Light-Duty Applications, http://www.hyphen.info, accessed 13/04/06.

[47] A. D. Toro, M. Frailey, F. Lynch, S. Munshi and S. Wayne, Development and Demonstration of Hydrogen and Compressed Natural Gas (H/CNG) Blend Transit Buses, Technical Report, NREL/TP-540-38707, 2005.

[48] R. F. Stebar and F. B. Parks, Emissions Control with Lean Operation Using Hydrogen-Supplemented Fuel, General Motors Research Publications No. 1537, 1974.

[49] J. Houseman and F. W. Hoehn, A Two-Charge Engine Concept: Hydrogen Enrichment, SAE technical paper 741169, 1974.

[50] Technical Comparison Between Hythane®, CNG and Gasoline Fueled Vehicles, Report by Energy Task Force of the Urban Consortium, City and County of Denver, Alternative Fuels Unit, 1992.

[51] J. Fulton, F. Lynch, B. Wilson, J. Schneider, and J. Yost, A Study of Hydrogen/Methane Combustion in Spark Ignition Engine, Proceedings of the Annual Automotive Technology Development Contractors' Coordination Meeting, Dearborn, Michigan, 1993, p. 278.

[52] F. Lynch and J. Fulton, Advanced Hydrogen/Methane Utilization Technology Demonstration- Final Report, NREL/TP-425-6357, 1994.

[53] V. Raman, J. Hansel, J. Fulton, F. Lynch, and D. Bruderly, Hythane®- An Ultraclean Transportation Fuel, 10th World Hydrogen Energy Conference, Cocoa Beach, Florida, 1994.

[54] E. Wang and H.C. Watson, Direct Injection Compressed Natural Gas Combustion and Visualisation, SAE technical paper 2000-01-1838, 2000.

[55] A. Das, Optimisation of a natural gas spark ignition engine, PhD thesis, The University of Melbourne, 1995.

[56] G. Lumsden, H.C. Watson, Optimum control of a SI engine with a $\lambda = 5$ capability, SAE technical paper 950689, 1995.

[57] J. Lawrence, Hydrocarbon Emissions from a HAJI Equipped Ultra Lean Burn Engine, PhD thesis, The University of Melbourne, 1999.

[58] A. G. Olabi and A. Grunwald, Design and Application of Magneto-rheological Fluid, Materials and Design, 2007, Vol. 28, pp. 2658–2664.

[59] R. E. Newnham, Piezoelectric Sensors and Actuators: Smart Materials, Proceedings of the IEEE Frequency Control Symposium, 1992, pp. 513-524.

[60] A. E. Clark, Ferromagnetic Materials, Vol. 1, E. P. Wolfhart (Ed.), Amsterdam, North-Holland, p. 531.

[61] Magnetostriction and Magnetostrictive Materials, http://aml.seas.ucla.edu, accessed 23/04/07.

[62] Magnetostrictive Materials Background, http://aml.seas.ucla.edu, accessed 20/05/07.

[63] J. W. Xie, D. Fort, Y. J. Bi and J. S. Abell, Microstructure and Magnetostrictive Properties of Tb-Dy-Fe (Al) Alloys, Journal of Applied Physics, 2000, Vol. 9, p. 87.

[64] L. Daniel, O. Hubert, and R. Billardon, Homogenisation of Magneto-elastic Behaviour: From the Grain to the Macro Scale, Computational and Applied Mathematics, 2004, Vol. 23, Issue 2-3, pp. 285-308.

[65] R. C. Smith, Smart Material Systems: Model Development, SIAM, pp. 15-16, 2005.

[66] N. B. Ekreem, A. G. Olabi, T. Prescott, A. Rafferty and M. S. J. Hashmi, An Overview of Magnetostriction, Its Use and Methods to Measure These Properties, Journal of Materials Processing Technology, 2007, Vol. 191, pp. 96-101.

[67] M. J. Dapino, Magnetostrictive Materials: Their Use in Smart Structure Applications, in: J.A. Harvey (Ed.), Encyclopedia of Smart Materials, John Wiley & Sons, Inc., New York, USA, 2000, pp. 600-620.

[68] R. Piercy, The Changing Shape of Magnetostriction, Physics Education, 1997, Vol. 32, pp. 160-163.

[69] M. Knobel, J. C. Cezar, H. C. N. Tolentino, A. R. B. de Castro, R. Piccin and K. R. Pirota, Circular Magnetic Dichroism in $Fe_{78-x}Ni_xSi_8B_{14}$ ($15 \leq x \leq 58$) Ferromagnetic Amorphous Ribbons, Journal of Magnetism and Magnetic Materials, 2001, Vol. 233, pp. 78-83.

[70] R. O’Handley, in: F. Luborsky (Ed.), Amorphous Metallic Alloys, Butterworths, London, 1981, p. 257.

[71] A. G. Olabi, and A. Grunwald, Design and Application of Magnetostrictive Materials, Materials & Design, 2008, Vol. 29, Issue 2, pp. 469-483.

[72] J. L. Pons, Emerging Actuator Technologies: A Micromechatronic Approach, John Wiley and Sons, Inc., New York, USA, 2005.

[73] S. Diamond and D. Johnson, Heavy Vehicle Propulsion Materials Draft Multi Year Program Plan, Revision 7, Department of Energy (DOE), USA, 2000.

[74] Cost-effective Smart Materials for Diesel Engine Applications, www.ornl.gov, accessed 20/03/07.

[75] P.R. Czimmek, Electronic fuel injector actuated by magnetostrictive transduction, US Patent Issued on April 2, 2002.

[76] Fuel Injection, http://en.wikipedia.org/wiki/Fuel_injection, accessed 14/09/08.

[77] M. J. Dapino, R. C. Smith, A. B. Flatau, An Active and Structural Strain Model for Magnetostrictive Transducers, SPIE Symposium on Smart Structures and Materials, Paper 3329-24, 1998.

[78] A. Grunwald and A. G. Olabi, Design of a Magnetostrictive (MS) Actuator, Sensors and Actuators: A Physical, 2008, Vol. 144, Issue 1, pp. 161-175.

[79] F. Claeyssen, N. Lhermet, R. Le Letty, P. Bouchiloux, Actuators, Transducers and Motors Based on Giant Magnetostrictive Materials, Journal of Alloys and Component, 1997, Vol. 258, pp. 61-73.

[80] M. G. Aston, A. G. I. Jenner, W. J. Metheringham, K. Prajapati, Controlled High Power Actuation Utilizing Terfenol-D, Journal of Alloys and Compounds, 1997, Vol. 258, pp. 97-100.

[81] H. Janocha (Ed.), Actuators, Springer Verlag, Germany, ISBN 3-540-61564-4, 2004.

[82] Y. Yamamoto, H. Eda, J. Shimizu. Application of Giant Magnetostrictive Materials to Positioning Actuators, IEEE/ASME International Conference on Advanced Mechatronics, Altanta USA, 1999, pp. 215-220.

[83] Y. Yamamoto, T. Makino, H. Matsui, Micro Positioning and Actuation Devices Using Giant Magnetostriction Materials, IEEE International Conference on Robotics and Automation, San Francisco CA, USA, 2000, pp. 3635-3640.

[84] M. J. Dapino, On Magnetostrictive Materials and Their Use in Smart Material Transducer, Structural Engineering and Mechanics Journal, 2002, pp. 1-28.

[85] Terfenol-D Data Sheet, ETREMA Products Inc., www.etrema.com, accessed 15/08/07.

[86] F. Claeyssen and C. Recherche, Design and Construction of a New Resonant Magnetostrictive Motor, IEEE Transactions of Magnetics, 1996, Vol. 32, Issue 5, pp. 4749-4751.

[87] R. D. Greenough, M. P. Schulze and D. Pollard, Non-destructive testing of Terfenol-D, Journal of Alloys and Component, 1997, Vol. 258, pp. 118-122.

[88] G. Engdahl (Ed.), Handbook of Giant Magnetostrictive Materials, Royal Institute of Technology, Stockholm, Sweden, ISBN 012238640, 2000.

[89] M.J. Dapino, F.T. Calkins, B. Flatau and D.L. Hall, Measured Terfenol-D Material Properties Under Varied Applied Magnetic Field Levels, SPIE Symposium on Smart Structures and Materials, paper 2717-66, 1996.

[90] A. G. I. Jenner, R. J. E. Smith, R. D. Greenough and A. J. Wilkinson, Actuation and Transduction by Giant Magnetostrictive Alloys, Mechatronics, 2000, Vol. 10, pp. 457-466.

[91] R. D. Greenough, M. P. Schulze, A. G. L. Jenner and A. J. Wilkinson, Actuation with Terfenol-D, IEEE Transactions on Magnetics, 1991, Vol. 27, Issue 6, pp. 5346-5348.

[92] G. Engdahl and F. Stillesjö, Estimation of the Intrinsic Magnetomechanical Response of Magnetostrictive Actuators by Dynamic Simulations, Journal of Alloys and Component, 1997, Vol. 258, pp. 79-82.

[93] F. Claeyssen, D. Colombani, C. Recherche, A. Tessereau, B. Ducros, E. Degreane, Giant Dynamic Magnetostrain in Rare Earth-iron Magnetostrictive Materials, IEEE Transaction on Magnetics, 1991, Vol. 27, Issue 6, pp 5343-5345.

[94] W. D. Callister, Materials Science and Engineering: An Introduction, 3rd Ed., John Wiley and Sons, Inc., New York, 1994.

[95] D. R. Askeland, The Science and Engineering of Materials, 3rd Ed., Chapman and Hall, London, 1996.

[96] HyperPhysics, Relative Permeability, http://hyperphysics.phy-astr.gsu.edu, accessed 02/06/08.

[97] HyperPhysics, Hysteresis Loop, http://hyperphysics.phy-astr.gsu.edu, accessed 02/06/08.

[98] D. L. Hall and A. B. Flatau, Broadband Performance of a Magnetostrictive Shaker, Journal of Intelligent Material Systems and Structures, 1995, Vol. 6, pp. 109-116.

[99] D. Davino, C. Visone, C. Natale, S. Pirozzi, Rate-dependent Losses Modeling for Magnetostrictive Actuators, Journal of Magnetism and Magnetic Materials, 2004, Vols. 272-276, pp. 1781-1782.

[100] J. Schäfer and H. Janocha, Compensation of Hysteresis in Solid State Actuators, Sensors and Actuators A, 1995, Vol. 49, pp. 97-102.

[101] F. Claeyssen In: H. Janocha, editor. Adaptronics and smart structures. Germany: Springer Verlag; 1999, ISBN 3-540-61484-2. pp. 124–143.

[102] J. D. Snodgrass and O. D. McMasters, Optimized Terfenol-D Manufacturing Processes, Journal of Alloys and Compounds, 1997, Vol. 258, Issue 1, pp. 24-29.

[103] New Production Process, Optimized PZT Ceramics, www.piceramic.com, accessed 30/06/07.

[104] A. Heinzmann, E. Hennig, B. Kolle, D. Kopsch, S. Richter, H. Schwotzer and E. Wehrsdorfer, Advances in Piezoelectric Multilayer Actuator Technology, www.piceramic.com, accessed 15/12/07.

[105] C. R. Bowen, R. Stevens, L. J. Nelson, A. C. Dent, A. C. Dent, G. Dolman, B. Su, T. W. Button, M. G. Cain and M. Stewart, Manufacture and Characterization of High Activity Piezoelectric Fibres, Smart Materials and Structures, 2006, Vol. 15, Issue 2, pp. 295-301.

[106] Measurement and Modelling of Non-linearity in Piezoelectric Materials, www.npl.co.uk, accessed 15/05/07.

[107] D. Davino, C. Natale, S. Pirozzi and C. Visone, A Fast Compensation Algorithm for Real-time Control of Magnetostrictive Actuators, Journal of Magnetism and Magnetic Materials, 2005, Vols. 290–291, pp. 1351–1354.

[108] I. D. Mayergoyz, Mathematical Models of Hysteresis, Springer, Berlin, 1991.

[109] G. Bertotti, Dynamic generalization of the scalar Preisach model of hysteresis, IEEE Transactions on Magnetics, 1992, Vol. 28, Issue 5, Part 2, pp. 2599-2601.

[110] D. Davino, C. Natale, S. Pirozzi and C. Visone, Phenomenological Dynamic Model of a Magnetostrictive Actuator, Physica B: Condensed Matter, 2004 Vol. 343, Issues 1-4, pp. 112-116.

[111] A. Cavallo, C. Natale, C. Pirozzi and C. Visone, Effects of Hysteresis Compensation in Feedback Control Systems, IEEE Transactions on Magnetics, 2003, Vol. 39, Issue 3, Part 1, pp. 1389-1392.

[112] M. A. Krasnoselskii, A. V. Pokrovskii, Systems with Hysteresis, Springer, Berlin, 1989.

[113] P. Krejci, Hysteresis and Periodic Solutions of Semilinear and Quasilinear Wave Equations, Mathematische Zeitschrift, 1986, Vol. 193, pp. 247-264.

[114] C. Visone and M. Mårten Sjöström, Exact Invertible Hysteresis Models Based on Play Operators, Physica B: Condensed Matter, 2004, Vol. 343, Issues 1-4, pp. 148-152.

[115] R. Fresa, C. Serpico and C. Visone, Numerical Analysis of Magnetic Field Diffusion in Ferromagnetic Laminations by Minimization of Constitutive Error, Journal of Applied Physics, 2000, Vol. 87, Issue 9, pp. 6546-6548.

[116] Cost-Effective Smart Materials for Diesel Engine Applications, Available from: www.ntrc.gov (16.05.07).

[117] N. Hakim, Y. Kalish, S. Li and H. Jiang, Smart Materials for Fuel Injection Actuation, DEER Workshop, 2000.

[118] Metal Suppliers Online, Carbon Steel 1020, www.suppliersonline.com, accessed 27/06/08.

[119] AISI 1020, Carbon Steel AISI 1020, www.efunda.com, accessed 27/06/08.

[120] Stainless Steel - Grade 316 - Properties, Fabrication and Applications, www.azom.com, accessed 27/06/08.

[121] Finite Element Method Magnetics, http://femm.foster-miller.net, accessed 10/08/07.

[122] User’s Manual, Finite Element Method Magnetics, Version 4.2, http://femm.foster-miller.net.

[123] Release 11.0 Documentation for ANSYS, ANSYS 11.0 SP1.

[124] I. H. Shames, Mechanics of fluid, McGraw Hill, Singapore, 3rd ed, ISBN 0-07-05638-X, 1992.

[125] FLUENT Inc, Introductory FLUENT Notes, FLUENT version 6.2.16.

[126] C. Hirsch, Numerical Computational of Internal and External Flows, Vols. 1-2, John Wiley & Sons, U.K, ISBN 0471 923516, 1992.

[127] K. A. Hoffmann and S. T. Chiang, Computational Fluid Dynamics for Engineers, Vol. 3, 4th ed, Engineering Education Systems, 2000.

[128] J. D. Anderson, Computational Fluid Dynamics: The Basics with Applications, McGraw Hill, ISBN 0-07-001685-2, 1995.

[129] A. A. Mostafa and S. E. Elghobashi, A Two-equation Turbulence Model for Jet Flows Laden with Vaporizing Droplets, International Journal of Multiphase Flow, 1985, Vol. 11, Issue 4, pp. 515-533.

[130] Fluent Inc. FLUENT 6.2 User Guide, Vol. 1-6, Published by FLUENT Inc., New Hampshire, USA, 2004.

[131] B. E. Launder and D. B. Spalding, The Numerical Computation of Turbulent Flows, Computer Methods in Applied Mechanics and Engineering, 1974, Vol. 3, pp. 269-289.

[132] T. H. Shih, W. W. Liou, A. Shabbir, Z. Yang and J. Zhu, A New k- ε Eddy Viscosity Model for High Reynolds Number Turbulent Flows, Computers & Fluids, 1995, Vol. 24, Issue 3, pp.227-238.

[133] D. C. Wilcox, Turbulence Modeling for CFD, 2nd Edition, DCW Industries, ISBN 192872910X, 1994.

[134] P. L. George, Automatic Mesh Generation and Finite Element Computation, Handbook of Numerical Analysis, Elsevier, 1996.

[135] M. C. Bastarrica and N. H. Kahler, Designing a Product Family of Meshing Tools, Advances in Engineering Software, 2006, Vol. 37, Issue 1, pp. 1-10.

[136] J. H. Ferziger and M. Peric, Computational Methods for Fluid Dynamics, 3rd ed, Springer, New York, ISBN-3-540-42074-6, 2002.

[137] Technical Notes, RC Fuel Injection, www.rceng.com, accessed 13/04/08.

APPENDICES

APPENDIX A

PUBLICATIONS

This work has been disseminated through the following publications.

Journal Papers:

- **H. A. Chowdhury**, S. A. Mazlan and A. G. Olabi, Implementation of Magnetostrictive Material Terfenol-D in CNG Fuel Injection Actuation, Advanced Materials Research, Vols. 47-50, 2008, pp. 630-633.
- **H. A. Chowdhury,** S. A. Mazlan and A. G. Olabi, A Simulation Study of Magnetostrictive Material Terfenol-D in Automotive CNG Fuel Injection Actuation, *Solid State Phenomenon*. (under review)
- **H. A. Chowdhury,** S. A. Mazlan and A. G. Olabi, A Comparative Magnetic Simulation Study between ANSYS and FEMM for the Implementation of Magnetostrictive Material Terfenol-D in CNG Fuel Injection Actuation, *Journal of Magnetism and Magnetic Materials*. (under review)

Conferences:

- **H. A. Chowdhury** and A. G. Olabi, A Finite Element Approach for the Implementation of Magnetostrictive Material Terfenol-D in CNG Fuel Injection Actuation, presented at the *ASME 2008 International Design Engineering Technical Conferences & Computers and Information in Engineering Conference IDETC/CIE 2008*, Brooklyn, New York, USA, August 3-6, 2008.
- **H. A. Chowdhury**, S. A. Mazlan and A. G. Olabi, Implementation of Magnetostrictive Material Terfenol-D in CNG Fuel Injection Actuation, presented at the *International Conference on Multifunctional Materials and Structures*, Hong Kong, China, 28-31 July, 2008.
- **H. A. Chowdhury**, S. A. Mazlan and A. G. Olabi, A Comparative Magnetic Simulation Study between ANSYS and FEMM for the Implementation of Magnetostrictive Material Terfenol-D in CNG Fuel Injection Actuation, presented at the *Joint European Magnetic Symposia*, Dublin, Ireland, September 14-19, 2008.
- **H. A. Chowdhury**, S. A. Mazlan and A. G. Olabi, A Simulation Study of Magnetostrictive Material Terfenol-D in Automotive CNG Fuel Injection Actuation, presented at *the 2008 European Materials Research Society (E-MRS) Fall Meeting*, Warsaw, Poland, September 15-19, 2008.
- **H. A. Chowdhury** and A. G. Olabi, Recent CNG Developments and Its Implications For Heavy-Duty Vehicles, in *Proceedings of The International Conference on Vehicles Alternative Fuel Systems & Environmental Protection*, 2006, pp. 75-89.

APPENDIX B

CAD DRAWINGS

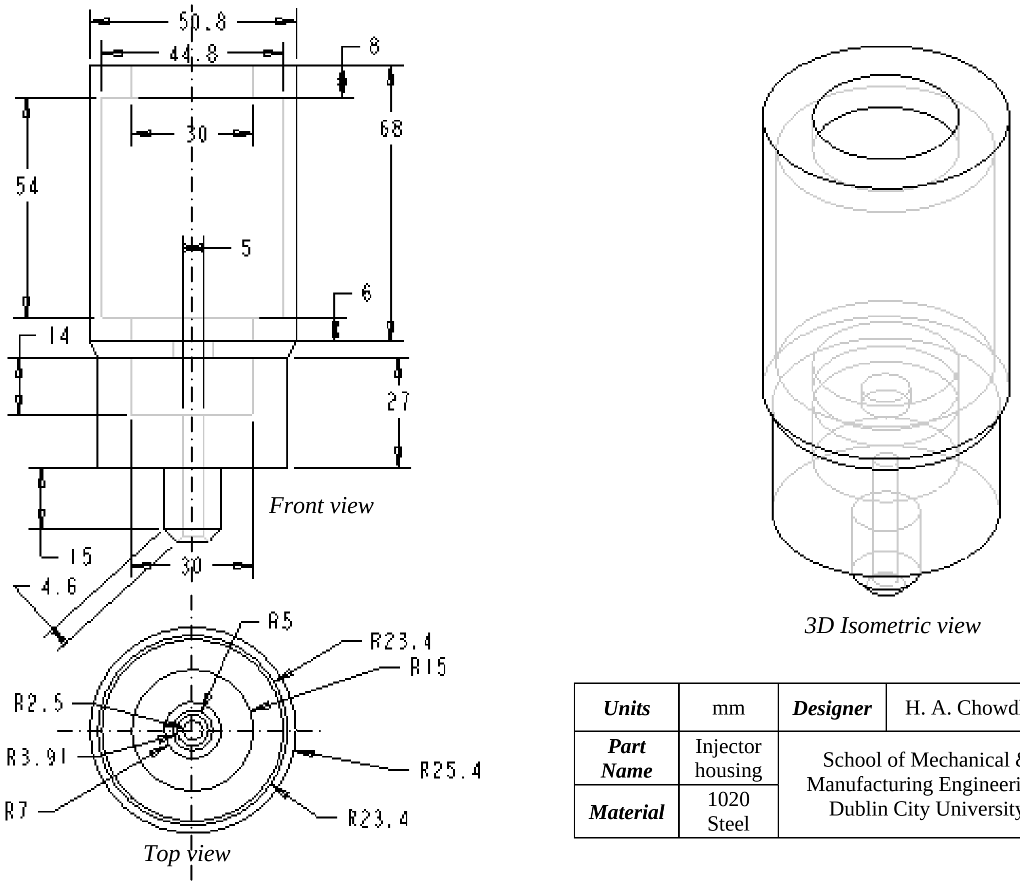

Units	mm	***Designer***	H. A. Chowdhury
Part Name	Injector housing	School of Mechanical & Manufacturing Engineering, Dublin City University	
Material	1020 Steel		

Figure B1: Injector housing.

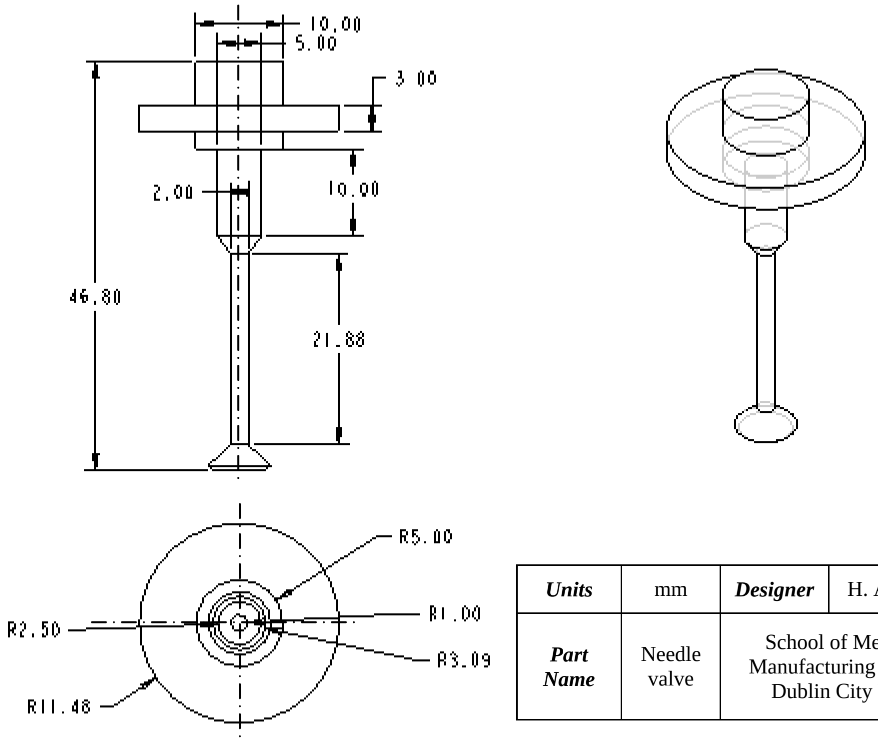

Units	mm	***Designer***	H. A. Chowdhury
Part Name	Needle valve	School of Mechanical & Manufacturing Engineering, Dublin City University	

Figure B2: Needle valve.

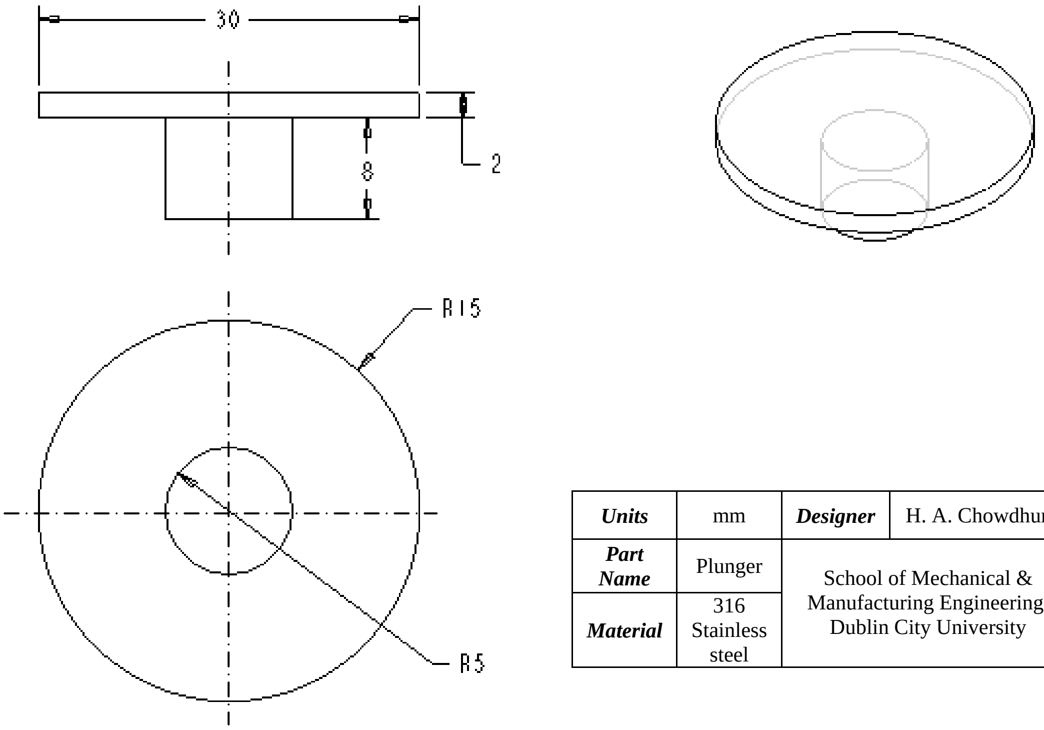

Units	mm	***Designer***	H. A. Chowdhury
Part Name	Plunger	School of Mechanical & Manufacturing Engineering, Dublin City University	
Material	316 Stainless steel		

Figure B3: Plunger

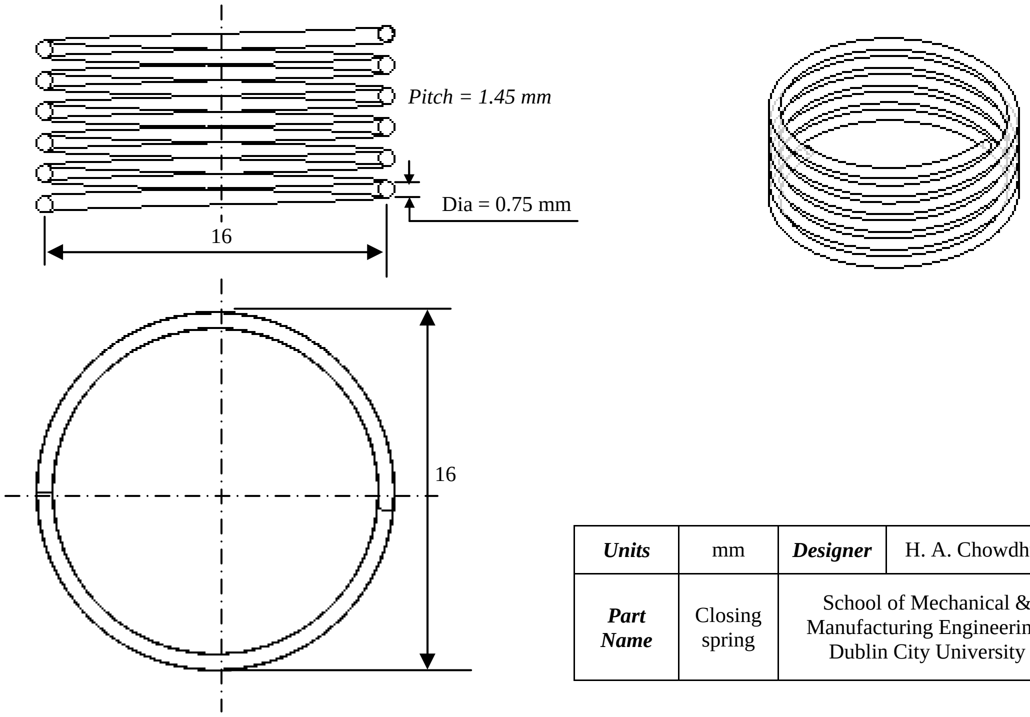

Units	mm	***Designer***	H. A. Chowdhury
Part Name	Closing spring	School of Mechanical & Manufacturing Engineering, Dublin City University	

Figure B4: Closing spring.

APPENDIX C

FEMM MAGNETOSTATIC SIMULATION RESULTS

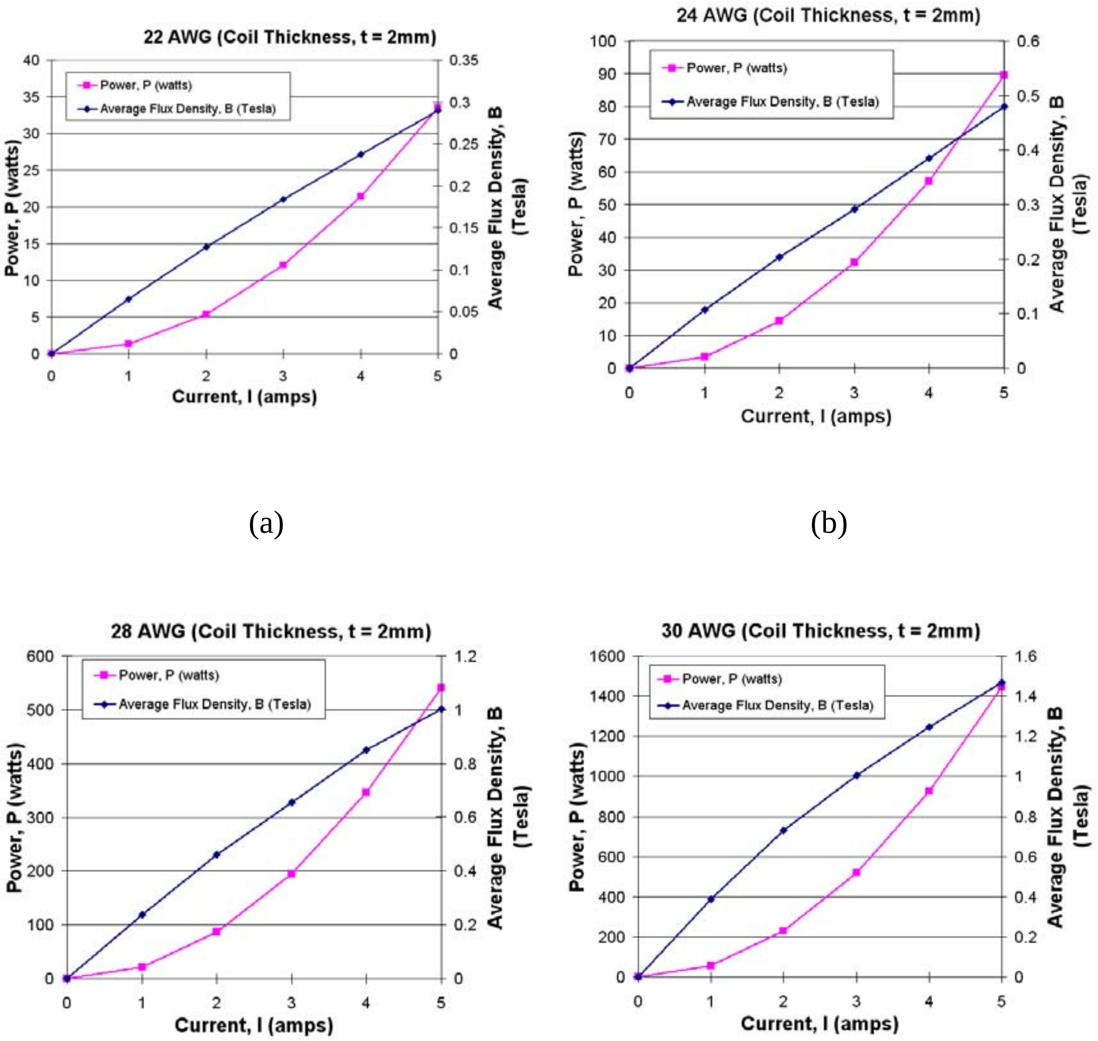

(a) (b)

(c) (d)

Figure C1: Variation of power and average flux density with current at coil thickness, t = 2 mm for; (a) 22 AWG, (b) 24 AWG, (c) 28 AWG and (d) 30 AWG.

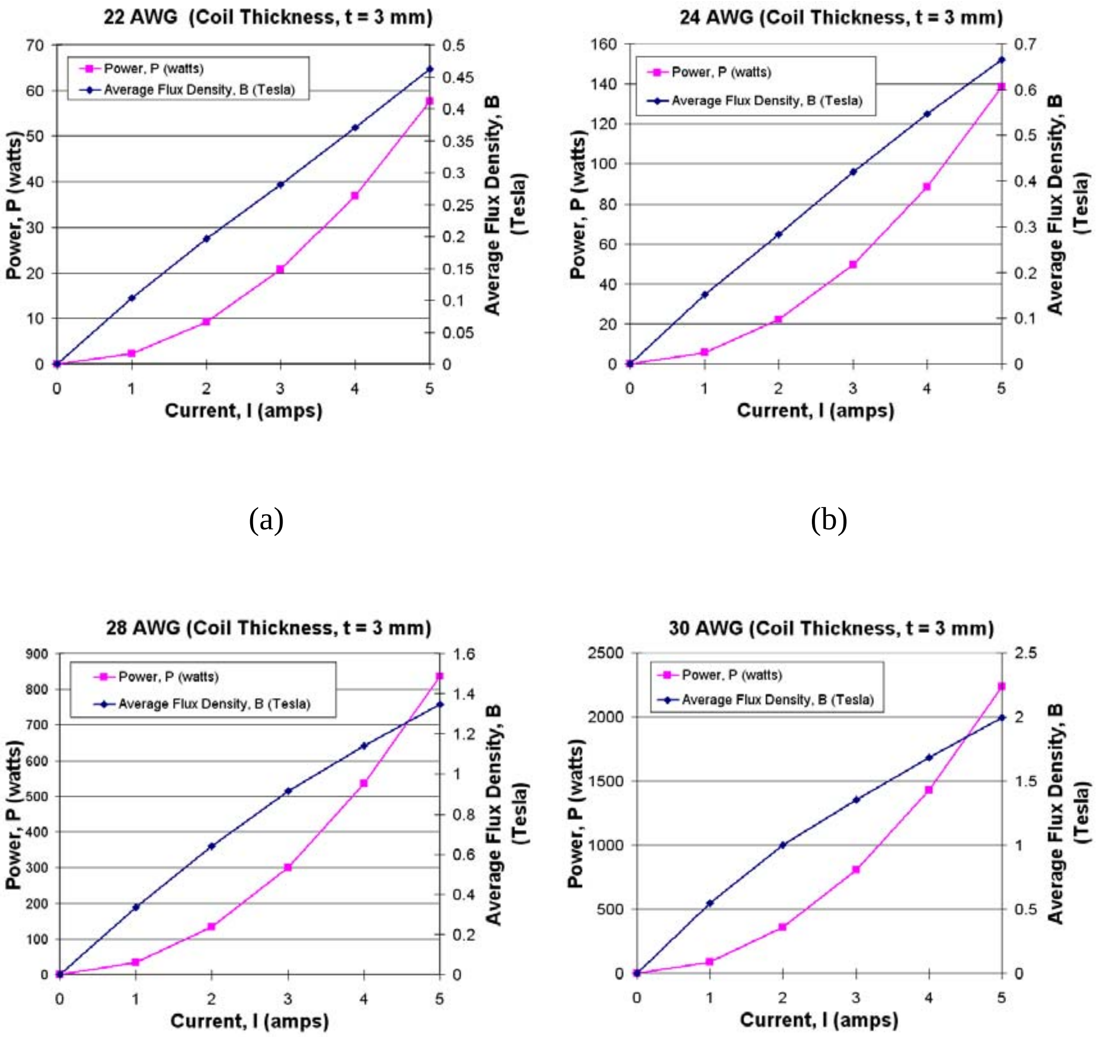

(a) (b)

(c) (d)

Figure C2: Variation of power and average flux density with current at coil thickness, t = 3 mm for; (a) 22 AWG, (b) 24 AWG, (c) 28 AWG and (d) 30 AWG.

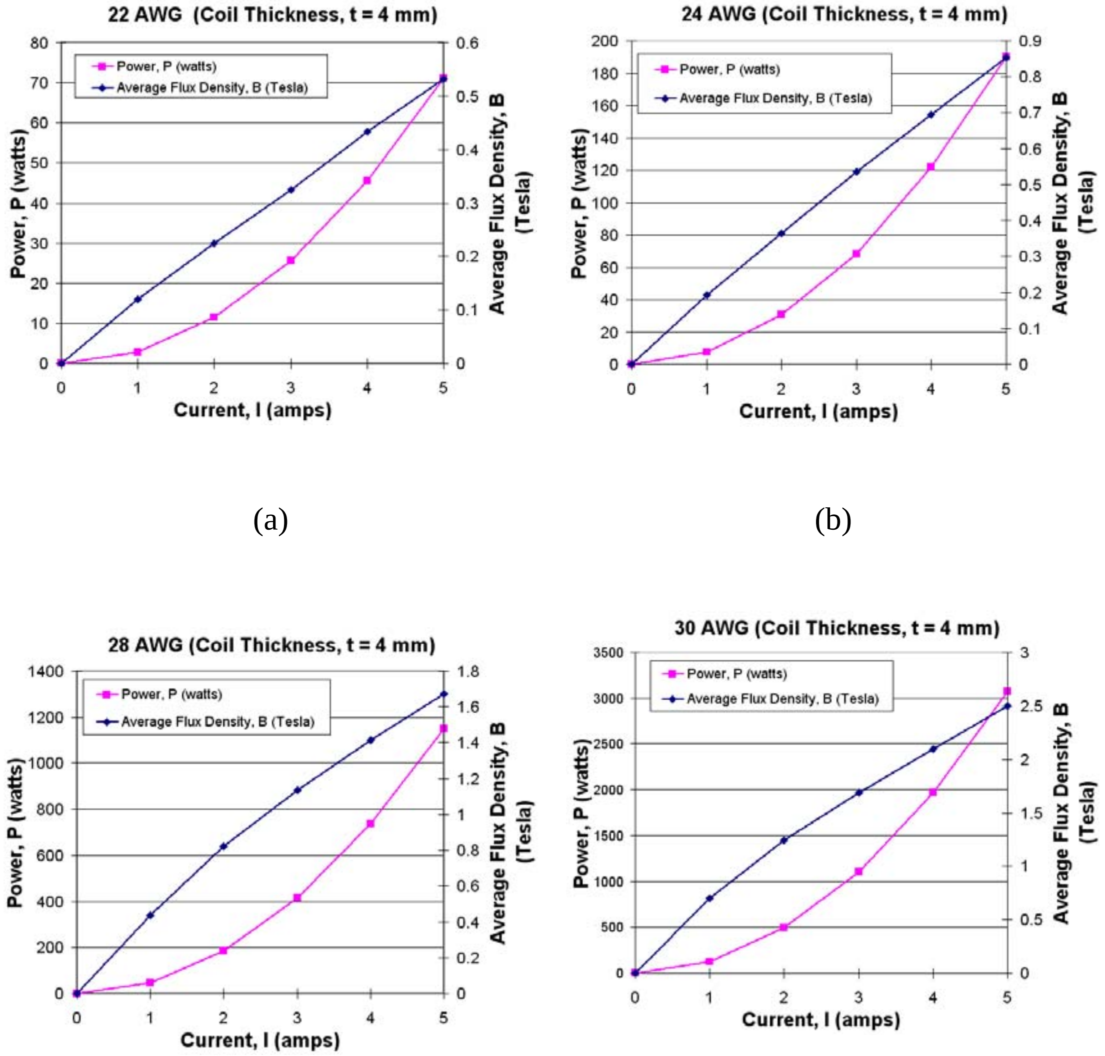

(a) (b)

(c) (d)

Figure C3: Variation of power and average flux density with current at coil thickness, t = 4 mm for; (a) 22 AWG, (b) 24 AWG, (c) 28 AWG and (d) 30 AWG.

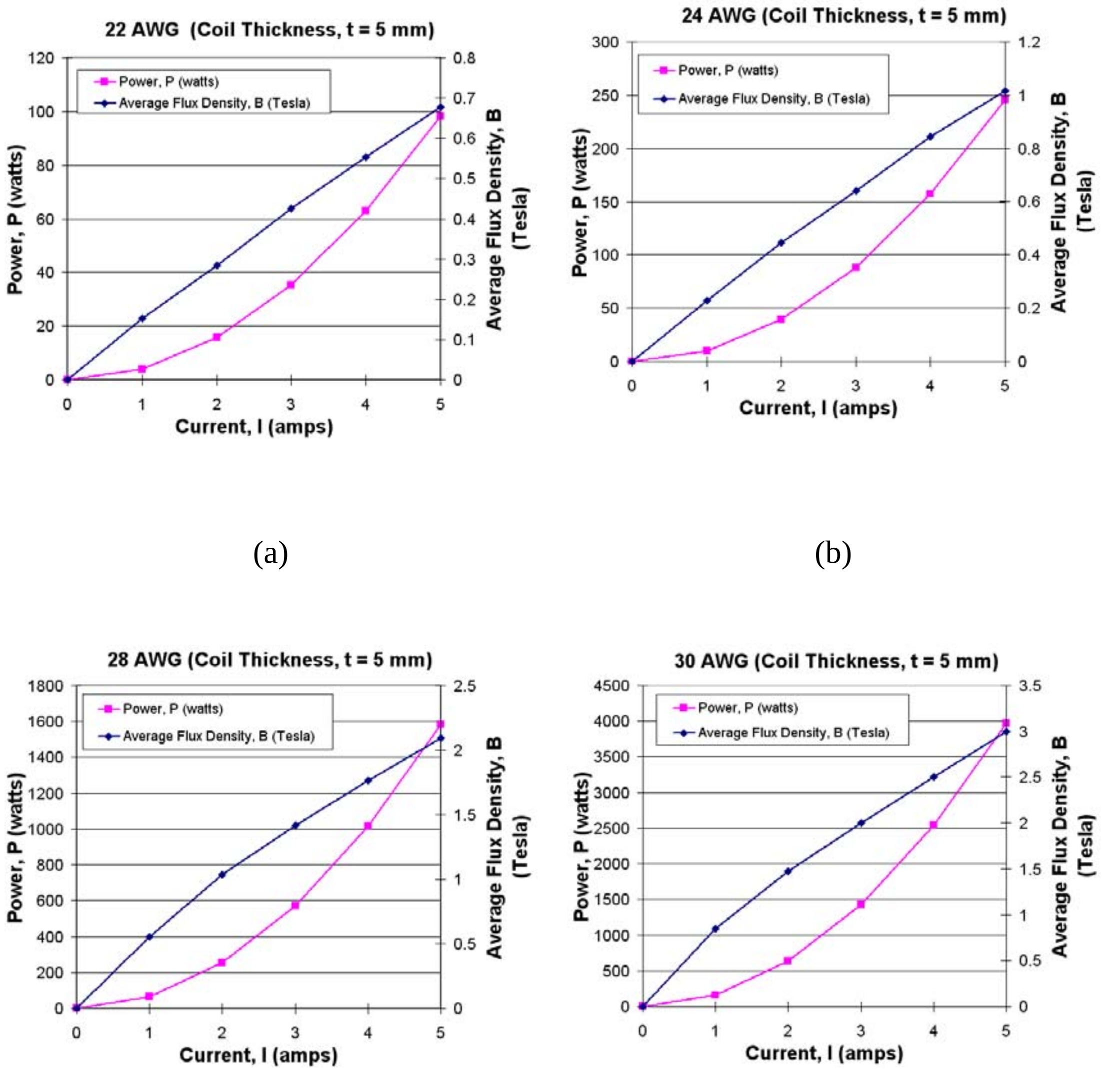

(a) (b)

(c) (d)

Figure C4: Variation of power and average flux density with current at coil thickness, t = 5 mm for; (a) 22 AWG, (b) 24 AWG, (c) 28 AWG and (d) 30 AWG.